(12)

ERL-0344-TR

AR-004-260

AD-A161 540

DEPARTMENT OF DEFENCE

DEFENCE SCIENCE AND TECHNOLOGY ORGANISATION

ELECTRONICS RESEARCH LABORATORY

DEFENCE RESEARCH CENTRE SALISBURY
SOUTH AUSTRALIA

TECHNICAL REPORT
ERL-0344-TR

THE RADAR CROSS SECTION OF PERFECTLY-CONDUCTING RECTANGULAR FLAT PLATES AND RECTANGULAR CYLINDERS – A COMPARISON OF PHYSICAL OPTICS, GTD AND UTD SOLUTIONS

W.C. ANDERSON

DTIC
ELECTE
NOV 26 1985
S D
D

DTIC FILE COPY

THE UNITED STATES NATIONAL TECHNICAL INFORMATION SERVICE IS AUTHORISED TO REPRODUCE AND SELL THIS REPORT

Approved for Public Release

COPY No. 14

© Commonwealth of Australia
AUGUST 1985

11 21 - 85 029

UNCLASSIFIED

AR-004-260

DEPARTMENT OF DEFENCE

DEFENCE SCIENCE AND TECHNOLOGY ORGANISATION

ELECTRONICS RESEARCH LABORATORY

TECHNICAL REPORT

ERL-0344-TR

THE RADAR CROSS SECTION OF PERFECTLY-CONDUCTING RECTANGULAR FLAT PLATES AND RECTANGULAR CYLINDERS - A COMPARISON OF PHYSICAL OPTICS, GTD AND UTD SOLUTIONS

W.C. Anderson

SUMMARY

The method of Physical Optics, the Geometrical Theory of Diffraction and the Uniform Geometrical Theory of Diffraction are applied here to electromagnetic scattering from flat plates and rectangular cylinders. The results are compared with experimental measurements to establish the domains of validity of the theoretical techniques.

Accesion For	
NTIS CRA&I	☑
DTIC TAB	☐
Unannounced	☐
Justification	
By	
Distribution /	
Availability Codes	
Dist	Avail and / or Special
A-1	

POSTAL ADDRESS: Director, Electronics Research Laboratory, Box 2151, GPO, Adelaide, South Australia, 5001.

QUALITY INSPECTED 3

UNCLASSIFIED

TABLE OF CONTENTS

	Page No.
1. INTRODUCTION	1
2. SCATTERING ANALYSIS USING PHYSICAL OPTICS	1
2.1 The method of physical optics	1
2.2 Backscattering from a rectangular flat plate	2
2.3 Backscattering from a rectangular cylinder	3
3. SCATTERING ANALYSIS USING THE GEOMETRICAL THEORY OF DIFFRACTION	4
3.1 The geometrical theory of diffraction	4
3.2 Backscattering from a rectangular flat plate	4
3.2.1 Vertical polarisation	5
3.2.2 Horizontal polarisation	10
3.3 Backscattering from a rectangular cylinder	12
3.3.1 Vertical polarisation	13
3.3.2 Horizontal polarisation	14
4. SCATTERING ANALYSIS USING THE KOUYOUMJIAN-PATHAK UNIFORM GEOMETRICAL THEORY OF DIFFRACTION	18
4.1 The uniform geometrical theory of diffraction	18
4.2 Backscattering from a rectangular flat plate	20
4.2.1 Vertical polarisation	20
4.2.2 Horizontal polarisation	20
4.3 Backscattering from a rectangular cylinder	23
4.3.1 Vertical polarisation	23
4.3.2 Horizontal polarisation	24
5. EXPERIMENTAL MEASUREMENTS	25
5.1 The anechoic chamber	25
5.2 Flat plate experiments	26
5.3 Rectangular cylinder measurements	26
5.4 Asymmetry of anechoic chamber measurements	27
6. RESULTS	28
6.1 Flat plate	28
6.1.1 Vertical polarisation	28
6.1.2 Horizontal polarisation	28

6.2 Rectangular cylinder 29

6.2.1 Vertical polarisation 29
6.2.2 Horizontal polarisation 30

6.3 Comparison with Moment Method solution 32

6.4 Deficiencies of the theories 33

6.4.1 Physical Optics 33
6.4.2 Geometrical theory of diffraction and uniform geometrical theory of diffraction 33

7. CONCLUSIONS 35

8. ACKNOWLEDGEMENT 35

REFERENCES 36

LIST OF TABLES

1. EXPRESSIONS FOR INCIDENT FIELD, DIFFRACTING ANGLE AND DISTANCE TO THE FAR-FIELD POINT FOR DIFFRACTING POINTS A', B' AND C' 13

2. DIMENSIONS OF FLAT PLATES IN TERMS OF WAVELENGTH 26

3. DIMENSIONS OF RECTANGULAR CYLINDER IN TERMS OF WAVELENGTH 27

LIST OF FIGURES

1. Flat plate

2. Rectangular cylinder

3. Top view of flat plate in azimuthal plane

4. Case (a) Multiple diffraction processes

5. Case (b) Multiple diffraction processes

6. Top view of rectangular cylinder in azimuthal plane

7. Self-consistent representation of surface waves on the rectangular cylinder

8. Self-consistent representation of surface waves on the strip

9. RCS for flat plate at 4 GHz (vertical polarisation)

10. RCS for flat plate at 6 GHz (vertical polarisation)

11. RCS for flat plate at 8 GHz (vertical polarisation)

12. RCS for flat plate at 10 GHz (vertical polarisation)

13. RCS for flat plate at 12 GHz (vertical polarisation)

14. RCS for flat plate at 4 GHz (horizontal polarisation)

15. RCS for flat plate at 6 GHz (horizontal polarisation)

16. RCS for flat plate at 8 GHz (horizontal polarisation)

17. RCS for flat plate at 10 GHz (horizontal polarisation)

18. RCS for flat plate at 12 GHz (horizontal polarisation)

19. RCS for 10 cm cylinder at 4 GHz (vertical polarisation)

20. RCS for 30 cm cylinder at 4 GHz (vertical polarisation)

21. RCS for 50 cm cylinder at 4 GHz (vertical polarisation)

22. RCS for 10 cm cylinder at 6 GHz (vertical polarisation)

23. RCS for 30 cm cylinder at 6 GHz (vertical polarisation)

24. RCS for 50 cm cylinder at 6 GHz (vertical polarisation)

25. RCS for 10 cm cylinder at 8 GHz (vertical polarisation)

26. RCS for 30 cm cylinder at 8 GHz (vertical polarisation)

27. RCS for 50 cm cylinder at 8 GHz (vertical polarisation)

28. RCS for 10 cm cylinder at 10 GHz (vertical polarisation)

29. RCS for 30 cm cylinder at 10 GHz (vertical polarisation)

30. RCS for 50 cm cylinder at 10 GHz (vertical polarisation)

31. RCS for 10 cm cylinder at 12 GHz (vertical polarisation)

32. RCS for 30 cm cylinder at 12 GHz (vertical polarisation)

33. RCS for 50 cm cylinder at 12 GHz (vertical polarisation)

34. RCS for 10 cm cylinder at 4 GHz (horizontal polarisation)

35. RCS for 30 cm cylinder at 4 GHz (horizontal polarisation)

36. RCS for 50 cm cylinder at 4 GHz (horizontal polarisation)

37. RCS for 10 cm cylinder at 6 GHz (horizontal polarisation)

38. RCS for 30 cm cylinder at 6 GHz (horizontal polarisation)

39. RCS for 50 cm cylinder at 6 GHz (horizontal polarisation)

40. RCS for 10 cm cylinder at 8 GHz (horizontal polarisation)

41. RCS for 30 cm cylinder at 8 GHz (horizontal polarisation)

42. RCS for 50 cm cylinder at 8 GHz (horizontal polarisation)

43. RCS for 10 cm cylinder at 10 GHz (horizontal polarisation)

44. RCS for 30 cm cylinder at 10 GHz (horizontal polarisation)

45. RCS for 50 cm cylinder at 10 GHz (horizontal polarisation)

46. RCS for 10 cm cylinder at 12 GHz (horizontal polarisation)

47. RCS for 30 cm cylinder at 12 GHz (horizontal polarisation)

48. RCS for 50 cm cylinder at 12 GHz (horizontal polarisation)

49. Comparison of UTD, PO and MM solutions for the flat plate at 4 GHz (vertical polarisation)

50. Comparison of UTD, PO and MM solutions for the flat plate at 4 GHz (horizontal polarisation)

51. Comparison of UTD, PO and MM solutions for the flat plate at 2 GHz (vertical polarisation)

52. Comparison of UTD, PO and MM solutions for the flat plate at 2 GHz (horizontal polarisation)

1. INTRODUCTION

The radar scattering properties of rectangular flat plates and rectangular cylinders are of concern for a number of reasons of which the following are perhaps the most important:

(i) Some targets of interest can be approximated by one of these shapes, in which case the results apply directly,

(ii) Many targets can be approximated by a composition of these primitive shapes; calculation of the radar scattering properties of complex targets may then reduce to an iterative procedure employing the scattering properties of the primitives,

(iii) Since these shapes are easily fabricated, they are convenient for anechoic chamber experiments; such measurements may be used to validate theoretical predictions or to assist in calibrating the anechoic chamber itself.

In this report, the radar cross sections of flat plates and rectangular cylinders are calculated using Physical Optics, the Geometrical Theory of Diffraction and the Uniform Geometrical Theory of Diffraction. The theoretical predictions are then compared with experimental measurements obtained in the ERL anechoic chamber.

In the present context the primary motivation was one of establishing the domains of validity of three important theoretical techniques for calculating radar cross sections: physical optics, the geometrical theory of diffraction and the uniform geometrical theory of diffraction. This objective is part of a broader investigation which aims at deriving guidelines for employing the various techniques available to the electromagnetics researcher. At present it appears to be the case that some methods yield sensible results over a wider range of situations than might be expected. In other circumstances the opposite holds. It is difficult to predict this behaviour from the isolated theory; one must apply the techniques to real problems and confirm their validity by comparison with experiment.

Obviously even this methodology has its limitations but there is no clear alternative if one wishes to be able to select and apply theoretical methods with confidence that the results will be meaningful.

The remainder of this paper is organised as follows. First the method of physical optics (PO) is described and applied in turn to the flat plate and the rectangular cylinder. Next the geometrical theory of diffraction (GTD) and the uniform geometrical theory of diffraction (UTD) are applied to the same targets. A brief description of the experimental measurements carried out in the anechoic chamber is then given, followed by a discussion of the comparisons between theories and experiment. Some limited comparisons with solutions obtained using the method of moments are included.

Finally, some conclusions are drawn regarding the domains of validity of the theoretical techniques.

2. SCATTERING ANALYSIS USING PHYSICAL OPTICS

2.1 The method of physical optics

Physical optics determines the field scattered from a scatterer by assuming that the field on the surface of the scatterer is the geometric optics surface field. At each point on the geometrically illuminated side of the body, the induced surface current is the same as that on an infinite

tangent plane at the point, whereas over the shadowed body, the surface field is zero. For a perfectly conducting body, the surface current distribution on the scatterer is then

$$\underset{\sim}{J}_{po} = \begin{cases} 2\hat{n} \times \underset{\sim}{H}^{i} & \text{in the illuminated region, } S_i \\ 0 & \text{in the shadowed region} \end{cases} \tag{1}$$

where $\hat{n}$ is a unit vector normal drawn outwards from the body and $\underset{\sim}{H}^{i}$ is the incident magnetic field. This is only valid for wavelengths very much smaller than the dimensions of the object. When this surface current is substituted into the magnetic field integral equation, the physical optics approximation for the scattered magnetic field $\underset{\sim}{H}^{s}$ is obtained, that is,

$$\underset{\sim}{H}^{s} = \frac{1}{4\pi}\int_{S_i} 2(\hat{n} \times \underset{\sim}{H}^{i}) \times \nabla\left(\frac{e^{-ikR}}{R}\right) dS_i \tag{2}$$

where $k = \frac{2\pi}{\lambda}$, R is the distance between the field point and the integration point on the scatterer and $\int_{S_i}$ denotes the integral over the illuminated surface S_i of the body. The time factor $e^{i\omega t}$ is assumed and suppressed.

When the field point is a large distance from the body, the scattered magnetic field simplifies to

$$\underset{\sim}{H}^{s} = \frac{ik}{4\pi}\frac{e^{-ikr}}{r}\int_{S_i} 2(\hat{n} \times \underset{\sim}{H}^{i}) \times \hat{r}\, e^{ik\hat{r}.\underset{\sim}{r}'}\, dS_i \tag{3}$$

where $\hat{r}$ is the unit vector from the origin to the field point, r is the distance from the origin to the field point and $\underset{\sim}{r}'$ is the radius vector from the origin to the integration point. For backscattering $\hat{r} = -\hat{k}$ ($\hat{k}$ being the unit wave vector), so the backscattered magnetic field, valid in the far field limit, is

$$\underset{\sim}{H}^{s} = \frac{ik}{4\pi}\frac{e^{-ikr}}{r}\int_{S_i} 2(\hat{n} \times \underset{\sim}{H}^{i}) \times (-\hat{k})\, e^{-ik\hat{k}.\underset{\sim}{r}'}\, dS_i \tag{4}$$

Useful accounts of the application of physical optics to radar scattering can be found in references 1 and 2.

2.2 Backscattering from a rectangular flat plate

A rectangular flat plate of sides 2a and 2b lies in the y-z plane as shown in figure 1.

A plane wave is incident on the plate in the azimuthal plane making an angle ϕ with the x-axis. Thus $\hat{k} = -\cos\phi\hat{i}_x - \sin\phi\hat{i}_y$. Let the incident magnetic field be $\underset{\sim}{H}^i = \hat{\ell}H_o e^{-ik\hat{k}.\underset{\sim}{r}'}$. If the incident wave is a horizontally polarised wave, $\hat{\ell} = \hat{i}_z$, $\hat{n} = \hat{i}_x$, $\underset{\sim}{r}' = y\hat{i}_y + z\hat{i}_z$ so that the backscattered field is

$$\underset{\sim}{H}^s = \hat{i}_z \frac{ik}{4\pi} \frac{e^{-ikr}}{r} 2H_o \cos\phi \int_{S_i} e^{2iksin\phi y} dS_i$$

$$= \hat{i}_z \frac{ik}{4\pi} \frac{e^{-ikr}}{r} 2H_o \, 4ab \cos\phi \frac{\sin(2kasin\phi)}{2kasin\phi} \tag{5}$$

Hence the monostatic radar cross section of the flat plate is

$$\sigma_{po} = \lim_{r\to\infty} 4\pi r^2 \left|\frac{\underset{\sim}{H}^s}{\underset{\sim}{H}^i}\right|^2$$

$$= \frac{64\pi}{\lambda^2} a^2b^2 \cos^2\phi \left[\frac{\sin(2kasin\phi)}{2kasin\phi}\right]^2 \tag{6}$$

If the incident wave is a vertically polarised wave, $\hat{\ell} = \sin\phi\hat{i}_x - \cos\phi\hat{i}_y$ and the backscattered field is determined by equation (4) to be

$$\underset{\sim}{H}^s = (\sin\phi \cos\phi\hat{i}_x - \cos^2\phi\hat{i}_y) \frac{ik}{4\pi} \frac{e^{-ikr}}{r} 2H_o \, 4ab \frac{\sin(2kasin\phi)}{2kasin\phi} \tag{7}$$

yielding a monostatic radar cross section equal to that given by equation (6) for horizontal polarisation. Although the physical optics radar cross section is polarisation independent in this case, this is not necessarily true of composite targets where multiple reflections can occur; this has been strikingly demonstrated in an analysis of the orthogonal trihedral corner reflector(ref.3).

2.3 Backscattering from a rectangular cylinder

A cylinder of height 2b has a rectangular cross section of sides 2a, 2c. The axis of the cylinder lies along the z-axis as shown in figure 2.

A plane wave is incident on the cylinder in the azimuthal plane making an angle of ϕ with the x-axis so $\hat{k} = -\cos\phi\hat{i}_x - \sin\phi\hat{i}_y$. Let the incident magnetic field be $\underset{\sim}{H}^i = \hat{\ell}H_o e^{-ik\hat{k}.\underset{\sim}{r}'}$. If the incident wave is horizontally polarised, $\hat{\ell} = \hat{i}_z$ and the scattered field is given by

$$\underline{H}^s = \hat{i}_z \frac{ik}{4\pi} \frac{e^{-ikr}}{r} 2H_o \, 4b \left[a \cos\phi \, e^{2ikc\cos\phi} \frac{\sin(2ka\sin\phi)}{2ka\sin\phi} + c \sin\phi \, e^{2ika\sin\phi} \frac{\sin(2kc\cos\phi)}{2kc\cos\phi} \right] \tag{8}$$

The monostatic radar cross section is then

$$\sigma_{po} = \frac{64\pi b^2}{\lambda^2} \left| a \cos\phi \, e^{2ikc\cos\phi} \frac{\sin(2ka\sin\phi)}{2ka\sin\phi} + c \sin\phi \, e^{2ika\sin\phi} \frac{\sin(2kc\cos\phi)}{2kc\cos\phi} \right|^2 \tag{9}$$

This expression is also valid for a vertically polarised incident wave as well.

3. SCATTERING ANALYSIS USING KELLER'S GEOMETRICAL THEORY OF DIFFRACTION

3.1 The geometrical theory of diffraction

In geometrical optics only incident, reflected and refracted rays are described. Keller's geometrical theory of diffraction is an extension of geometrical optics in which diffracted rays are introduced by a generalisation of Fermat's principle. Diffracted rays are produced when incident rays hit edges, corners or vertices of scattering surfaces, or when incident rays impinge tangentially on smoothly curved boundaries. Diffracted rays can penetrate into the shadow regions and account for the fields there. The initial value of the field on a diffracted ray is obtained by multiplying the field on the incident ray at the point of diffraction by an appropriate diffraction coefficient. Diffraction is treated as a local phenomenon determined entirely by the local properties of the field, the media and the boundary in the immediate neighbourhood of the point of diffraction. Thus the diffraction coefficient is determined from the solution of the simplest boundary value problems having these local properties; these problems are called canonical problems. Away from the diffracting surfaces, the diffracted rays behave just like the ordinary rays of geometrical optics. As before, a time factor $e^{i\omega t}$ is assumed and is suppressed throughout the work.

3.2 Backscattering from a rectangular flat plate

A rectangular flat plate of sides 2a, 2b becomes an infinite strip of width 2a when $b \to \infty$. Ross(ref.4) has shown that the results for an infinite strip can be adapted to that for the rectangular flat plate. A plane wave is incident on the flat plate in the azimuthal plane making an angle of ϕ with the x-axis as shown in figures 1 and 3. It can be seen that, if corner diffraction is neglected, only edge diffracted fields from edges AD and BC will contribute to the backscattered field for angles of incidence $\phi \neq 0$ as for the infinite strip.

The backscattered far field is derived for an infinite strip and the radar cross section per unit length, σ(length), is then calculated. The area backscatter radar cross section, σ(area), for the rectangular plate is obtained using the formula which relates area and length cross sections(ref.5)

$$\sigma(\text{area}) = \frac{8b^2}{\lambda}\,\sigma(\text{length}) \tag{10}$$

Both vertical and horizontal polarisations are considered here.

3.2.1 Vertical polarisation

Following James(ref.6), the diffracted field for normal incidence of a plane wave on a straight edge of a half-plane is

$$E_v(s^d) = D^e E_v^i(P_o)\,(s^d)^{-\frac{1}{2}}\,e^{-iks^d} \tag{11}$$

where D^e is the half-plane diffraction coefficient for vertical polarisation, $E_v^i(P_o)$ is the incident field at the point of diffraction P_o and s^d is the distance of the field point from the diffraction point. The diffracted field E_v and incident field E_v^i have only z-components. These diffracted rays lie in a plane perpendicular to the edge. When a diffracted ray hits another edge it can again produce diffracted rays and so on. Thus one has not only singly diffracted rays from the two parallel edges contributing to the backscattered field but also doubly, triply and other higher order multiply diffracted rays contributing as well. The diffracted far field is given by equation (11) with

$$D^e(\phi_p,\phi_o) = -\frac{1}{\sqrt{8i\pi k}}\left[\sec\tfrac{1}{2}(\phi_p - \phi_o) - \sec\tfrac{1}{2}(\phi_p + \phi_o)\right] \tag{12}$$

where ϕ_o is the incident angle measured from the half plane faces and ϕ_p is the angle of the diffracted ray measured from the same half-plane face at the point of diffraction. The singly diffracted ray from diffraction point A' is given by equations (11) and (12) with $s^d = \rho + a\sin\phi$ where ρ is the distance between O, the coordinate origin, on the plate and the field point and $\rho \gg a\sin\phi$. Referring the phase of the incident field to O, the incident wave at A' is $E_v^i(A') = E_o\,e^{-ika\sin\phi}$. The singly diffracted field scattered back towards the source is thus

$$E_v^{A'} \sim -\left[\sec\tfrac{1}{2}(\phi_{A'} - \phi_o) - \sec\tfrac{1}{2}(\phi_{A'} + \phi_o)\right] E_o\,e^{-2ika\sin\phi}\,\frac{e^{-ik\rho}}{\sqrt{8i\pi k\rho}} \tag{13}$$

Figure 3 shows $\phi_{A'} = \phi_o = \frac{\pi}{2} - \phi$, so

$$E_v^{A'} \sim -\left(1 - \frac{1}{\sin\phi}\right) E_o\,e^{-2ika\sin\phi}\,\frac{e^{-ik\rho}}{\sqrt{8i\pi k\rho}} \tag{14}$$

The singly diffracted ray from B' is given by equations (11) and (12) with $s^d = \rho - a\sin\phi$, $E_v^i(B') = E_o\,e^{ika\sin\phi}$, $\phi_{A'} = \phi_o = \frac{\pi}{2} + \phi$; thus

$$E_v^{B'} \sim -\left(1 + \frac{1}{\sin\phi}\right) E_o\, e^{2ika\sin\phi} \frac{e^{-ik\rho}}{\sqrt{i\pi k\rho}} \tag{15}$$

The total singly diffracted field from A' and B' backscattered towards the source is

$$E_v^s \sim -2\left[\cos(2ka\sin\phi) + 2ika\,\frac{\sin(2ka\sin\phi)}{2ka\sin\phi}\right] E_o \frac{e^{-ik\rho}}{\sqrt{8i\pi k\rho}} \tag{16}$$

The singly diffracted ray from A' in the direction of $\phi_{A'} = 0, 2\pi$ hits B' when $s^d = 2a$ on the front and rear of the strip respectively; equations (11) and (12) constrain this field to be zero. In order to calculate the doubly diffracted rays from B', a higher order edge diffraction term has to be considered - this is called the slope diffraction term where the diffracted field is not proportional to the incident field but to the normal derivative of the incident field at the point of diffraction. This is given by James(ref.6) to be

$$E_v \sim \frac{1}{2ik}\frac{1}{\sqrt{8i\pi k}}\Big[\sin\tfrac{1}{2}(\phi_p - \phi_o)\sec^2\tfrac{1}{2}(\phi_p - \phi_o)$$

$$+ \sin\tfrac{1}{2}(\phi_p + \phi_o)\sec^2\tfrac{1}{2}(\phi_p + \phi_o)\Big]\frac{\partial E_v^i}{\partial n}(s^d)^{-\frac{1}{2}}\, e^{-iks^d} \tag{17}$$

for a vertically polarised incident wave at normal incidence on the edge of a half-plane. In calculating the multiply diffracted fields, the factor $\frac{1}{2}$ for grazing incidence(ref.6) is dropped. This is equivalent to adding the backscattered field resulting from the diffraction of the surface wave on the front of the strip to the backscattered field resulting from diffraction of the surface wave on the rear of the strip, both front and rear waves contributing equally. Thus the doubly diffracted field from B' in the backscatter direction is given by equation (17) with the normal derivative of the incident field

$$\frac{\partial E_v^i}{\partial n} \sim \frac{\sqrt{2}}{2a} E_o\, e^{-ika\sin\phi} \frac{e^{-ik2a}}{\sqrt{8i\pi k2a}} \frac{\sqrt{1 - \sin\phi}}{1 + \sin\phi} \tag{18}$$

and

$$\phi_{B'} = \frac{\pi}{2} + \phi,\ \phi_o = 0,\ s^d = \rho - a\sin\phi$$

whence

$$E_v^{B'} \sim \frac{E_o}{ika}\frac{e^{-ik2a}}{\sqrt{8i\pi k2a}}\frac{e^{-ik\rho}}{\sqrt{8i\pi k\rho}}\frac{1}{\cos\phi} \tag{19}$$

Similarly the doubly diffracted field from A' is given by equation (17) with the normal derivative of the incident field

$$\frac{\partial E_v^i}{\partial n} \sim \frac{\sqrt{2}}{2a} E_o \, e^{ika\sin\phi} \frac{e^{-ik2a}}{\sqrt{8i\pi k2a}} \frac{\sqrt{1+\sin\phi}}{1-\sin\phi} , \tag{20}$$

$\phi_{A'} = \frac{\pi}{2} - \phi$, $\phi_o = 0$, $s^d = \rho + a\sin\phi$ whence

$$E_v^{A'} \sim \frac{E_o}{ika} \frac{e^{-ik2a}}{\sqrt{8i\pi k2a}} \frac{e^{-ik\rho}}{\sqrt{8i\pi k\rho}} \frac{1}{\cos\phi} \tag{21}$$

Thus the total doubly diffracted field in the backscattered direction is

$$E_v^d \sim \frac{2E_o}{ika} \frac{e^{-ik2a}}{\sqrt{8i\pi k2a}} \frac{e^{-ik\rho}}{\sqrt{8i\pi k\rho}} \frac{1}{\cos\phi} \tag{22}$$

To calculate the triply diffracted fields from A' and B', equation (17) has to be used as the doubly diffracted rays that hit A' and B' to produce triply diffracted fields are zero so that once again higher order diffraction terms have to be considered. The triply diffracted field from A' is given by equation (17) with the normal derivative of the incident field,

$$\frac{\partial E_v^i}{\partial n} \sim \frac{\sqrt{2}}{8ika^2} E_o \, e^{-ika\sin\phi} \left(\frac{e^{-ik2a}}{\sqrt{8i\pi k2a}}\right)^2 \frac{\sqrt{1-\sin\phi}}{1+\sin\phi} , \tag{23}$$

$\phi_{A'} = \frac{\pi}{2} - \phi$, $\phi_o = 0$, $s^d = \rho + a\sin\phi$ whence

$$E_v^{A'} \sim -\frac{E_o}{4a^2k^2} e^{-2ika\sin\phi} \left(\frac{e^{-ik2a}}{\sqrt{8i\pi k2a}}\right)^2 \frac{e^{-ik\rho}}{\sqrt{8i\pi k\rho}} \frac{(1-\sin\phi)}{(1+\sin\phi)^2} \tag{24}$$

Similarly, the triply diffracted field from B' is given by equation (17) with the normal derivative of the incident field,

$$\frac{\partial E_v^i}{\partial n} \sim \frac{\sqrt{2}}{8ika^2} E_o \, e^{ika\sin\phi} \left(\frac{e^{-ik2a}}{\sqrt{8i\pi k2a}}\right)^2 \frac{\sqrt{1+\sin\phi}}{1-\sin\phi} , \tag{25}$$

$\phi_{B'} = \frac{\pi}{2} + \phi$, $\phi_o = 0$, $s^d = \rho - a\sin\phi$ whence

$$E_v^{B'} \sim -\frac{E_o}{4a^2k^2} e^{2ika\sin\phi} \left(\frac{e^{-ik2a}}{\sqrt{8i\pi k2a}}\right)^2 \frac{e^{-ik\rho}}{\sqrt{8i\pi k\rho}} \frac{(1+\sin\phi)}{(1-\sin\phi)^2} \tag{26}$$

Thus the total diffracted field is

$$E_v^T \sim -\frac{E_o}{4a^2k^2}\left(\frac{e^{-ik2a}}{\sqrt{8i\pi k2a}}\right)^2 \frac{e^{-ik\rho}}{\sqrt{8i\pi k\rho}}\left[\frac{(1-\sin\phi)}{(1+\sin\phi)^2}\, e^{-2ika\sin\phi} + \frac{(1+\sin\phi)}{(1-\sin\phi)^2}\, e^{2ika\sin\phi}\right] \tag{27}$$

Higher order multiply diffracted fields can be obtained in a similar way by applying equation (17) repeatedly for the various incident fields on the edges and summing the results. It would be tedious indeed to have to evaluate each higher order field this way. It transpires, however, that the contribution from all the multiply diffracted fields can be accounted for in a very simple way if one observes that all multiply diffracted fields from doubly diffracted fields onwards can be divided into two general cases.

(a) The incident ray hits one edge and then undergoes 2, 4, 6, 8, ... diffractions before being backscattered from the other edge to the one it was incident on.

(b) The incident ray hits one edge and then undergoes 3, 5, 7, 9, ... diffractions before being backscattered from the same edge it was incident on.

These diffracting mechanisms are illustrated in figures 4 and 5. In summing the contributions from these multiply diffracted rays, it is seen that the doubly diffracted field given by equation (22) is a common multiple in case (a) so that the total field from the contributions is

$$E_v^{MI} \sim \frac{2E_o}{ika}\frac{e^{-ik2a}}{\sqrt{8i\pi k2a}}\frac{e^{-ik\rho}}{\sqrt{8i\pi k\rho}}\frac{1}{\cos\phi}(1 + x^2 + x^4 + \ldots\ldots) \tag{28}$$

where

$$x = \frac{1}{ik}\frac{1}{2a}\frac{\partial}{\partial\phi_p}\left\{\frac{1}{2\sqrt{8i\pi k}}\left[\sin\tfrac{1}{2}(\phi_p - \phi_o)\sec^2\tfrac{1}{2}(\phi_p - \phi_o) + \sin\tfrac{1}{2}(\phi_p + \phi_o)\sec^2\tfrac{1}{2}(\phi_p + \phi_o)\right]\right\}(s^d)^{-\frac{1}{2}}\, e^{-iks^d}$$

evaluated at $s^d = 2a$ and $\phi_p = \phi_o = 0$, that is,

$$x = \frac{1}{4ika}\frac{e^{-ik2a}}{\sqrt{8i\pi k2a}} \tag{29}$$

and

$$x^2 = -\frac{e^{-ik4a}}{256i\pi k^3a^3} \tag{30}$$

Thus the sum is the sum of an infinite geometric series and

$$E_v^{M1} \sim \frac{2E_o}{ika} \frac{e^{-ik2a}}{\sqrt{8i\pi k2a}} \frac{e^{-ik\rho}}{\sqrt{8i\pi k\rho}} \frac{1}{\cos\phi} \left(1 + \frac{e^{-ik4a}}{256i\pi k^3a^3}\right)^{-1} \tag{31}$$

The triply diffracted field given by equation (27) is a common multiple in case (b) so that the total field can be written as

$$E_v^{M2} \sim -\frac{E_o}{4a^2k^2} \left(\frac{e^{-ik2a}}{\sqrt{8i\pi k2a}}\right)^2 \frac{e^{-ik\rho}}{\sqrt{8i\pi k\rho}} \left[\frac{(1 - \sin\phi)}{(1 + \sin\phi)^2} e^{-2ikasin\phi} + \frac{(1 + \sin\phi)}{(1 - \sin\phi)^2} e^{2ikasin\phi}\right] (1 + x^2 + x^4 + \ldots.) \tag{32}$$

where x^2 is as given by equation (30).

Thus

$$E_v^{M2} \sim -\frac{E_o}{4a^2k^2} \left(\frac{e^{-ik2a}}{\sqrt{8i\pi k2a}}\right)^2 \frac{e^{-ik\rho}}{\sqrt{8i\pi k\rho}} \left[\frac{(1 - \sin\phi)}{(1 + \sin\phi)^2} e^{-2ikasin\phi} + \frac{(1 + \sin\phi)}{(1 - \sin\phi)^2} e^{2ikasin\phi}\right] \left(1 + \frac{e^{-ik4a}}{256i\pi k^3a^3}\right)^{-1} \tag{33}$$

The total backscattered field for the plate is then

$$E_v^{tot} \sim -2E_o \frac{e^{-ik\rho}}{\sqrt{8i\pi k\rho}} K_1 \tag{34(a)}$$

where

$$K_1 = \cos(2kasin\phi) + 2ika \frac{\sin(2kasin\phi)}{2kasin\phi} - \left(1 + \frac{e^{-ik4a}}{256i\pi k^3a^3}\right)^{-1} \left\{\frac{e^{-ik2a}}{\sqrt{8i\pi k2a}} \frac{1}{ikacos\phi} - \frac{1}{8a^2k^2} \left(\frac{e^{-ik2a}}{\sqrt{8i\pi k2a}}\right)^2 \left[\frac{(1 - \sin\phi)}{(1 + \sin\phi)^2} e^{-2ikasin\phi} + \frac{(1 + \sin\phi)}{(1 - \sin\phi)^2} e^{2ikasin\phi}\right]\right\} \tag{34(b)}$$

The monostatic radar cross section per unit length for vertical polarisation is defined to be

$$\sigma_v(\text{length}) = \lim_{\rho\to\infty} 2\pi\rho \left|\frac{E_v^{tot}}{E_o}\right|^2 = \frac{|K_1|^2}{k} \tag{35}$$

and the area backscatter radar cross section of the rectangular plate is given by equation (10) to be

$$\sigma_v^{GTD} = \frac{4b^2}{\pi} |K_1|^2 \tag{36}$$

3.2.2 Horizontal polarisation

The diffracted field for normal incidence of a plane wave on a straight edge is

$$E_H(s^d) = D^m E_H^i(P_o)(s^d)^{-\frac{1}{2}} e^{-iks^d} \tag{37}$$

where D^m is the half-plane diffraction coefficient for horizontal polarisation, $E_H^i(P_o)$ is the incident field at the point of diffraction and s^d is the distance between the diffraction point and the field point.

$$D^m(\phi_p,\phi_o) = -\frac{1}{\sqrt{8i\pi k}} [\sec \tfrac{1}{2}(\phi_p - \phi_o) + \sec \tfrac{1}{2}(\phi_p + \phi_o)] \tag{38}$$

Singly diffracted rays from A' and B' are calculated in the same way as for vertical polarisation and the total singly diffracted field is

$$E_H^s \sim -2\left[\cos(2ka\sin\phi) - 2ika \frac{\sin(2ka\sin\phi)}{2ka\sin\phi}\right] E_o \frac{e^{-ik\rho}}{\sqrt{8i\pi k\rho}} \tag{39}$$

The singly diffracted field from B' in the direction $\phi_{B'} = 0$ hits A' when $s^d = 2a$. Thus the incident field at A' that gives rise to doubly diffracted field from A' is

$$E_H^i \sim -2\sqrt{2}\, E_o\, e^{ika\sin\phi} \frac{e^{-ik2a}}{\sqrt{8i\pi k2a}} \frac{1}{\sqrt{1-\sin\phi}} \tag{40}$$

The doubly diffracted field from A' is given by equations (37), (38) and (40) to be

$$E_H^{A'} \sim 8\, E_o \frac{e^{-ik2a}}{\sqrt{8i\pi k2a}} \frac{e^{-ik\rho}}{\sqrt{8i\pi k\rho}} \frac{1}{\cos\phi} \tag{41}$$

Again, the grazing incidence factor $\frac{1}{2}$ is dropped in the derivation for multiply diffracted fields to allow for the rear surface wave contributions.

Similarly the doubly diffracted field from B' can be found to be

$$E_H^{B'} \sim 8\, E_o \frac{e^{-ik2a}}{\sqrt{8i\pi k2a}} \frac{e^{-ik\rho}}{\sqrt{8i\pi k\rho}} \frac{1}{\cos\phi} \tag{42}$$

Accordingly, the total doubly diffracted field is

$$E_H^{d} \sim 16\, E_o \frac{e^{-ik2a}}{\sqrt{8i\pi k2a}} \frac{e^{-ik\rho}}{\sqrt{8i\pi k\rho}} \frac{1}{\cos\phi} \tag{43}$$

Using equations (37) and (38) again with the appropriate incident field, the triply diffracted field is found to be

$$E_H^{T} \sim -16\, E_o \left(\frac{e^{-ik2a}}{\sqrt{8i\pi k2a}}\right)^2 \frac{e^{-ik\rho}}{\sqrt{8i\pi k\rho}} \left[\frac{e^{2ika\sin\phi}}{1-\sin\phi} + \frac{e^{-2ika\sin\phi}}{1+\sin\phi}\right] \tag{44}$$

All multiply diffracted fields can be accounted for in the same simple way as for vertical polarisation (figures 4 and 5). The backscattered field for doubly, triply and all other higher order diffraction is given by

$$E_H^{M} \sim \left\{16\, E_o \frac{e^{-ik2a}}{\sqrt{8i\pi k2a}} \frac{e^{-ik\rho}}{\sqrt{8i\pi k\rho}} \frac{1}{\cos\phi} - 16\, E_o \left(\frac{e^{-ik2a}}{\sqrt{8i\pi k2a}}\right)^2 \frac{e^{-ik\rho}}{\sqrt{8i\pi k\rho}} \cdot \right.$$

$$\left. \left[\frac{e^{2ika\sin\phi}}{1-\sin\phi} + \frac{e^{-2ika\sin\phi}}{1+\sin\phi}\right]\right\}(1 + x^2 + x^4 + \ldots) \tag{45}$$

where

$$x = -\frac{1}{\sqrt{8i\pi k}} \left[\sec \tfrac{1}{2}(\phi_p - \phi_o) + \sec \tfrac{1}{2}(\phi_p + \phi_o)\right] (s^d)^{-\frac{1}{2}}\, e^{-iks^d}$$

evaluated at $\phi_p = \phi_o = 0$ and $s^d = 2a$. So

$$x = -\frac{2e^{-ik2a}}{\sqrt{8i\pi k2a}} \tag{46}$$

and

$$x^2 = \frac{e^{-ik4a}}{4i\pi ka} \tag{47}$$

This gives

$$E_H^M \sim \left\{ 16\, E_o \frac{e^{-ik2a}}{\sqrt{8i\pi k2a}} \frac{e^{-ik\rho}}{\sqrt{8i\pi k\rho}} \frac{1}{\cos\phi} - 16\, E_o \left(\frac{e^{-ik2a}}{\sqrt{8i\pi k2a}}\right)^2 \frac{e^{-ik\rho}}{\sqrt{8i\pi k\rho}} \left[\frac{e^{2ikasin\phi}}{1 - \sin\phi} + \frac{e^{-2ikasin\phi}}{1 + \sin\phi}\right]\right\} \left(1 - \frac{e^{-ik4a}}{4i\pi ka}\right)^{-1} \tag{48}$$

Thus the total backscattered field for the plate for horizontal polarisation is

$$E_H^{tot} \sim -2E_o \frac{e^{-ik\rho}}{\sqrt{8i\pi k\rho}} K_2 \tag{49(a)}$$

where

$$K_2 = \cos(2kasin\phi) - 2ika \frac{\sin(2kasin\phi)}{2kasin\phi} - 8 \frac{e^{-ik2a}}{\sqrt{8i\pi k2a}} \left(1 - \frac{e^{-ik4a}}{4i\pi ka}\right)^{-1} \left\{\frac{1}{\cos\phi} - \frac{e^{-ik2a}}{\sqrt{8i\pi k2a}} \left[\frac{e^{2ikasin\phi}}{1 - \sin\phi} + \frac{e^{-2ikasin\phi}}{1 + \sin\phi}\right]\right\} \tag{49(b)}$$

The area backscatter radar cross section of the rectangular plate for horizontal polarisation is then

$$\sigma_H^{GTD} = \frac{4b^2}{\pi} |K_2|^2 \tag{50}$$

3.3 Backscattering from a rectangular cylinder

The rectangular cylinder is shown in figure 2. A view of it in the azimuthal plane is shown in figure 6. Three diffracting edges AE, BF and CG contribute to the backscattered field for the rectangular cylinder. From the results of the flat plate it was seen that for vertical polarisation the doubly diffracted field which results from the higher order slope diffraction term (of order k^{-2}) is weak in comparison with the singly diffracted field of order $k^{-\frac{1}{2}}$. Thus for vertical polarisation only the singly diffracted field needs to be considered. For horizontal polarisation, the singly diffracted field is of order $k^{-\frac{1}{2}}$ while the doubly and triply diffracted fields are of order k^{-1} and $k^{-3/2}$ respectively. Hence multiply diffracted fields need only be considered for horizontal polarisation. The technique used to handle multiply diffracted fields in Section 3.2 proved rather cumbersome and would be even more so for the

rectangular cylinder. Rudduck(ref.7) has pointed out a much more elegant way of computing the nett multiply diffracted field. This approach, known as the self-consistent field method is employed here to calculate the multiply diffracted field for the case of horizontal polarisation.

3.3.1 Vertical polarisation

The diffracted field for normal incidence of a vertically polarised plane wave on the straight edge of a wedge of angle $\frac{\pi}{2}$ is(ref.6),

$$E_v(s^d) \sim D^e E_v^i(P_o)(s^d)^{-\frac{1}{2}} e^{-iks^d} \tag{51}$$

where

$$D^e(\phi_P,\phi_o) = \frac{2\sqrt{3}}{3\sqrt{8i\pi k}} \left\{ \left[\cos\frac{2\pi}{3} - \cos\frac{2}{3}(\phi_P - \phi_o)\right]^{-1} - \left[\cos\frac{2\pi}{3} - \cos\frac{2}{3}(\phi_P + \phi_o)\right]^{-1} \right\} \tag{52}$$

is Keller's diffraction coefficient for vertical polarisation for a wedge of angle $\frac{\pi}{2}$, ϕ_o is the incident angle measured from one of the wedge faces and ϕ_P is the angle of the diffracted ray measured from the same wedge face. Referring to figure 6, the singly diffracted far field from A', B' and C' can be calculated using equations (51) and (52) with the following information for A', B' and C':

TABLE 1. EXPRESSIONS FOR INCIDENT FIELD, DIFFRACTING ANGLE AND DISTANCE TO THE FAR-FIELD POINT FOR DIFFRACTING POINTS A', B' AND C'

A'	$s^d = \rho + a\sin\phi - c\cos\phi$	$\phi_{A'} = \phi_o = \frac{\pi}{2} - \phi$	$E^i(A') = E_o\, e^{-ik(a\sin\phi - c\cos\phi)}$
B'	$s^d = \rho - a\sin\phi - c\cos\phi$	$\phi_{B'} = \phi_o = \frac{\pi}{2} + \phi$	$E^i(B') = E_o\, e^{ik(a\sin\phi + c\cos\phi)}$
C'	$s^d = \rho - a\sin\phi + c\cos\phi$	$\phi_{C'} = \phi_o = \phi$	$E^i(C') = E_o\, e^{ik(a\sin\phi - c\cos\phi)}$

The phase of the incident wave is referred to the coordinate origin, O. ρ is the distance between O and the field point and for far field, $\rho \gg a\sin\phi$, $\rho \gg c\cos\phi$. The total singly diffracted field for vertical polarisation is

$$E_v \sim \frac{2\sqrt{3}}{3} E_o \frac{e^{-ik\rho}}{\sqrt{8i\pi k\rho}} F \tag{53}$$

where

$$F = -\frac{4}{3}\cos(2ka\sin\phi)\, e^{2ikc\cos\phi} + \frac{e^{2ikc\cos\phi}}{2\sin\frac{2\phi}{3}}\left[\frac{e^{-2ika\sin\phi}}{\sin\frac{2}{3}(\pi-\phi)} - \frac{e^{2ika\sin\phi}}{\sin\frac{2}{3}(\pi+\phi)}\right] + e^{2ik(a\sin\phi - c\cos\phi)}\left[-\frac{2}{3} + \frac{1}{2\sin\frac{1}{3}(\pi+2\phi)\sin\frac{1}{3}(\pi-2\phi)}\right] \tag{54}$$

The monostatic radar cross section per unit length for vertical polarisation is given by

$$\sigma_v(\text{length}) = \lim_{\rho\to\infty} 2\pi\rho\left|\frac{E_v}{E_o}\right|^2 = \frac{|F|^2}{3k} \tag{55}$$

so the area monostatic radar cross section is

$$\sigma_v^{GTD} = \frac{4b^2}{3\pi}|F|^2 \tag{56}$$

3.3.2 Horizontal polarisation

The diffracted field for normal incidence of a horizontally polarised plane wave on the straight edge of a wedge of angle $\frac{\pi}{2}$ is(ref.6),

$$E_H(s^d) \sim D^m E_H^i(P_o)(s^d)^{-\frac{1}{2}} e^{-iks^d} \tag{57}$$

where

$$D^m(\phi_p,\phi_o) = \frac{2\sqrt{3}}{3\sqrt{8i\pi k}}\left\{\left[\cos\frac{2\pi}{3} - \cos\frac{2}{3}(\phi_p-\phi_o)\right]^{-1} + \left[\cos\frac{2\pi}{3} - \cos\frac{2}{3}(\phi_p+\phi_o)\right]^{-1}\right\} \tag{58}$$

is Keller's diffraction coefficient for horizontal polarisation for a wedge of angle $\frac{\pi}{2}$. The total backscattered field can be represented as the sum of the singly diffracted field and the multiply diffracted fields.

(a) Singly diffracted field

Referring to figure 6 the singly diffracted field is calculated from equations (57) and (58) for A', B', C' with Table 1 giving the required information. Thus the total singly diffracted field for horizontal polarisation is

$$E_H^s \sim \frac{2\sqrt{3}}{3} E_o \frac{e^{-ik\rho}}{\sqrt{8i\pi k\rho}} G_1 \qquad (59(a))$$

where

$$G_1 = -\frac{4}{3} e^{2ikc\cos\phi} \cos(2ka\sin\phi) + \frac{e^{2ikc\cos\phi}}{2\sin\frac{2\phi}{3}} \left[\frac{e^{2ika\sin\phi}}{\sin\frac{2}{3}(\pi+\phi)} - \frac{e^{-2ika\sin\phi}}{\sin\frac{2}{3}(\pi-\phi)} \right] - e^{2ik(a\sin\phi - c\cos\phi)} \left[\frac{2}{3} + \frac{1}{2\sin\frac{1}{3}(\pi+2\phi)\sin\frac{1}{3}(\pi-2\phi)} \right] \qquad (59(b))$$

(b) The self-consistent GTD formulation for the multiply diffracted fields

The multiply diffracted fields result from waves travelling at least once along the surface of the cylinder. There are infinitely many of these waves on each face of the cylinder. The self-consistent GTD concept combines all the waves on each face into two waves travelling in opposite directions with unknown complex amplitudes as shown in figure 7.

The complex amplitudes $C_1, C_2, \ldots C_8$ are determined by a self-consistent field procedure. E_o, the amplitude of the incident wave, is factorised out so that the unknown $\{C_k\}$ result from a unit amplitude incident wave.

At A'

$$C_1 = V_1 + \frac{1}{2} C_3 D^m(0, 0) \frac{e^{-ik2a}}{\sqrt{2a}} + \frac{1}{2} C_4 D^m\left(\frac{3\pi}{2}, 0\right) \frac{e^{-ik2a}}{\sqrt{2a}} \qquad (60(a))$$

V_1 represents the direct source contribution to C_1, that is, the wave diffracted from B' to A' for a unit amplitude wave incident on B', the second term represents the contribution from the wave travelling along surface A' - B' being diffracted at B' to A' and the third term gives the contribution from the wave travelling along surface C' - B' being diffracted at B' to A'. The diffraction coefficient is multiplied by $\frac{1}{2}$ for grazing incidence(ref.6).

Similarly,

$$C_2 = V_2 + \frac{1}{2} C_8 D^m(0, 0) \frac{e^{-ik2c}}{\sqrt{2c}} + \frac{1}{2} C_7 D^m\left(\frac{3\pi}{2}, 0\right) \frac{e^{-ik2c}}{\sqrt{2c}} \qquad (60(b))$$

At B'

$$C_3 = V_3 + \frac{1}{2} C_1 D^m(0, 0) \frac{e^{-ik2a}}{\sqrt{2a}} + \frac{1}{2} C_2 D^m\left(\frac{3\pi}{2}, 0\right) \frac{e^{-ik2a}}{\sqrt{2a}} \qquad (60(c))$$

$$C_4 = V_4 + \frac{1}{2} C_5 D^m(0, 0) \frac{e^{-ik2c}}{\sqrt{2c}} + \frac{1}{2} C_6 D^m\left(\frac{3\pi}{2}, 0\right) \frac{e^{-ik2c}}{\sqrt{2c}} \qquad (60(d))$$

At C',

$$C_5 = V_5 + \frac{1}{2} C_4 D^m(0, 0) \frac{e^{-ik2c}}{\sqrt{2c}} + \frac{1}{2} C_3 D^m\left(\frac{3\pi}{2}, 0\right) \frac{e^{-ik2c}}{\sqrt{2c}} \qquad (60(e))$$

$$C_6 = V_6 + \frac{1}{2} C_7 D^m(0, 0) \frac{e^{-ik2a}}{\sqrt{2a}} + \frac{1}{2} C_8 D^m\left(\frac{3\pi}{2}, 0\right) \frac{e^{-ik2a}}{\sqrt{2a}} \qquad (60(f))$$

At D',

$$C_7 = V_7 + \frac{1}{2} C_6 D^m(0, 0) \frac{e^{-ik2a}}{\sqrt{2a}} + \frac{1}{2} C_5 D^m\left(\frac{3\pi}{2}, 0\right) \frac{e^{-ik2a}}{\sqrt{2a}} \qquad (60(g))$$

$$C_8 = V_8 + \frac{1}{2} C_2 D^m(0, 0) \frac{e^{-ik2c}}{\sqrt{2c}} + \frac{1}{2} C_1 D^m\left(\frac{3\pi}{2}, 0\right) \frac{e^{-ik2c}}{\sqrt{2c}} \qquad (60(h))$$

The waves excited by the incident wave are given by

$$V_1 = e^{ik(a\sin\phi + c\cos\phi)} D^m\left(0, \frac{\pi}{2} + \phi\right) \frac{e^{-ik2a}}{\sqrt{2a}} \qquad (61(a))$$

$$V_2 = 0 \qquad (61(b))$$

$$V_3 = e^{-ik(a\sin\phi - c\cos\phi)} D^m\left(0, \frac{\pi}{2} - \phi\right) \frac{e^{-ik2a}}{\sqrt{2a}} \qquad (61(c))$$

$$V_4 = e^{ik(a\sin\phi - c\cos\phi)} D^m(0, \phi) \frac{e^{-ik2c}}{\sqrt{2c}} \qquad (61(d))$$

$$V_5 = e^{ik(a\sin\phi + c\cos\phi)} D^m(0, \pi - \phi) \frac{e^{-ik2c}}{\sqrt{2c}} \qquad (61(e))$$

$$V_6 = 0 \qquad (61(f))$$

$$V_7 = e^{ik(a\sin\phi - c\cos\phi)} D^m\left(0, \frac{3\pi}{2} - \phi\right) \frac{e^{-ik2a}}{\sqrt{2a}} \qquad (61(g))$$

$$V_8 = e^{-ik(a\sin\phi - c\cos\phi)} D^m(0, \pi + \phi) \frac{e^{-ik2c}}{\sqrt{2c}} \qquad (61(h))$$

Equation (60) can be written in matrix form,

$$\underset{\sim}{TC} = \underset{\sim}{V} \tag{62}$$

where

$$T = \begin{bmatrix} 1 & 0 & T1 & T2 & 0 & 0 & 0 & 0 \\ 0 & 1 & 0 & 0 & 0 & 0 & T4 & T3 \\ T1 & T2 & 1 & 0 & 0 & 0 & 0 & 0 \\ 0 & 0 & 0 & 1 & T3 & T4 & 0 & 0 \\ 0 & 0 & T4 & T3 & 1 & 0 & 0 & 0 \\ 0 & 0 & 0 & 0 & 0 & 1 & T1 & T2 \\ 0 & 0 & 0 & 0 & T2 & T1 & 1 & 0 \\ T4 & T3 & 0 & 0 & 0 & 0 & 0 & 1 \end{bmatrix}, \tag{63(a)}$$

$$C = \begin{bmatrix} C_1 \\ C_2 \\ C_3 \\ C_4 \\ C_5 \\ C_6 \\ C_7 \\ C_8 \end{bmatrix}, \tag{63(b)}$$

$$V = \begin{bmatrix} V_1 \\ V_2 \\ V_3 \\ V_4 \\ V_5 \\ V_6 \\ V_7 \\ V_8 \end{bmatrix} \tag{63(c)}$$

and

$$T1 = \frac{1}{2} D^{m}(0, 0) \frac{e^{-ik2a}}{\sqrt{2a}}, \tag{64(a)}$$

$$T2 = \frac{1}{2} D^{m}\left(\frac{3\pi}{2}, 0\right) \frac{e^{-ik2a}}{\sqrt{2a}}, \tag{64(b)}$$

$$T3 = \frac{1}{2} D^{m}(0, 0) \frac{e^{-ik2c}}{\sqrt{2c}}, \tag{64(c)}$$

$$T4 = \frac{1}{2} D^{m}\left(\frac{3\pi}{2}, 0\right) \frac{e^{-ik2c}}{\sqrt{2c}}. \tag{64(d)}$$

The unknown complex amplitudes can then be solved by matrix inversion,

$$\underset{\sim}{C} = \underset{\sim}{T}^{-1}\underset{\sim}{V} \tag{65}$$

The total backscattered field. E_H^M, from these waves diffracted at A', B' and C' is

$$E_H^M \sim E_o \frac{e^{-ik\rho}}{\sqrt{\rho}} G_2 \tag{66(a)}$$

where

$$\begin{aligned} G_2 = \frac{1}{2} \Bigg\{ & \left[C_1 D^m\left(\frac{\pi}{2} - \phi, 0\right) + C_2 D^m(\pi + \phi, 0) \right] e^{-ik(a\sin\phi - c\cos\phi)} \\ & + \left[C_3 D^m\left(\frac{\pi}{2} + \phi, 0\right) + C_4 D^m(\pi - \phi, 0) \right] e^{ik(a\sin\phi + c\cos\phi)} \\ & + \left[C_5 D^m(\phi, 0) + C_6 D^m\left(\frac{3\pi}{2} - \phi, 0\right) \right] e^{ik(a\sin\phi - c\cos\phi)} \Bigg\} \end{aligned} \tag{66(b)}$$

(c) The total backscattered field

The total backscattered field is defined by $E_H^{tot} = E_H^S + E_H^M$, that is,

$$E_H^{tot} \sim E_o \frac{e^{-ik\rho}}{\sqrt{\rho}} \left[\frac{G_1}{\sqrt{6i\pi k}} + G_2 \right] \tag{67}$$

The area monostatic radar cross for horizontal polarisation can then be written

$$\sigma_H^{GTD} = 8b^2 k \left| \frac{G_1}{\sqrt{6i\pi k}} + G_2 \right|^2 \tag{68}$$

4. SCATTERING ANALYSIS USING THE KOUYOUMJIAN-PATHAK UNIFORM GEOMETRICAL THEORY OF DIFFRACTION

4.1 The uniform geometrical theory of diffraction

GTD, as originally developed by Keller, fails in the transition regions adjacent to shadow and reflection boundaries where the solution becomes infinite and discontinuous. Kouyoumjian and Pathak(ref.8) modified Keller's diffraction coefficients in the GTD solution by a multiplication factor involving a Fresnel integral. When the observation point is close to a shadow boundary, the modification factor approaches zero so as to compensate for the singularity in Keller's diffraction coefficients, and to give rise to a finite field solution there. They refer to this approach as the uniform GTD or UTD, a name adopted here to distinguish it from GTD with Keller's diffraction coefficients.

For normal incidence on a wedge with exterior angle $n\pi$, the Kouyoumjian-Pathak diffraction coefficients D^e, D^m for vertical and horizontal polarisation respectively are

$$D^{e,m}(L, \phi_p, \phi_o) = -\frac{e^{-i\pi/4}}{2n\sqrt{2\pi k}} \left\{ \cot\left(\frac{\pi + \beta^-}{2n}\right) F(kLa^+(\beta^-)) + \cot\left(\frac{\pi - \beta^-}{2n}\right) F(kLa^-(\beta^-)) \mp \left[\cot\left(\frac{\pi + \beta^+}{2n}\right) F(kLa^+(\beta^+)) + \cot\left(\frac{\pi - \beta^+}{2n}\right) F(kLa^-(\beta^+)) \right] \right\} \tag{69}$$

where

$$\beta^- = \phi_p - \phi_o,$$

$$\beta^+ = \phi_p + \phi_o,$$

ϕ_p, ϕ_o as defined in Section 3.

$$F(x) = 2i\sqrt{x}\, e^{ix} \int_{\sqrt{x}}^{\infty} e^{-i\tau^2}\, d\tau; \tag{70}$$

$$a^{\pm}(\beta) = 2\cos^2 \frac{2\pi n N^{\pm} - \beta}{2} \tag{71}$$

in which $N^{\pm}$ are the integers which most nearly satisfy the equations

$$2\pi n N^+ - \beta = \pi, \tag{72(a)}$$

$$2\pi n N^- - \beta = -\pi. \tag{72(b)}$$

L is the distance parameter given by

$$L = \begin{cases} s^d & \text{for plane-wave normal incidence} \\ \dfrac{rr'}{r + r'} & \text{for cylindrical-wave incidence} \\ \dfrac{s^d s^i}{s^d + s^i} & \text{for conical- and spherical-wave normal incidence} \end{cases} \tag{73}$$

where s^i is the distance of the source point to the diffraction point, s^d is the distance of the field point to the diffraction point, r' is the radius of the incident cylindrical wave and r is the perpendicular distance of the field point from the edge.

If the arguments of the four transition functions in equation (69) exceed ~10, the transition functions are approximately equal to one and equation (69) reduces to Keller's diffraction coefficients.

4.2 Backscattering from a rectangular flat plate

The UTD backscattered radar cross section of the rectangular flat plate is derived here. As discussed in Section 3.3 multiply diffracted fields are only significant for horizontal polarisation. In handling the multiply diffracted fields for horizontal polarisation, the more elegant self-consistent field method is employed.

For diffraction from a half-plane, n = 2 and the diffraction coefficients in equation (69) reduce to

$$D^{e,m}(L, \phi_p, \phi_o) = -\frac{e^{-i\pi/4}}{2\sqrt{2\pi k}}\left[\frac{F(kLa(\beta^-))}{\cos(\beta^-/2)} \mp \frac{F(kLa(\beta^+))}{\cos(\beta^+/2)}\right] \tag{74}$$

where

$$a^{\pm}(\beta) = a(\beta) = 2\cos^2(\beta/2).$$

4.2.1 Vertical polarisation

The multiply diffracted fields are negligible. The singly diffracted fields from edges A' and B' (figure 3) are given by equation (11) with D^e as defined in equation (74). The distance parameter L for plane wave incidence and far-field backscattered field is very large so that the Kouyoumjian-Pathak diffraction coefficient reduces to that of Keller. The singly diffracted field is thus given by equation (16) and the area backscatter radar cross section is

$$\sigma_v^{UTD} = \frac{4b^2}{\pi}\left|\cos(2ka\sin\phi) + 2ika\,\frac{\sin(2ka\sin\phi)}{2ka\sin\phi}\right|^2 \tag{75}$$

4.2.2 Horizontal polarisation

(a) Singly diffracted field

As in Section 4.2.1, the singly diffracted field is the same as that obtained with Keller's diffraction coefficient. Thus the singly diffracted field E_H^S is given by equation (39).

(b) The self-consistent UTD formulation for the multiply diffracted fields

The diffracted waves travelling in opposite directions with unknown complex amplitudes $C_1 E_o$, $C_3 E_o$ on one side of the strip and $C_2 E_o$, $C_4 E_o$ on the back side of the strip are illustrated in figure 8.

At B'

$$C_1 = e^{-ikasin\phi}\, D^m\left(2a,0,\frac{\pi}{2} - \phi\right)\frac{e^{-ik2a}}{\sqrt{2a}} + \frac{1}{2}\left[C_3\, D^m(a,0,0) + C_4\, D^m(a,2\pi,0)\right]\frac{e^{-ik2a}}{\sqrt{2a}} \tag{76(a)}$$

$$C_2 = e^{-ikasin\phi}\, D^m\left(2a,2\pi,\frac{\pi}{2} - \phi\right)\frac{e^{-ik2a}}{\sqrt{2a}} + \frac{1}{2}\left[C_4\, D^m(a,0,0) + C_3\, D^m(a,2\pi,0)\right]\frac{e^{-ik2a}}{\sqrt{2a}} \tag{76(b)}$$

At A',

$$C_3 = e^{ikasin\phi}\, D^m\left(2a,0,\frac{\pi}{2} + \phi\right)\frac{e^{-ik2a}}{\sqrt{2a}} + \frac{1}{2}\left[C_1\, D^m(a,0,0) + C_2\, D^m(a,2\pi,0)\right]\frac{e^{-ik2a}}{\sqrt{2a}} \tag{76(c)}$$

$$C_4 = e^{ikasin\phi}\, D^m\left(2a,2\pi,\frac{\pi}{2} + \phi\right)\frac{e^{-ik2a}}{\sqrt{2a}} + \frac{1}{2}\left[C_2\, D^m(a,0,0) + C_1\, D^m(a,2\pi,0)\right]\frac{e^{-ik2a}}{\sqrt{2a}} \tag{76(d)}$$

From equation (74), it is seen that

$$D^m(a,0,0) = -D^m(a,2\pi,0),$$

$$D^m\left(2a,0,\frac{\pi}{2} - \phi\right) = -D^m\left(2a,2\pi,\frac{\pi}{2} - \phi\right) \text{ and}$$

$$D^m\left(2a,0,\frac{\pi}{2} + \phi\right) = -D^m\left(2a,2\pi,\frac{\pi}{2} + \phi\right).$$

Substituting these into equation (76) gives $C_1 = -C_2$, $C_3 = -C_4$ and the following equations for C_1 and C_3,

$$C_1 = e^{-ikasin\phi}\, D^m\left(2a,0,\frac{\pi}{2} - \phi\right)\frac{e^{-ik2a}}{\sqrt{2a}} + C_3\, D^m(a,0,0,)\,\frac{e^{-ik2a}}{\sqrt{2a}} \tag{77(a)}$$

$$C_3 = e^{ikasin\phi}\, D^m\left(2a,0,\frac{\pi}{2} + \phi\right)\frac{e^{-ik2a}}{\sqrt{2a}} + C_1\, D^m(a,0,0)\,\frac{e^{-ik2a}}{\sqrt{2a}} \tag{77(b)}$$

Solution of equation (77) yields

$$C_1 = \frac{X + ZY}{1 - Z^2}, \tag{78(a)}$$

$$C_3 = \frac{Y + ZX}{1 - Z^2} \tag{78(b)}$$

where

$$X = e^{-ika\sin\phi}\, D^m\left(2a, 0, \frac{\pi}{2} - \phi\right) \frac{e^{-ik2a}}{\sqrt{2a}}, \tag{78(c)}$$

$$Y = e^{ika\sin\phi}\, D^m\left(2a, 0, \frac{\pi}{2} + \phi\right) \frac{e^{-ik2a}}{\sqrt{2a}}, \tag{78(d)}$$

$$Z = D^m(a,0,0) \frac{e^{-ik2a}}{\sqrt{2a}}. \tag{78(e)}$$

From B', the multiply diffracted field in the backscattered direction is

$$E_H^{M1} \sim \frac{1}{2}\left[C_1 E_o\, D^m\left(2a, \frac{\pi}{2} + \phi, 0\right) + C_2 E_o\, D^m\left(2a, \frac{3\pi}{2} - \phi, 0\right)\right] \frac{e^{-ik(\rho - a\sin\phi)}}{\sqrt{\rho}} \tag{79(a)}$$

and from A',

$$E_H^{M2} \sim \frac{1}{2}\left[C_3 E_o\, D^m\left(2a, \frac{\pi}{2} - \phi, 0\right) + C_4 E_o\, D^m\left(2a, \frac{3\pi}{2} + \phi, 0\right)\right] \frac{e^{-ik(\rho + a\sin\phi)}}{\sqrt{\rho}} \tag{79(b)}$$

But $C_1 = -C_2$, $C_3 = -C_4$ and equation (74) gives

$$D^m\left(2a, \frac{\pi}{2} + \phi, 0\right) = -D^m\left(2a, \frac{3\pi}{2} - \phi, 0\right)$$

$$D^m\left(2a, \frac{\pi}{2} - \phi, 0\right) = -D^m\left(2a, \frac{3\pi}{2} + \phi, 0\right).$$

Thus

$$E_H^{M1} \sim C_1 E_o\, D^m\left(2a, \frac{\pi}{2} + \phi, 0\right) \frac{e^{-ik\rho}}{\sqrt{\rho}}\, e^{ika\sin\phi}, \tag{80(a)}$$

$$E_H^{M2} \sim C_3 E_o\, D^m\left(2a, \frac{\pi}{2} - \phi, 0\right) \frac{e^{-ik\rho}}{\sqrt{\rho}}\, e^{-ika\sin\phi}. \tag{80(b)}$$

The total backscattered field from multiply diffracted rays is

$$E_H^M \sim E_o \frac{e^{-ik\rho}}{\sqrt{\rho}} \left[C_1 \, D^m\left(2a, \frac{\pi}{2} + \phi, 0\right) e^{ika\sin\phi} + C_3 \, D^m\left(2a, \frac{\pi}{2} - \phi, 0\right) e^{-ika\sin\phi} \right] \tag{81}$$

(c) The total backscattered field

The total backscattered field, E_H^{tot}, is the sum of the singly and multiply diffracted fields,

$$E_H^{tot} \sim E_o \frac{e^{-ik\rho}}{\sqrt{\rho}} Q \tag{82(a)}$$

where

$$Q = -\frac{1}{\sqrt{2i\pi k}} \left[\cos(2ka\sin\phi) - \frac{2ika\sin(2ka\sin\phi)}{2ka\sin\phi} \right]$$

$$+ C_1 \, D^m\left(2a, \frac{\pi}{2} + \phi, 0\right) e^{ika\sin\phi} + C_3 \, D^m\left(2a, \frac{\pi}{2} - \phi, 0\right) e^{-ika\sin\phi}, \tag{82(b)}$$

C_1 and C_3 are given by equation (78).

The area backscatter radar cross section for horizontal polarisation is then given by

$$\sigma_H^{UTD} = 8kb^2 |Q|^2 \tag{83}$$

4.3 Backscattering from a rectangular cylinder

The UTD backscatter radar cross sections for the rectangular cylinder (figures 2 and 6) are derived here. The derivation follows that of Section 3.3 closely with the diffraction coefficients of Kouyoumjian and Pathak (equation (69)) used instead of those of Keller. The wedge angle in this case is $\frac{\pi}{2}$ so that $n\pi = \frac{3\pi}{2}$.

4.3.1 Vertical polarisation

Only singly diffracted field contributions are significant. As in Section 4.2, the Kouyoumjian-Pathak diffraction coefficient reduces to the Keller diffraction coefficient for far-field backscattered singly diffracted fields so that the backscattered radar cross section is the same as that given by equation (56), that is,

$$\sigma_V^{UTD} = \frac{4b^2}{3\pi} |F|^2 \tag{84}$$

with F defined in equation (54).

4.3.2 Horizontal polarisation

The singly diffracted field is again the same as that derived using Keller's diffraction coefficient and is given by equation (59).

The multiply diffracted fields (figure 7) are as given by equation (65) with the elements of matrices $\underset{\sim}{V}$ and $\underset{\sim}{T}$ now defined by

$$V_1 = e^{ik(a\sin\phi + c\cos\phi)}\, D^m\left(2a, 0, \frac{\pi}{2} + \phi\right) \frac{e^{-ik2a}}{\sqrt{2a}}, \tag{85(a)}$$

$$V_2 = 0, \tag{85(b)}$$

$$V_3 = e^{-ik(a\sin\phi - c\cos\phi)}\, D^m\left(2a, 0, \frac{\pi}{2} - \phi\right) \frac{e^{-ik2a}}{\sqrt{2a}}, \tag{85(c)}$$

$$V_4 = e^{ik(a\sin\phi - c\cos\phi)}\, D^m(2c, 0, \phi) \frac{e^{-ik2c}}{\sqrt{2c}}, \tag{85(d)}$$

$$V_5 = e^{ik(a\sin\phi + c\cos\phi)}\, D^m(2c, 0, \pi - \phi) \frac{e^{-ik2c}}{\sqrt{2c}}, \tag{85(e)}$$

$$V_6 = 0, \tag{85(f)}$$

$$V_7 = e^{ik(a\sin\phi - c\cos\phi)}\, D^m\left(2a, 0, \frac{3\pi}{2} - \phi\right) \frac{e^{-ik2a}}{\sqrt{2a}}, \tag{85(g)}$$

$$V_8 = e^{-ik(a\sin\phi - c\cos\phi)}\, D^m(2c, 0, \pi + \phi) \frac{e^{-ik2c}}{\sqrt{2c}}, \tag{85(h)}$$

$$T1 = \frac{1}{2} D^m(a, 0, 0) \frac{e^{-ik2a}}{\sqrt{2a}}, \tag{86(a)}$$

$$T2 = \frac{1}{2} D^m\left(\frac{2ac}{a + c}, \frac{3\pi}{2}, 0\right) \frac{e^{-ik2a}}{\sqrt{2a}}, \tag{86(b)}$$

$$T3 = \frac{1}{2} D^m(c, 0, 0) \frac{e^{-ik2c}}{\sqrt{2c}}, \tag{86(c)}$$

$$T4 = \frac{1}{2} D^m\left(\frac{2ac}{a + c}, \frac{3\pi}{2}, 0\right) \frac{e^{-ik2c}}{\sqrt{2c}}. \tag{86(d)}$$

The multiply diffracted field in the backscattered direction is

$$E_H^M \sim E_o \frac{e^{-ik\rho}}{\sqrt{\rho}} G_3 \qquad (87(a))$$

where

$$G_3 = \frac{1}{2}\left\{\left[C_1 D^m\left(2a,\frac{\pi}{2}-\phi,0\right) + C_2 D^m(2c,\pi+\phi,0)\right] e^{-ik(a\sin\phi - c\cos\phi)}\right.$$

$$+\left[C_3 D^m\left(2a,\frac{\pi}{2}+\phi,0\right) + C_4 D^m(2c,\pi-\phi,0)\right] e^{ik(a\sin\phi + c\cos\phi)}$$

$$\left.+\left[C_5 D^m(2c,\phi,0) + C_6 D^m\left(2a,\frac{3\pi}{2}-\phi,0\right)\right] e^{ik(a\sin\phi - c\cos\phi)}\right\} \qquad (87(b))$$

The total backscattered field is thus

$$E_H^{tot} \sim E_o \frac{e^{-ik\rho}}{\sqrt{\rho}}\left[\frac{G_1}{\sqrt{6i\pi k}} + G_3\right] \qquad (88)$$

where G_1 is as given in equation (59(b)).

The area monostatic radar cross section for horizontal polarisation is then

$$\sigma_H^{UTD} = 8b^2 k\left|\frac{G_1}{\sqrt{6i\pi k}} + G_3\right|^2 \qquad (89)$$

5. EXPERIMENTAL MEASUREMENTS

5.1 The anechoic chamber

The experimental observations carried out to check the theoretical predictions were performed in the DRCS anechoic chamber. This facility has a normal source-target separation of 12 m, a frequency range extending from 2.5 GHz to 40 GHz, and analogue recording of measurements(ref.9).

A problem that has to be combatted in the anechoic chamber measurements is null drift, that is, a drift in the adjustment for background cancellation. This can arise from frequency instability and temperature variation in passive components. The low power returns are especially susceptible to any null drift that occurs as is evident in the high incidence of data asymmetry in the flat plate results, particularly at the lower frequencies, and in the 10 cm cylinder at 4 GHz for vertical polarisation.

In general the performance of the chamber improves with increasing frequency because the antenna gains are higher, the antenna beamwidths are narrower so that less of the wall is illuminated and the radar absorbent material is more effective. However, there are some isolated narrow bandwidths within the operating frequency range for which the chamber performance is uncharacteristically poor. The 12 GHz frequency has been identified as one of them; a dramatic increase in background noise being experienced at the time of measurements at this frequency.

Apart from the poor chamber performance another contributing factor to the unreliable results at 12 GHz could be the frequency instability of the Klystron oscillator used. Frequency instability increases with frequency and will result in null drift problems. Some of the 10 GHz results seem to be similarly affected, the 10 GHz and 12 GHz measurements are done using the same Klystron oscillator while the 4 to 8 GHz measurements are done using another*.

As the operating frequency increases other problems are decreased sensitivity of the receiver and components and greater attenuation in the cables.

5.2 Flat plate experiments

The flat plate measurements were conducted using a brass rectangular plate 10 cm x 10 cm and thickness 1 mm (figure 1). Five frequencies were employed, viz 4, 6, 8, 10 and 12 GHz, corresponding to values of $\frac{2a}{\lambda}$ as shown in Table 2. Measurements were made over the range -90° to +90° so that symmetry could be used to assess system errors. The analogue X-Y plotter output was sampled at 2° intervals for analysis.

TABLE 2. DIMENSIONS OF FLAT PLATES IN TERMS OF WAVELENGTH

Frequency (GHz)	4	6	8	10	12
Ratio of side of plate to wavelength, $\frac{2a}{\lambda}$	1.3	2.0	2.7	3.3	4.0

5.3 Rectangular cylinder measurements

The method adopted in the theoretical analysis using the Geometrical Theory of Diffraction ignores diffraction from the ends of the cylinder. In order to assess the significance of this effect, three cylinders of equal cross sections 10 cm x 10 cm but with lengths 10, 30 and 50 cm were used. The cylinders were fabricated of brass of thickness 1 mm to a nominal tolerance of 0.5 mm.

Again, five frequencies were employed, namely, 4, 6, 8, 10 and 12 GHz. The dimensions of the targets in terms of incident wavelength are given in Table 3. Measurements were made over the range -90° to +90°; the analogue X-Y plotter output was sampled at 2° intervals for analysis.

*. The frequency stability has since been improved by phase locking the Klystron to a stable source.

TABLE 3. DIMENSIONS OF RECTANGULAR CYLINDER IN TERMS OF WAVELENGTH

Frequency (GHz)	Ratio of width of cylinder to wavelength, $\frac{2a}{\lambda}$	Ratio of length of cylinder to wavelength, $\frac{2b}{\lambda}$		
		Length of cylinder, 2b (cm)		
		10	30	50
4	1.3	1.3	4.0	6.67
6	2.0	2.0	6.0	10.0
8	2.7	2.7	8.0	13.3
10	3.3	3.3	10.0	16.7
12	4.0	4.0	12.0	20.0

5.4 Asymmetry of anechoic chamber measurements

One of the features of the anechoic chamber measurements presented in figures 9 to 48 is the occasional asymmetry between the 0 to 90° data and the 0 to -90° data. The models were not of high quality machine-shop standard so a certain amount of asymmetry was anticipated but several of the RCS patterns for the flat plate show inexplicable variations. Possible explanations for these variations include (i) model construction errors, such as curvature resulting in focussing effects, (ii) errors in mounting the models vertically in the chamber, leading to sampling over oblique $\theta - \phi$ arcs, (iii) errors in orienting the model at $\phi = 0°$ leading to a translation of the pattern across ϕ (see figure 31), (iv) null drift problems discussed in Section 5.1 and (v) errors introduced by the analogue plotting equipment.

Of these, (v) is believed to be most unlikely while the effect of null drift is expected to be more significant at the lower frequencies, 4 to 6 GHz, when power returns are low. (iii) could explain small deviations but not the larger ones. (i) would be an appealing solution were it not for the fact that for both flat plate and cylinder, the errors are greatest at 4 GHz, decreasing through 6 GHz to only ~2 dB for most measurements at 8 GHz and 10 GHz, but increasing again at 12 GHz. If the 12 GHz results are discounted because of the poorer performance of the chamber at 12 GHz, neither (i), (ii) nor (iii) would seem to account for the asymmetry because errors in θ and ϕ would be much more critical owing to the finer lobe structure at higher frequencies. Thus the most likely explanation of the discrepancies is unidentified problems with the anechoic chamber itself.

Unfortunately other demands on the anechoic chamber resources made a second series of measurements out of the question so the analysis has been undertaken in the knowledge that the deviations from symmetry may well reflect a variety of errors as discussed above. The majority of the measured data shows no significant asymmetry (compared with the variations of RCS with ϕ), however, so there seems to be a strong case for retaining the experimental points for comparison with the theoretical results.

6. RESULTS

6.1 Flat plate

6.1.1 Vertical polarisation

At 4 GHz the PO, GTD, UTD and anechoic chamber (AC) estimates agree to within 1 dB out to about 15° from normal incidence, after which the theoretical values depart grossly from the measured RCS (figure 9). The AC values are symmetric within ±2 dB, increasing confidence in their accuracy. The 6 GHz AC measurements are, by contrast, in fair agreement with PO, GTD and UTD out to 45° (figure 10). Beyond 45° the 0 to 90° AC values diverge significantly from the 0 to -90° AC values, differing by 14 dB at 62°. The UTD estimates near grazing incidence agree best with AC values, PO grossly underestimates it while GTD is singular there.

The agreement between AC, GTD and UTD values at 8 GHz is excellent out to 55° where measurements show a shallow minimum which is not predicted by GTD, UTD or PO (figure 11). Again UTD succeeds best near grazing incidence while PO and GTD exhibits the same problems as at 6 GHz. At 10 GHz agreement between UTD and AC is within ±2 dB over the entire range (figure 12) while GTD only fails near grazing incidence. The 12 GHz results (figure 13) are in conflict with the trend shown from 4 to 10 GHz. As mentioned in Section 5.4, the 12 GHz AC data is unreliable and so this deviation from the observed trend may be an artifact.

In all cases reviewed above, PO consistently underestimates the RCS for aspect angles away from broadside, in addition to predicting unphysical nulls. The GTD and UTD solutions are identical up to within 10° or, in some cases 5° of grazing incidence. The infinite fields predicted by GTD at grazing incidence are unphysical whereas those predicted by UTD remain finite and agree with AC values to within ±3 dB at 6, 8 and 10 GHz.

6.1.2 Horizontal polarisation

PO solutions for convex targets are independent of polarisation; this is not the case for GTD and UTD.

The 4 GHz results show an agreement between theory and experiment out to 18°, beyond that to 70° the GTD and UTD solutions match the AC values to within ±8 dB (figure 14). Beyond 70° UTD and PO values decrease very rapidly while AC values remain fairly constant and GTD becomes singular at grazing incidence. Again the AC values show marked asymmetry, similar to that obtained for vertical polarisation at 6 GHz with the 0 to 90° measurements up to 11 dB above the 0 to -90° measurements. The values for 6 GHz are also asymmetric but with the 0 to 90° values falling some 10 dB below the 0 to -90° measurements (figure 15). Once again, theoretical estimates fall well below measured values.

At 8 GHz the theoretical and experimental values agree to within ±2 dB over most of the range; interestingly the exceptions to this are the minima at 22° and 48° where the deeper nulls of the PO solution are more suggestive of the AC data than the GTD and UTD solutions which have shallow minima some 8 dB above the measured values (figure 16). Near grazing incidence UTD and PO estimates are well below AC values while GTD values are well above, becoming infinite at grazing incidence.

The AC data at 10 GHz show significantly greater oscillatory behaviour than the GTD and UTD solutions, though the "phase" of the variations is in rough agreement at all angles (figure 17). Asymmetry in the AC data

suggests measurements are affected by the problems discussed in Section 5.4.

Measurements at 12 GHz are in slightly better agreement with the GTD and UTD solutions than the corresponding vertical polarisation values at this frequency but variations of up to 5 dB occur (figure 18). The asymmetry scatter in AC data again calls in question their reliability.

Summarising the results, one can observe that at the lower frequencies systematic AC data structure departs significantly from theoretical predictions. At the intermediate frequencies, 8 and 10 GHz, agreement is generally very good particularly for vertical polarisation. The 12 GHz results are less reliable for the reasons mentioned in Section 5.4.

Except at the lowest frequency, it is true that the PO solutions are satisfactory for representing the main lobe of the pattern, near normal incidence; at higher frequencies reasonable agreement (± several decibels) holds for the second and third lobes as well. Of course, near the minima PO must not be used. At higher frequencies it locates the positions of the minima reasonably well but at low frequencies it fails even to do that.

The GTD solutions have a singularity at grazing incidence, a failure of the method. Apart from angles near edge on, the GTD and UTD solutions are in better agreement with AC measurements virtually everywhere, though at low frequencies discrepancies of 6 to 16 dB occur. At 8 and 10 GHz the GTD and UTD solutions are in excellent agreement with AC data but data unreliability at 12 GHz precludes any extension of the observed trend to that frequency. For angles near grazing incidence GTD fails whereas UTD solutions remain finite; agreement between UTD solutions and AC data is reasonable for vertical polarisation but not so for horizontal polarisation, UTD solutions being much lower than AC data there.

6.2 Rectangular cylinder

6.2.1 Vertical polarisation

For the 10 cm cylinder the AC measurements are up to 12 dB greater than PO, GTD and UTD predictions, though a marked systematic asymmetry in the experimental values accounts for some of this (figure 19). The expected symmetry about 45° is, however, only present in the 0 to 90° measurements which are the ones which differ most from the theoretical curves. The 30 cm cylinder results show agreement to within 2 dB everywhere except at the sharp minima near 22° and 68°, where GTD and UTD are too conservative while PO exaggerates the minima (figure 20). At 50 cm cylinder lengths even the minima are accurately predicted by GTD and UTD, with excellent agreement at all angles (figure 21).

The 6 GHz measurements for the 10 cm cylinder lie well above theoretical predictions at intermediate angles but agree reasonably well near 0°, 45° and 90° (figure 22). It is interesting to note that the AC data show slight maxima around 45° as predicted by PO but not by GTD and UTD. The 30 cm cylinder measurements are in much closer agreement with the GTD and UTD calculations, differing by at most 3 dB (figure 23). PO consistently underestimates the RCS, especially near minima. For the 50 cm cylinder the GTD and UTD solutions match the AC data equally well, to within less than the difference between the 0 to 90° and 0 to -90° measurements (figure 24). The PO disagrees as before.

At 8 GHz the theoretical results for the 10 cm cylinder match well out to 20° where they all underestimate the RCS (figure 25). Near $\phi = 45°$ the GTD and UTD estimates overestimate and predict a shallow minimum; PO is in better agreement over this region but discrepancies of up to 7 dB are present. The reverse is true for the 30 cm cylinder (figure 26). Near $\phi = 45°$ the theoretical results are too low but the GTD and UTD values are only a few decibels in error. The nulls at 11° and 22° and their complementary angles are accurately modelled by GTD and UTD while PO locates them correctly but overestimates their depths. For the 50 cm cylinder GTD and UTD provide accurate solutions at all aspects (figure 27). A slight asymmetry in the experimental results suggests an equipment effect.

Turning to the figures for 10 GHz, the 10 cm cylinder AC measurements show deep nulls at 37° and 53° (45° ± 8°) which are not adequately predicted by PO and are only hinted at by GTD and UTD (figure 28). Elsewhere the agreement between theory and experiment is less satisfactory than at 8 GHz. The 30 cm cylinder results are in much better accord, however, with GTD and UTD estimates within 2 dB of measured values (figure 29). Apart from the nulls, the PO estimates are also good everywhere except near $\phi = 45°$ where they depart from AC data by several decibels. Similar remarks can be made about the 50 cm cylinder RCS pattern at 10 GHz though here one cannot observe any superior performance of GTD and UTD over PO near $\phi = 45°$ (figure 28).

It is apparent that measured values of the RCS of the 10 cm rectangular cylinder at 12 GHz are scattered more widely about the theoretical curves than at lower frequencies (figure 31). The unreliability of the 12 GHz AC data has been noted in Section 5.4.

At a cylinder length of 30 cm the agreement between theory and experiment is certainly not as good as at 10 GHz. The shape of the patterns agree everywhere but deviations of 3 or 4 dB occur for $\phi > 15°$; the scatter in AC data may explain this excursion (figure 32).

The 50 cm cylinder results are similarly slightly less impressive than at lower frequencies but the greater asymmetry in the anechoic chamber data may account for this (figure 33). The PO solutions in this case tend to underestimate the widths of the lobes for $\phi > 20°$.

6.2.2 Horizontal polarisation

The anechoic chamber measurements of the 10 cm cylinder at 4 GHz are generally in better accord with GTD and UTD solutions than was the case for vertical polarisation. The nulls in the pattern are much more pronounced for horizontal polarisation (figure 34). There is reasonable agreement between the UTD solution and AC data in the general shape of the curve, though discrepancies of several decibels are observed and UTD's locations of the nulls are out by ∿3° from AC results. The same is true of GTD solutions except near $\phi = 0°$ and $\phi = 90°$ where GTD solutions are infinite. PO's prediction of the main lobes agrees well with AC data but it fails to describe the behaviour outside the main lobes; in particular, it misses the lobe at 45° entirely.

The AC data for the 30 cm cylinder are marked by four outliers in the 0 to 90° measurements (figure 35). These suggest nulls of 25 dB but the 0 to -90° and theoretical curves are in agreement that the nulls are only ∿15 dB. Apart from these outlier points the AC data is in fair agreement with UTD and with GTD except near the singularities at 0° and 90°. The PO curve is within 1 dB over the main lobes but again PO fails to predict the lobe at 45°.

At a cylinder length of 50 cm, PO again represents the main lobes to within 1 or 2 dB and misses the lobe at 45° (figure 36). UTD and, apart from the effects of the singularities at 0° and 90°, GTD are in good agreement with AC data on the shape of the curve but AC data consistently indicates deeper nulls than predicted by UTD or GTD.

The 6 GHz measurements of the 10 cm cylinder reveal an almost global underestimation of RCS by the theories, ranging from a few decibels around the main lobe for UTD and PO to 10 dB for UTD, 10 dB for GTD and 15 dB for PO near 45° (figure 37), GTD again predicting infinite fields in the main lobes at 0° and 90°. The theories fail to predict curves that agree in shape with that of measurements between 30° and 60°. This is uncharacteristic of the GTD and UTD solutions thus far. While some asymmetry between the 0 to 90° and 0 to -90° measurements is evident for $\phi > 75°$, the theories are clearly inadequate for this case. It is worth noting that the vertical polarisation results showed similar underestimates of the RCS at intermediate angles.

The 30 cm cylinder data are, in contrast, quite well matched by UTD and, apart from the lobe at 45°, by PO (figure 38). GTD besides having singularities at 0° and 90°, estimates broader main lobes than UTD, PO and AC data.

The results for the 50 cm cylinder show excellent agreement between UTD and the AC measurements (figure 39). Again GTD estimates broader main lobes than UTD, PO and AC data.

At 8 GHz the theories exaggerate the second and third nulls somewhat but generally the 10 cm cylinder RCS pattern is quite well modelled (figure 40), especially compared with the performance of the theories at 4 and 6 GHz. UTD and GTD disagree with PO in the location of the second nulls and there is some scatter in the measurements making location of them by the AC data uncertain. UTD's estimates of the first nulls agree very well with AC data, while GTD underestimates them somewhat and PO grossly exaggerates them as it does the second nulls.

The GTD and UTD calculations for the 30 cm cylinder predict a distortion of the second lobe near 22° and 68° which does not appear to be present in the AC data (figure 41). Again UTD has the best estimates of the first nulls while both UTD and GTD underestimate the second nulls and, as before, GTD is singular at 0° and 90°. PO exaggerates the first and second nulls but underestimates the lobes at 30° and 60°.

The situation is much the same for the 50 cm cylinder (figure 42). The distortion of the second lobe is again apparent in the GTD and UTD solutions and some suggestion of a genuine asymmetry near the peak of the lobe is present in the AC data. The match between theory and equipment is quite good elsewhere, within 2 to 3 dB everywhere for UTD except for the second null, within 2 to 3 dB for GTD except for the first and second nulls and near 0° and 90° and within 2 to 4 dB for PO except at the nulls.

The anechoic chamber measurements at 10 GHz for the 10 cm cylinder are somewhat erratically distributed with gross variations between the 0 to 90° and 0 to -90° pattern - in some cases they differ by 18 dB (figure 43). Characterisation of the main lobes (away from 0° and 90° for GTD) is good but the scatter of the measurement makes further interpretation difficult.

More sense can be made of the result for the 30 cm cylinder (figure 44). Here the agreement between theory and experiment is obviously very good, typically ±1 to ±2 dB, with only isolated exceptions. For instance, PO appears to mislocate the null near 29°, placing it at 27° whereas GTD and UTD matches the measured data. GTD underestimates the first nulls while UTD overestimates the second nulls.

The 50 cm cylinder likewise shows very good agreement between UTD and measurements though there is more scatter in the measurements for $\phi > 60°$ (figure 45). Away from 0° and 90°, GTD, apart from underestimating the first nulls, is equally impressive. PO again fails to predict the correct behaviour for 20° to 30° and its image for 70° to 60°. Apart from this, it too agrees well with measurements.

The measurements at 12 GHz for the 10 cm cylinder (figure 46) show a fair amount of scatter between 20° to 70° as is the case for the 10 GHz measurements of the 10 cm cylinder. Outside of the 20° to 70° region, agreement between theories and measurements is good (away from 0° and 90° for GTD). In the 20° to 70° region PO's prediction departs significantly from that of GTD and UTD; in particular the peaks predicted by GTD and UTD at 30° and 60° are missed by PO which places deep nulls there instead. Despite the poor measurements here, more confidence is to be placed in the GTD and UTD results.

The results for the 30 cm cylinder show very good agreement between UTD and AC data apart from an overestimation of the peaks at 30° and 60° by UTD (figure 47). The same is true of GTD away from 0° and 90°. PO overestimates the first two nulls from the main lobes and replaces the peaks at 30° and 60° by deep nulls as before; apart from that, it agrees well with measurements.

The 50 cm cylinder measurements have more scatter, particularly from 70° to 90° (figure 48). Good agreement is obtained between UTD and AC data and, away from 0° and 90°, between GTD and AC data, especially with the 0 to 90° measurements. PO suffers from the same deficiencies as mentioned for the 30 cm cylinder. Nevertheless, the height of the peaks as predicted by PO matches that of measurements better than that of GTD and UTD which overestimate them particularly away from the main lobes directions.

6.3 Comparison with moment method solution

The results obtained in this paper for the flat plate and finite rectangular cylinder using the normalisation scheme through equation (10) must involve termination errors, the significance of which must increase with decreasing plate size and cylinder length. Comparison with experimental results attests to this expected trend in the cylinder case, agreement is good down to a length of 2λ but in the case of the flat plate it is hard to assess the accuracy of the solutions obtained as there is much more scatter in the AC data as has been mentioned in Section 5.4.

In view of the unreliability of the AC data at low power return, the PO and UTD results are compared here with moment method (MM) solutions of the integral equation for the flat plate at 4 GHz, that is, for $\frac{2b}{\lambda} = \frac{2a}{\lambda} = 1.3$. Comparison is not made with GTD as it gives the same results as UTD away from grazing incidence. The MM solutions were obtained using the NEC wire grid modelling code available at DRCS. Agreement between PO and MM solutions is only good for the main lobes, that is, near the specular directions (figures 49 and 50). On the other hand agreement between UTD and MM solutions at 4 GHz is very good - within 1 dB up to 25° and within

2 dB beyond 25° for vertical polarisation (figure 49), within 1 dB up to 40° and within 4 dB beyond 40° for horizontal polarisation (figure 50). These results indicate that termination effects are not significant even for plate lengths as small as 1.3λ.

Figures 51 and 52 compare UTD, PO and MM solutions for the flat plate at 2 GHz, that is, for $\frac{2b}{\lambda} = \frac{2a}{\lambda} = 0.7$, for vertical and horizontal polarisation respectively. At this frequency, even PO's prediction of the specular return from the plate is several decibels out from that of MM. UTD's solution deviates from that of MM by as much as 2 dB up to 40° and 8 dB beyond 40°, agreement being slightly better for horizontal polarisation. Thus if a limit has to be placed on the method of UTD and GTD (away from its singularities) and equation (10) in the prediction of the RCS of the flat plate it is for a plate of size ∿1λ.

The UTD solution for the rectangular cylinder has been shown to be good down to cylinder width = 1.3λ and length 2.0λ. Comparison of results with MM solutions would reveal the lower limit of validity, independent of data reliability. This comparison is scarcely feasible as can be appreciated by noting that the MM solution for the 1.3λ flat plate took 30 min of CPU time. In view of this no attempt was made to obtain MM solutions for the rectangular cylinder.

6.4 Deficiencies of the theories

6.4.1 Physical Optics

It is a common feature of the PO solutions that they possess deep nulls in RCS which are not realised in the experimental measurements. This effect could have been eliminated from the figures by, for example, convolving the PO solutions with a windowing function. More conveniently, smoothing could have been done by weighting in the transform domain. No such processing has been performed here to emphasise the fact that simple methods such as PO do yield unphysical results.

In general, PO proves to be accurate in the prediction of the main lobes of the RCS patterns, accuracy falls away for aspect angles away from these regions. This arises from the fact that the surface field is taken to be the geometric optics field. A method developed by Ufimtsev(ref.10) known as the physical theory of diffraction corrects for this surface field in PO by including an additional term in the induced surface current - this 'nonuniform' component is due to perturbations created by the departure of the surface from an infinite plane and may arise from the curvature of the surface at a shadow boundary or from geometrical discontinuities such as edges.

The backscattered RCS as predicted by PO is polarisation independent, a result of the tangent plane approximation. This is a fundamental weakness of PO in general though it can yield polarisation dependent results in the case of scatterers with multiple reflections, eg reference 3.

6.4.2 Geometrical theory of diffraction and uniform geometrical theory of diffraction

GTD fails in the transition regions adjacent to shadow and reflection boundaries where the solution becomes infinite and discontinuous. This limitation is overcome by the uniform GTD(UTD) developed by Kouyoumjian and Pathak(ref.8) and by the uniform field introduced by Ahluwalia et al(ref.11,12). Both approaches yield high-frequency fields

that are continuous at shadow and reflection boundaries and that reduce to the fields predicted by GTD away from such transition regions.

The singularities that arise in the GTD solution for the strip and the cylinder appear in the multiple diffraction terms at shadow boundaries. They are a consequence of using Keller's plane wave diffraction coefficients in the treatment of higher order diffraction. When the higher order diffraction terms are formulated in terms of cylindrical wave diffraction, as in UTD, the results are finite.

It is interesting to note that the singly diffracted GTD or UTD field for the strip (equation (16) for vertical polarisation and equation (39) for horizontal polarisation), is finite at $\phi = 0°$ despite the fact that the individual terms are infinite there. The same is observed to hold for the rectangular cylinder (equation (53) for vertical polarisation and equation (59) for horizontal polarisation), at $\phi = 0°$ and $\phi = 90°$. This is a phenomenon that occurs frequently in GTD/UTD analysis of radiation and scattering problems. It was noted by James(ref.6) that the endpoint infinities would cancel to yield a finite result if the aperture had a symmetrical field distribution, though in general this result is not expected to be the same as that obtained by a direct evaluation of the aperture field integral.

A fundamental limitation of GTD and UTD, in common with other ray techniques, is the prediction of infinite fields at caustics. This does not correspond to physical reality and caustic corrections have to be introduced. No general techniques valid for an arbitrary body are available for finding caustic corrections; this involves generating matching functions that provide a smooth transition into a finite value at the caustics(ref.13,14,15). The GTD and UTD edge diffraction concepts are suitable for the analysis of geometries where diffraction appears to come from a single point or group of single isolated points along an edge. At $\phi = 0°$ for the flat plate, and $\phi = 0°$ and 90° for the finite rectangular cylinder, there is a congruence of backscattered rays, that is, caustics occur. Thus GTD and UTD fail to predict the field in the backscattered directions. In these cases it is convenient to use the physical optics approximation to correct the scattered field determined by GTD and UTD; this caustic correction technique is useful for the flat plate structures treated here. Another technique for caustic correction is to employ equivalent electric and magnetic edge currents derived from the GTD/UTD diffracted field away from the caustics. These equivalent currents are substituted in the radiation integral to give the caustic field.

In this paper the flat plate and finite rectangular cylinder have not been treated as three dimensional scattering targets; rather the results were obtained by using a normalisation scheme (equation (10)) to reduce the two dimensional infinite strip and infinite cylinder solutions to ones applicable to the finite problems. Interestingly, the solutions thus obtained in the backscattered directions corresponding to caustics for the finite target problem, yield finite values that agree with PO even though the geometrical optics reflection terms were not included. This effect has been observed by James(ref.6) in his treatment of radiation from a parallel-plate waveguide as has the cancellation of the singularities in the singly diffracted field terms mentioned earlier.

7. CONCLUSIONS

PO proves to be very accurate in the neighbourhood of specular reflections, that is, in the region of the main lobes of the RCS curves, at least down to plate sizes $2a \sim 1.3\lambda$. Its performance deteriorates with aspect angle away from the specular direction where polarisation dependent effects become evident but are not predicted by PO, though the range of reliable prediction increases with plate size. It should be noted, however, that apart from a substantial overestimation of the depths of the nulls, PO's domain of applicability is extended to the next sidelobes along with increasing $\frac{2a}{\lambda}$.

Singularities exist in the GTD solution for both polarisations at grazing incidence on the flat plate. Away from the neighbourhood of these singularities, the GTD solution for the flat plate agrees with the UTD solution. GTD and UTD results for the flat plate improve as $\frac{2a}{\lambda}$ increases. The AC data at the smaller values of $\frac{2a}{\lambda}$ are erratic but comparison with MM solutions has demonstrated the accuracy of UTD solution down to plate dimensions of one wavelength.

An ideal thin flat plate should yield a zero RCS at grazing incidence for horizontal (that is, transverse) polarisation in the limit of zero thickness, yet the measured RCS for horizontal polarisation does not diminish to zero at grazing incidence as expected. This suggests that the plate is not a "thin" plate as assumed or that an unexpectedly significant contribution comes from vertex diffraction. The thickness of the edge ranges from 0.01λ at 4 GHz to 0.04λ at 12 GHz. No exact solution is available for diffraction from an edge with finite thickness, however references 16 and 17 present solutions for a thick edge modelled as two 90° wedges. The application of this model to the present case has not been attempted.

The GTD solution for the rectangular cylinder for horizontal polarisation has singularities at $\phi = 0$ and 90°. Away from the neighbourhood of these singularities close agreement is obtained between GTD and UTD solutions. The results for the rectangular cylinder at 4 GHz work well down to $\frac{2a}{\lambda} = 1.3$ for the 30 cm and 50 cm cylinders where termination errors are not significant. Agreement of the UTD solution with measured results is definitely not good for the 10 cm cylinder, particularly at the lower frequencies of 4 and 6 GHz; data reliability is questionable in these cases and in the absence of comparison with accurate numerical solutions of the exact integral equations for scattering from the cylinder, it is difficult to assess the performance of the method for these cases. It could well be that termination errors arising from the assumptions implicit in equation (10) are more significant for the cylinder of length 1.3λ than for the flat plate of length 1.3λ. It seems more likely, however, that the poor agreement for the 10 cm cylinder is due to errors in the anechoic chamber measurements, as in the case of the flat plate, and that UTD with equation (10) is a good description of scattering from a finite cylinder down to cylinder lengths of the order of a wavelength.

8. ACKNOWLEDGEMENT

The anechoic chamber measurements incorporated in this paper were obtained by Mr J. Crombie under the direction of Mr A. Tickner of Radar Division. Thanks are due Dr J.L. Whitrow for his perceptive comments on an early draft of this paper.

REFERENCES

No.	Author	Title
1	Ruck, G.T., Barrick, D.E., Stuart, W.D. and Krichbaum, C.K.	"Radar Cross Section Handbook Vol 1". Plenum Press, New York, 1970
2	Crispin, Jr., J.W. and Siegel, K.M.	"Methods of Radar Cross Section Analysis". Academic Press, New York, 1968
3	Anderson, W.C.	"Polarisation - Dependent Scattering Properties of Trihedral Corner Reflectors". To be published
4	Ross, R.A.	"Radar Cross Section of Rectangular Flat Plates as a Function of Aspect Angle". IEEE Trans. Antennas Propagat, Vol. AP-14, pp. 329-335, 1966
5	Rhodes, D.R.	"An Investigation of Pulsed Radar Systems for Model Measurements". Ohio State Ant Lab., Columbus, Rept 475-6, p. 94, 1964
6	James, G.L.	"Geometrical Theory of Diffraction for Electromagnetic Waves".
7	Rudduck, R.C.	"Application of Wedge Diffraction and Wave Interaction Methods to Antenna Theory". OSU short course notes for GTD and Numerical Techniques, Vol. 1, September 1975
8	Kouyoumjian, R.G. and Pathak, P.H.	"A Uniform Geometrical Theory of Diffraction for an Edge in a Perfectly Conducting Surface". Proc. IEEE, Vol. 62, pp. 1448-1461, November 1974
9	Tickner, A.T. and Sinnott, D.H.	"The Electronics Research Laboratory Anechoic Chamber and its Evaluation". Seminar on Electromagnetic Antenna and Scattering Measurements, Part II, CSIRO Division of Applied Physics, National Measurement Laboratory, November 1982
10	Ufimtsev, P. Ya.	"Method of Edge Waves in Physical Theory of Diffraction". Sovyetskoye Radio, Moscow, 1962 Translated and available from the US Air Force Foreign Technology Division, Wright-Patterson, AFB, Ohio, USA

11	Ahluwalia, D.S., Lewis, R.M. and Boersma, J.	"Uniform Asymptotic Theory of Diffraction by a Plane Screen". SIAMJ. Appl.Math. Vol. 16, pp. 783-807, 1968
12	Lewis, R.M. and Boersma, J.	"Uniform Asymptotic Theory of Edge Diffraction Theory". J. Math. Phys., Vol. 10, pp. 2291-2305, 1969
13	Keller, J.B.	"Diffraction by an Aperture". J.Appl.Phys., Vol. 28, pp. 426-444, 1959
14	Ryan, Jr., C.E. and Peters, Jr., L.	"Evaluation of Edge-Diffracted Fields including Equivalent Currents for the Caustic Regions". IEEE Trans Antennas Propagat., Vol. AP-17, pp. 292-299, 1969
15	Albertson, N.C., Balling, P. and Jensen, N.E.	"Caustics and Caustic Corrections to the Field Diffracted by a Curved Edge". IEEE Trans. Antennas Propagat., Vol. AP-25, pp. 297-303, 1977
16	Burke, J.E. and Keller, J.B.	"Diffraction by a Thick Screen, a Step and Related Axially Symmetric Objects". Contract A 36-039-SC-78281, Sylvania Electronic Systems, Mountain View, Calif., March 1960
17	Russo, P.M., Kudduck, R.C. and Peters, Jr., L.	"A Method for Computing E-Plane Patterns of Horn Antennas". IEEE Trans Antennas Propagat., Vol. AP-13, pp. 219-224, March 1965

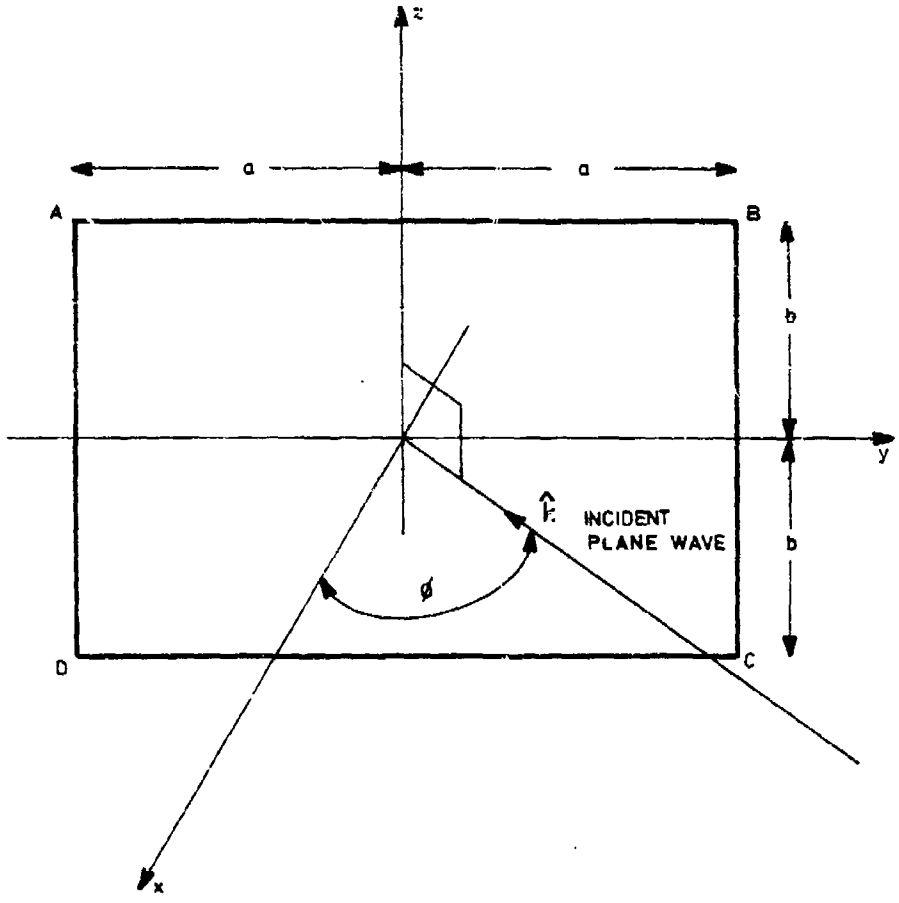

Figure 1. Flat plate

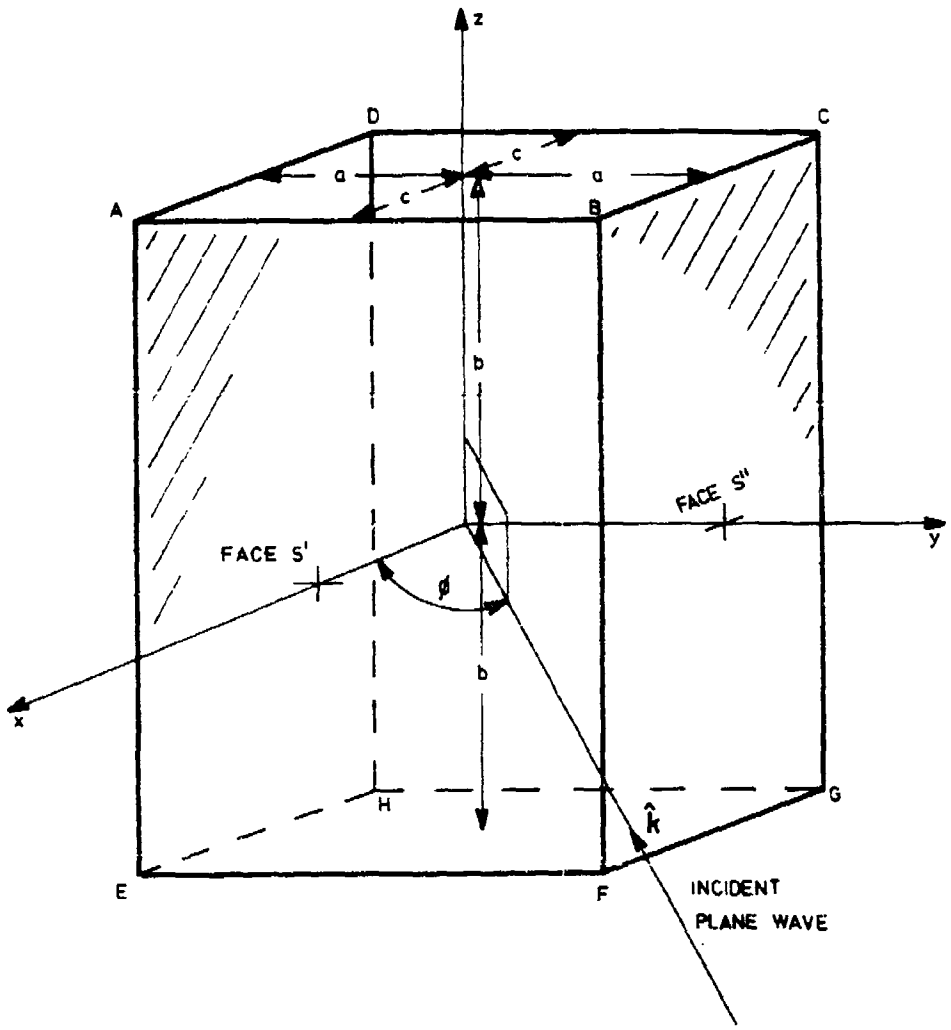

Figure 2. Rectangular cylinder

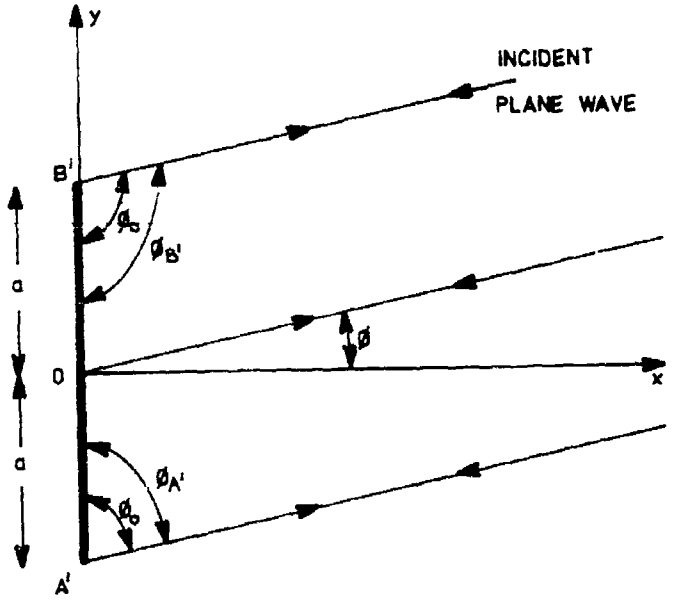

Figure 3. Top view of flat plate in azimuthal plane

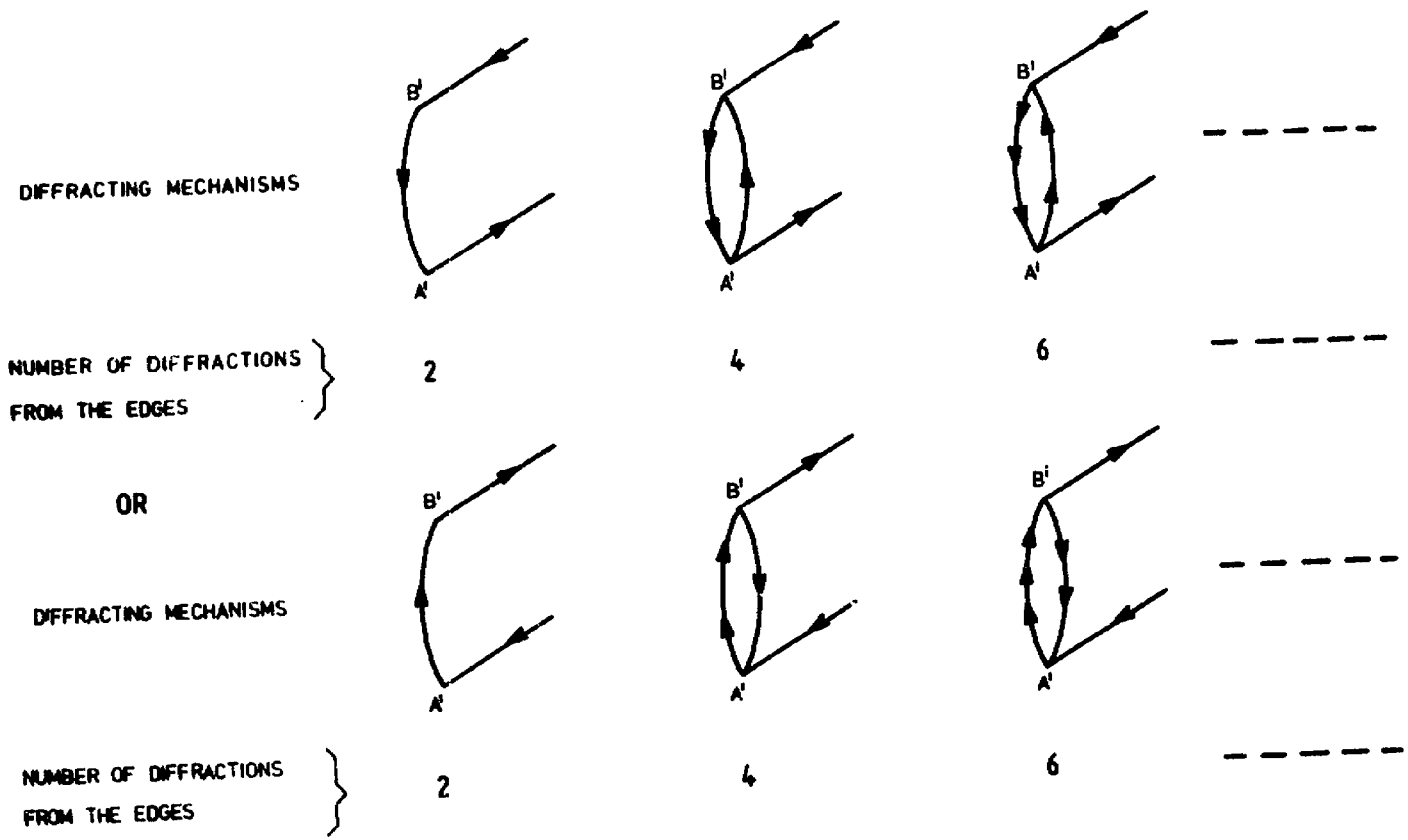

Figure 4. Case (a) Multiple diffraction processes

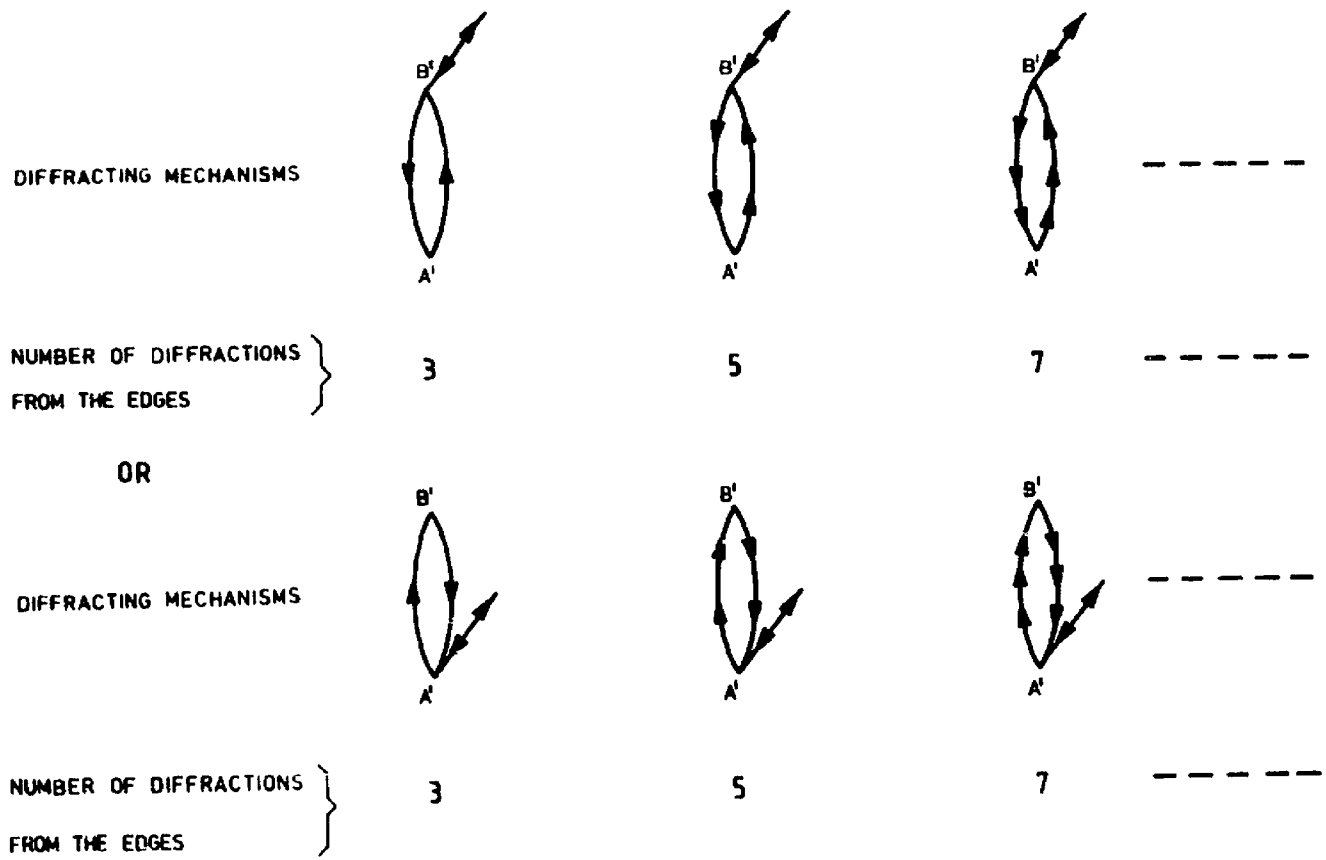

Figure 5. Case (b) Multiple diffraction processes

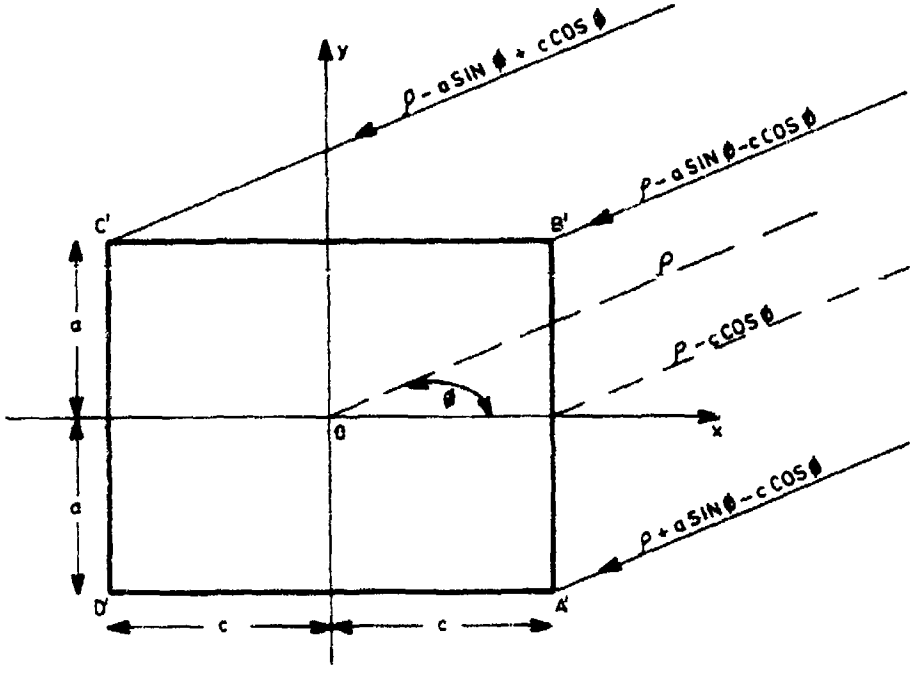

Figure 6. Top view of rectangular cylinder in azimuthal plane

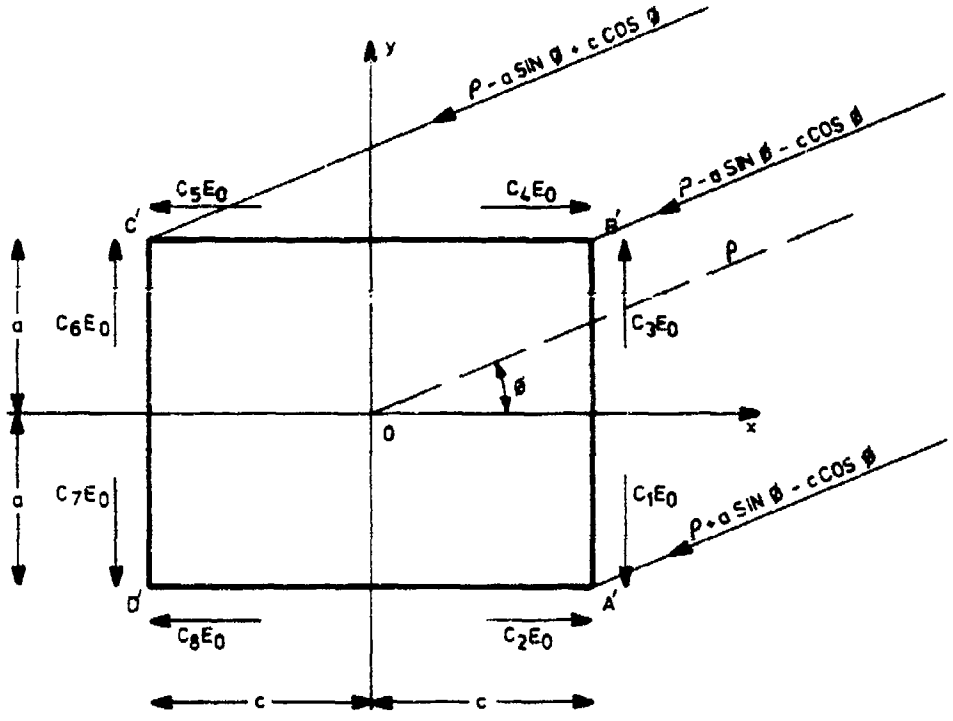

Figure 7. Self-consistent representation of surface waves on the rectangular cylinder

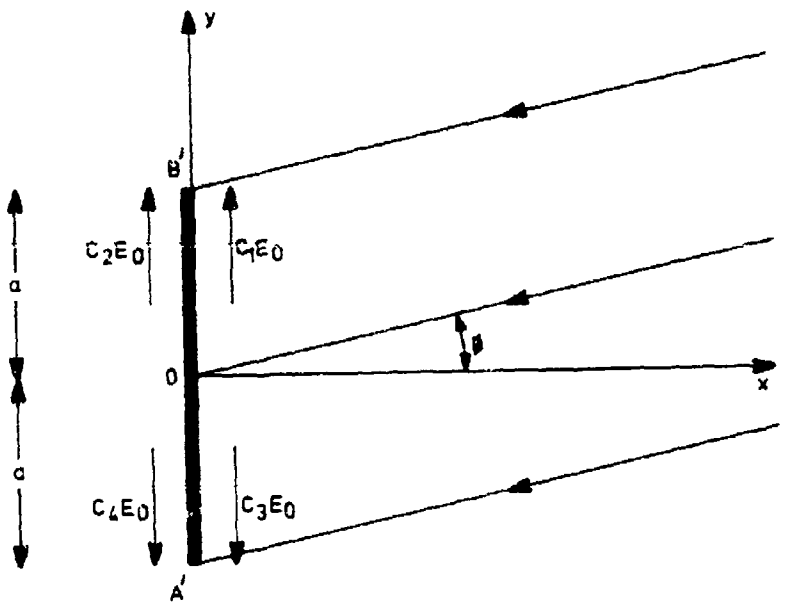

Figure 8. Self-consistent representation of surface waves on the strip

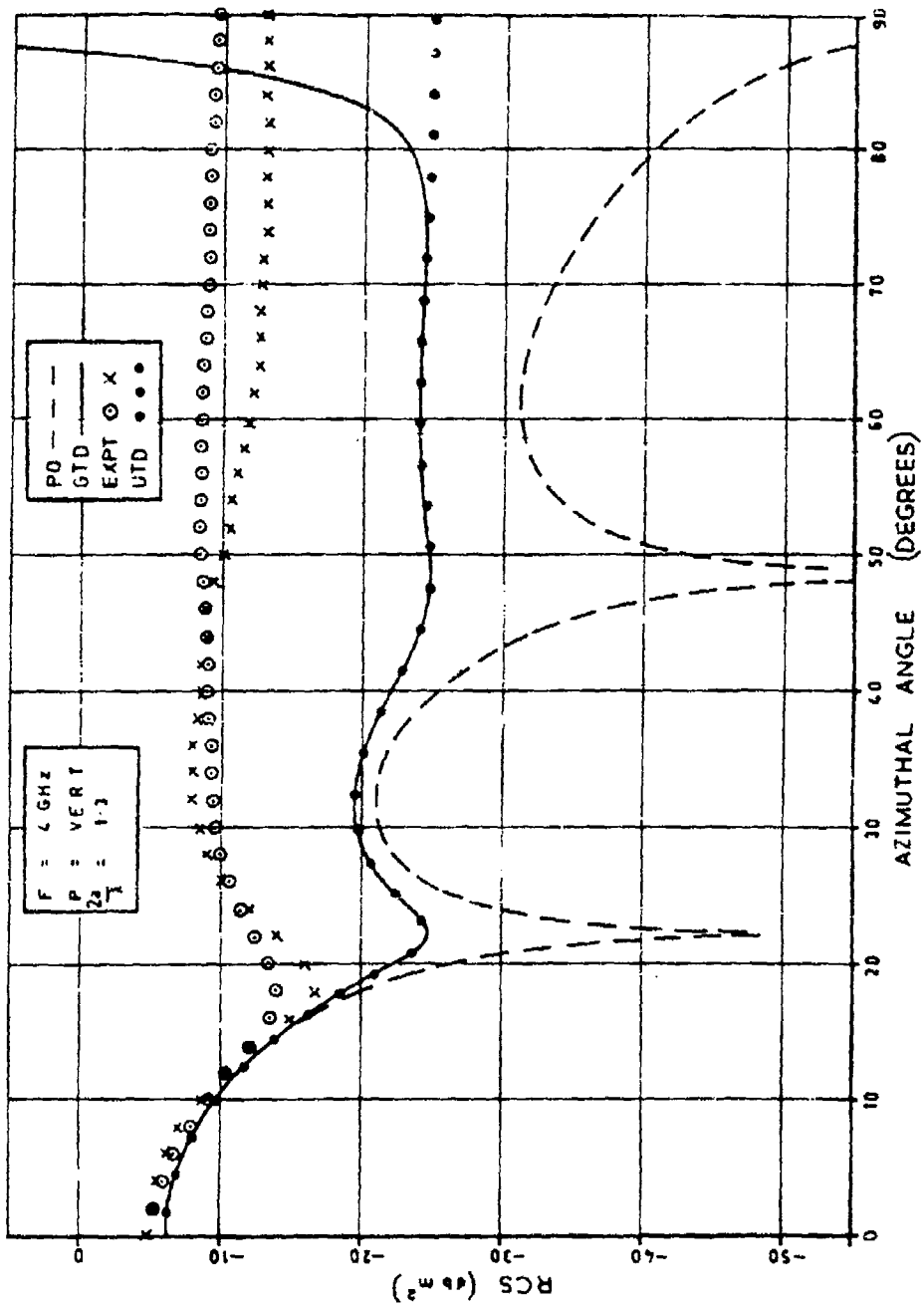

Figure 9. RCS for flat plate at 4 GHz (vertical polarisation)

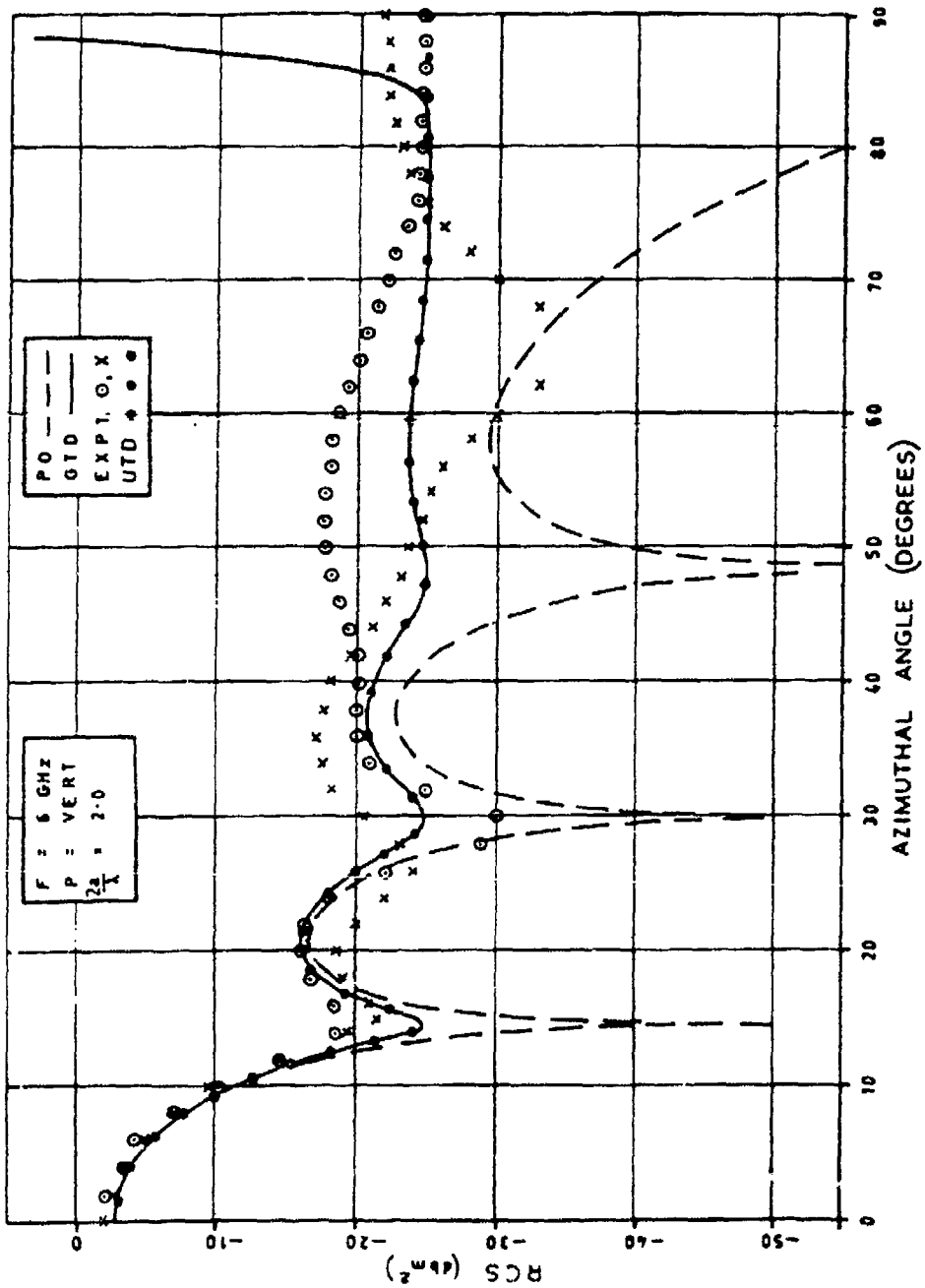

Figure 10. RCS for flat plate at 6 GHz (vertical polarisation)

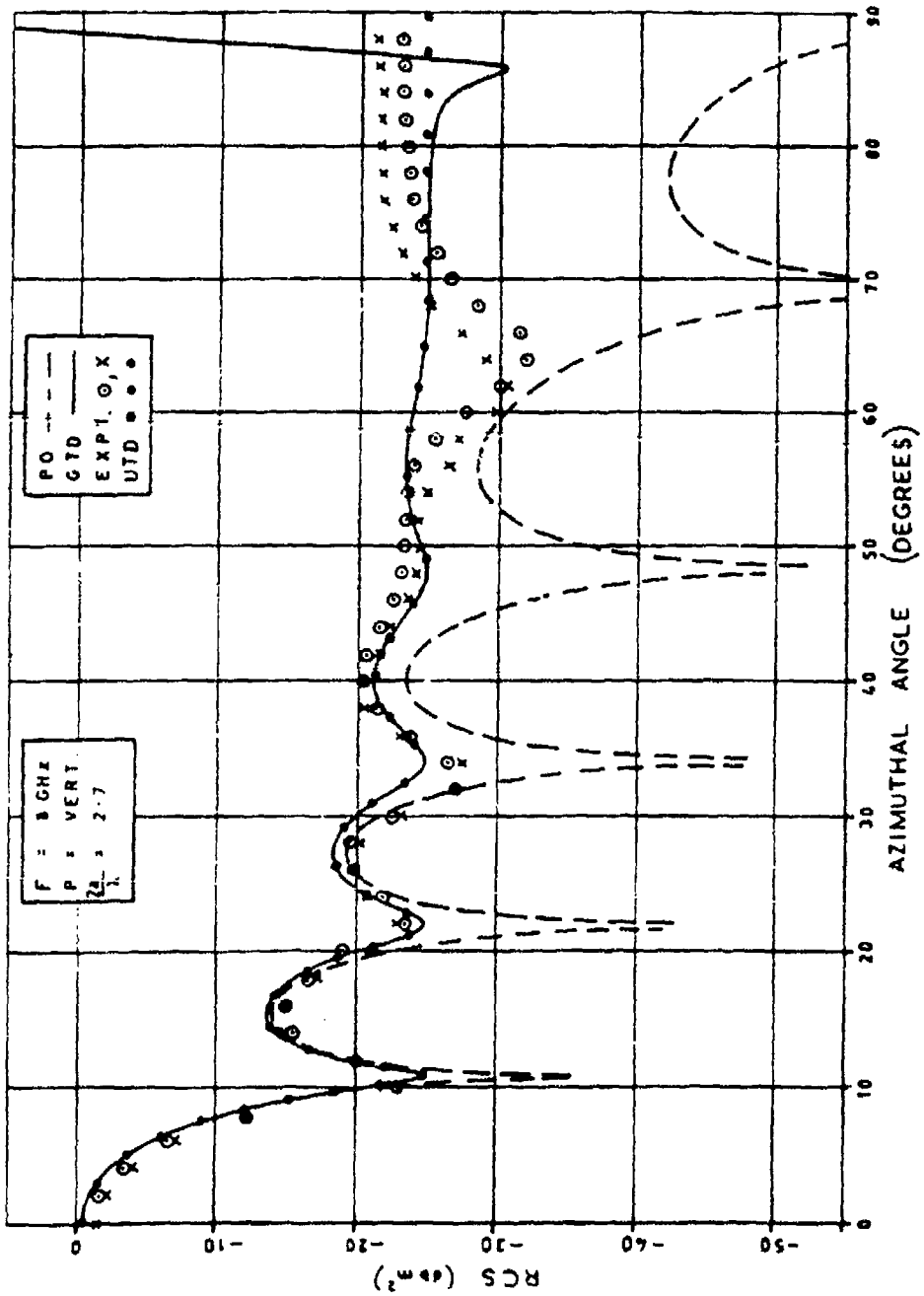

Figure 11. RCS for flat plate at 8 GHz (vertical polarisation)

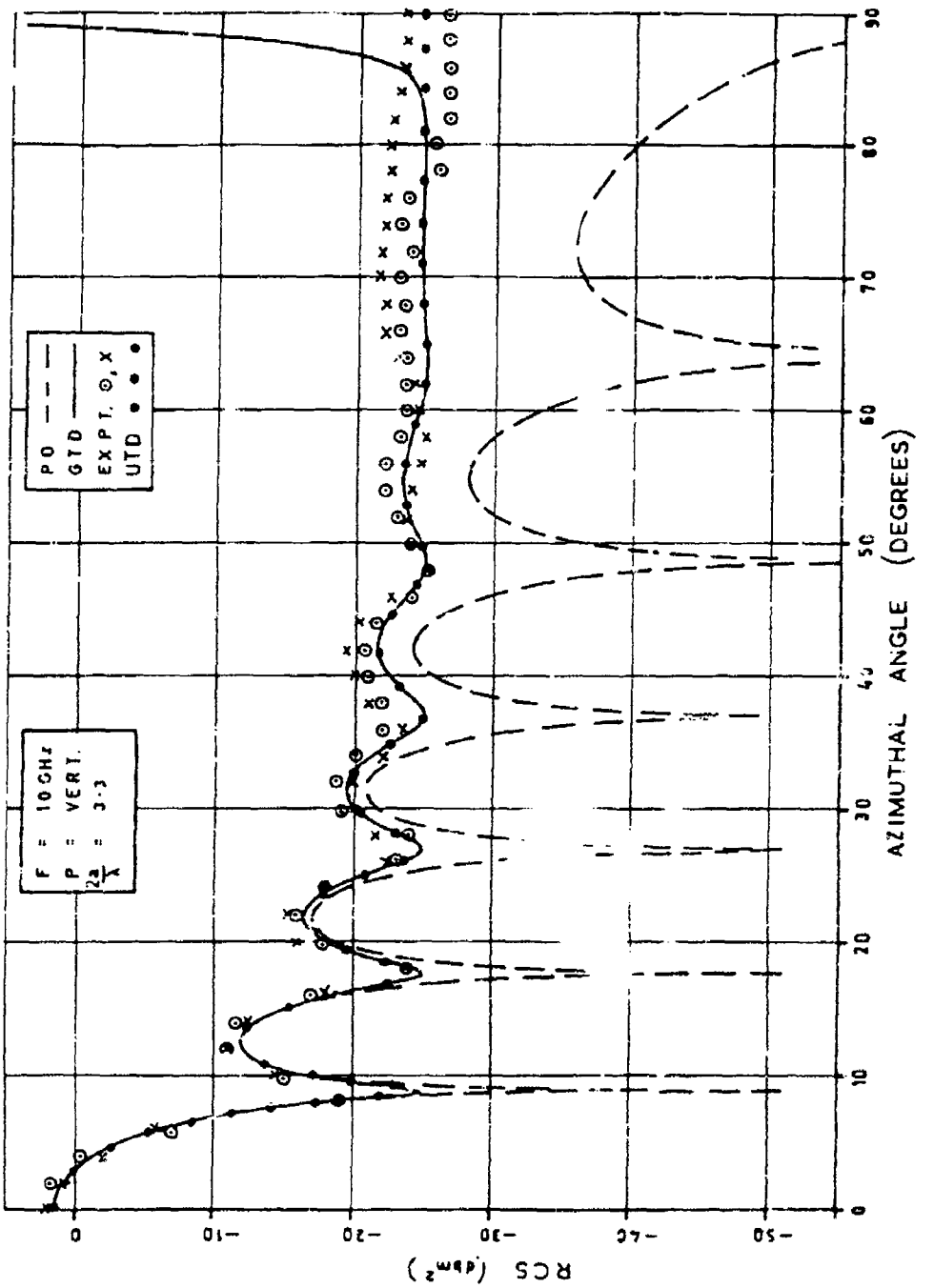

Figure 12. RCS for flat plate at 10 GHz (vertical polarisation)

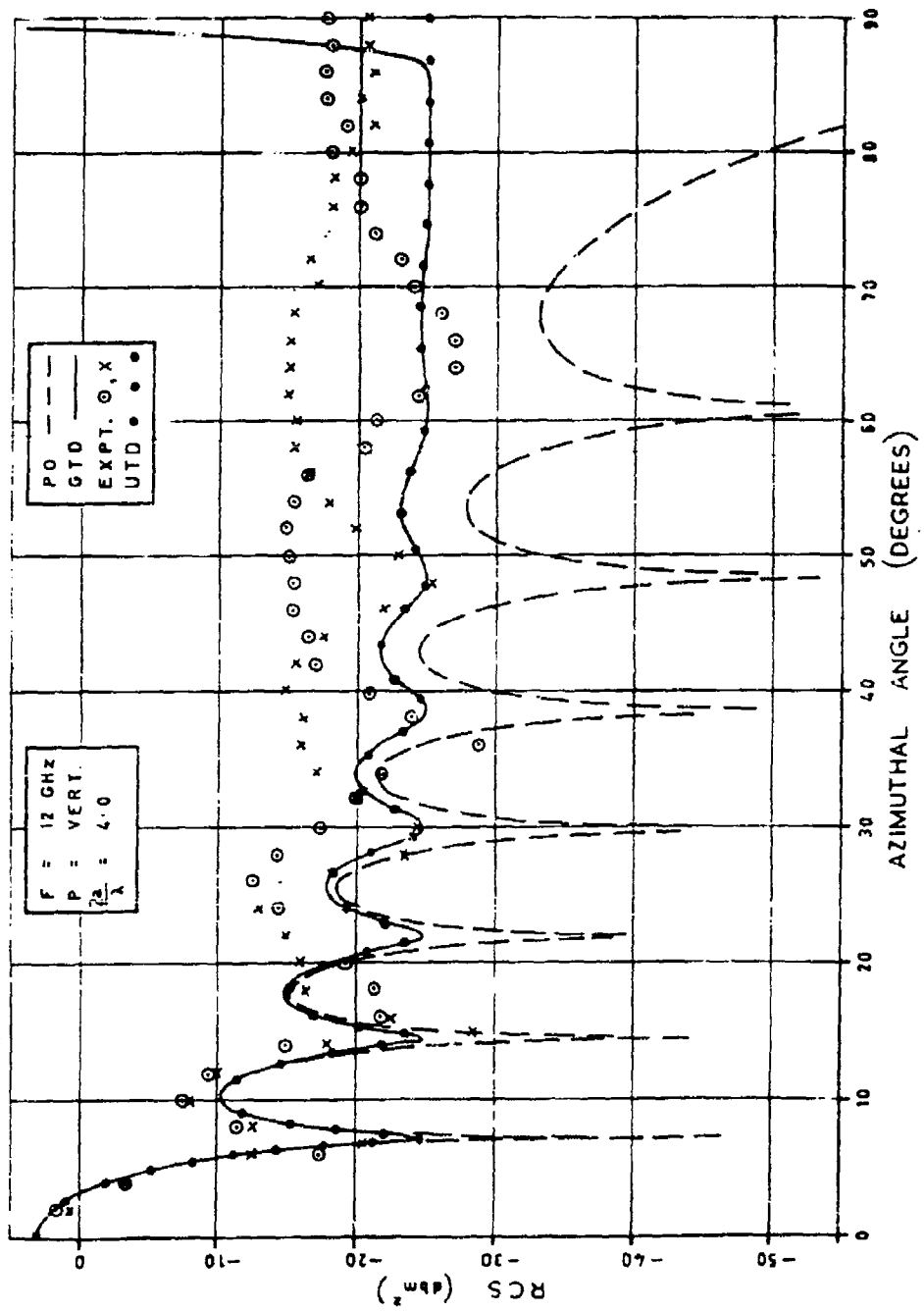

Figure 13. RCS for flat plate at 12 GHz (vertical polarisation)

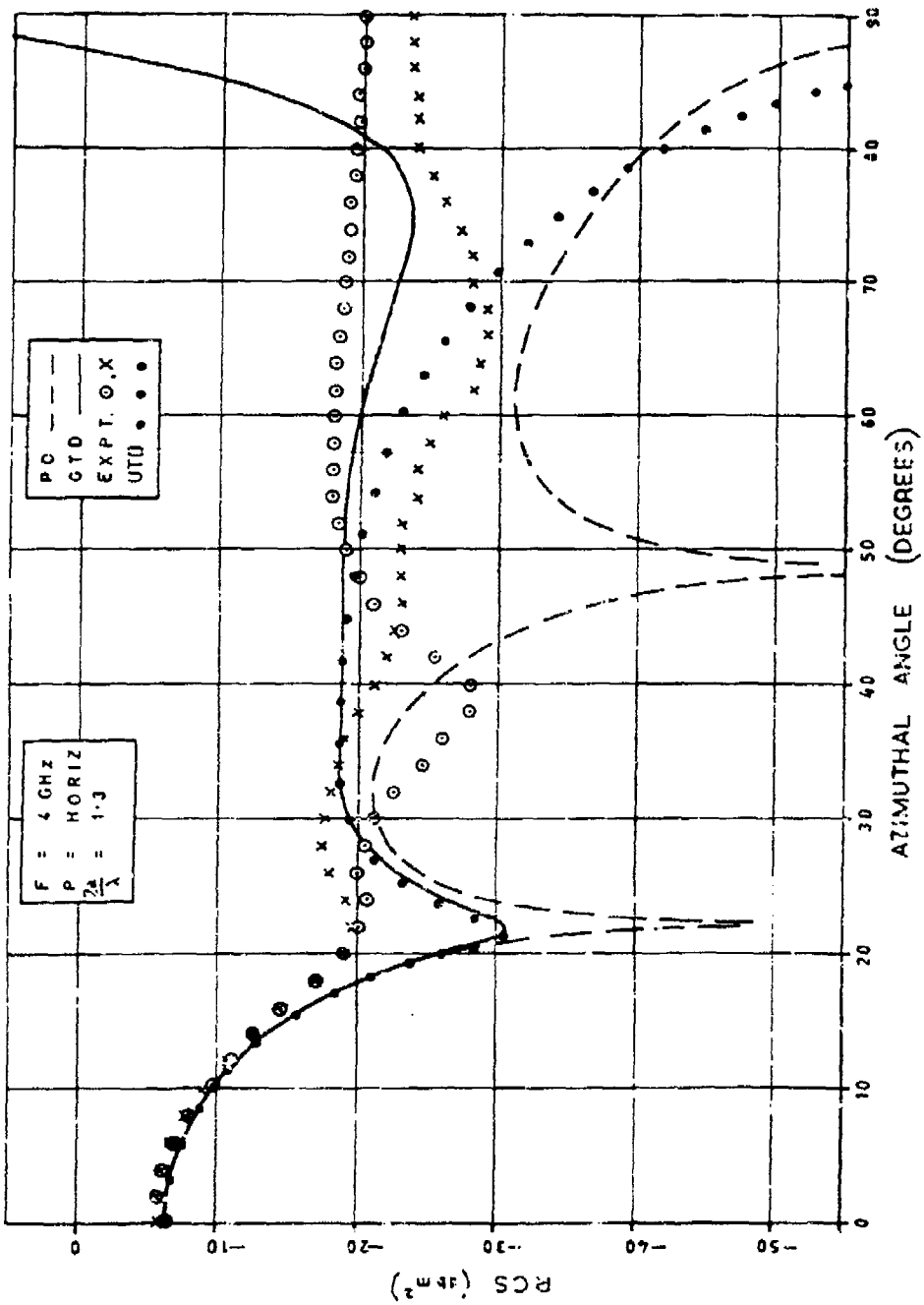

Figure 14. RCS for flat plate at 4 GHz (horizontal polarisation)

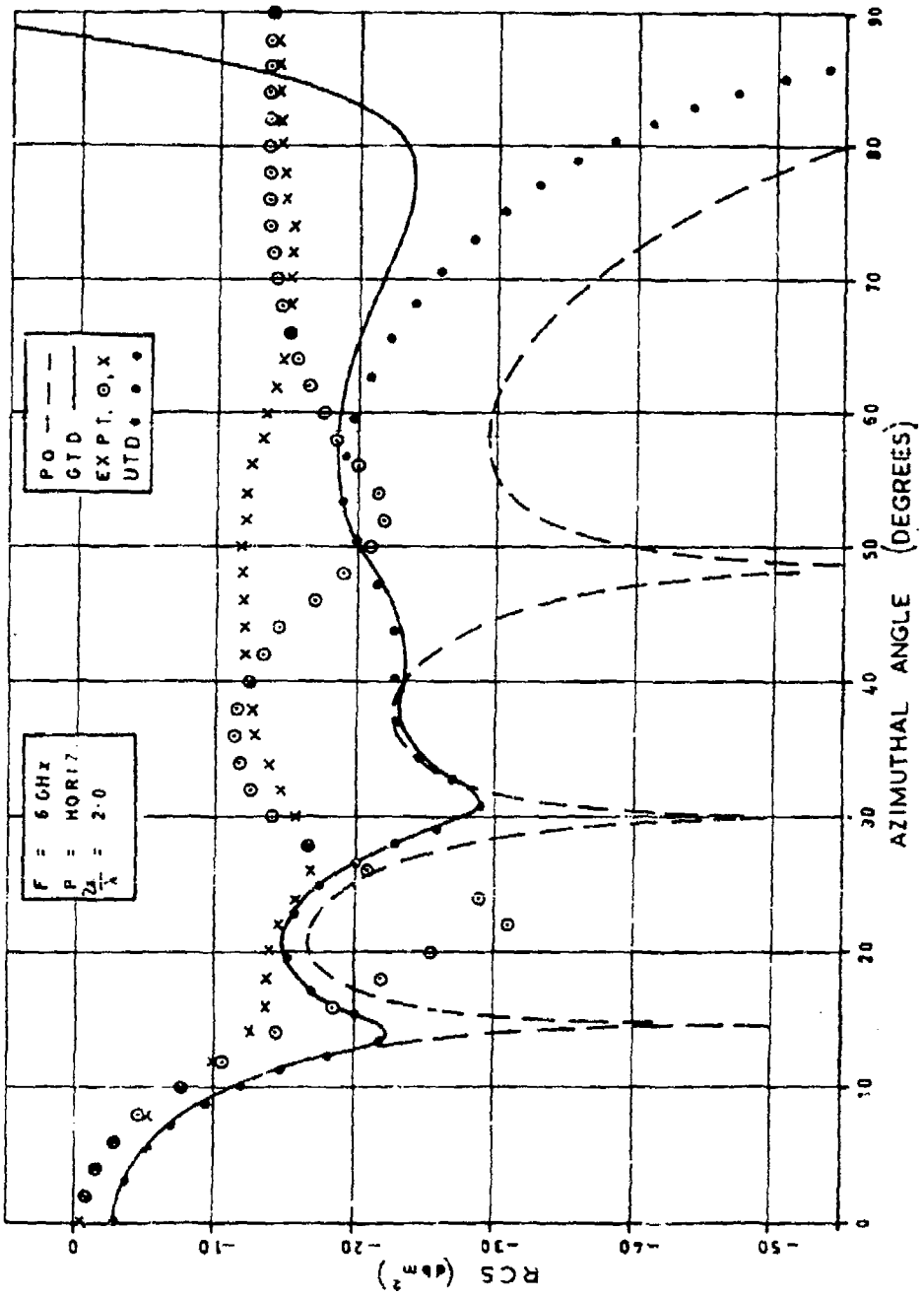

Figure 15. RCS for flat plate at 6 GHz (horizontal polarisation)

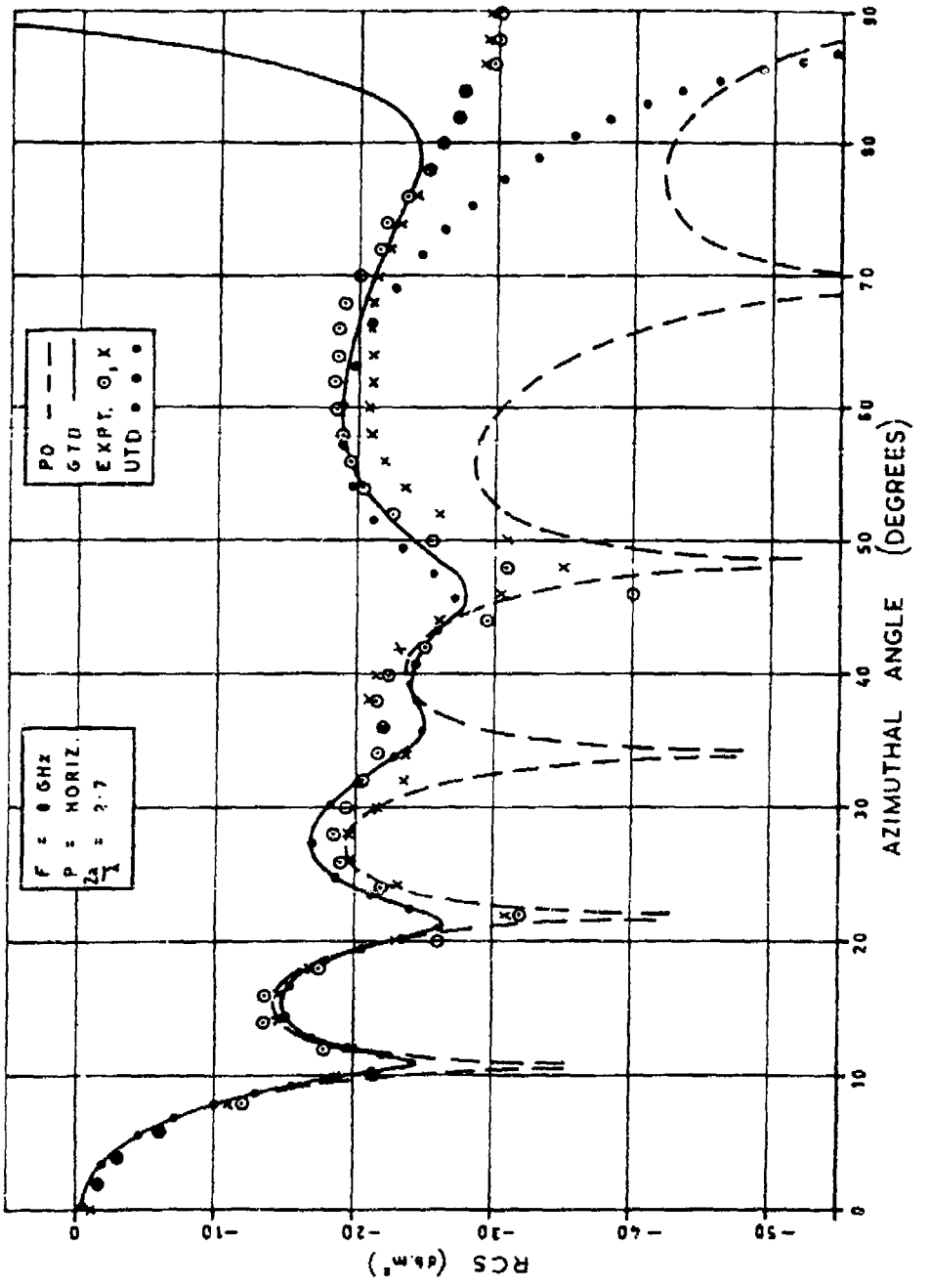

Figure 16. RCS for flat plate at 8 GHz (horizontal polarisation)

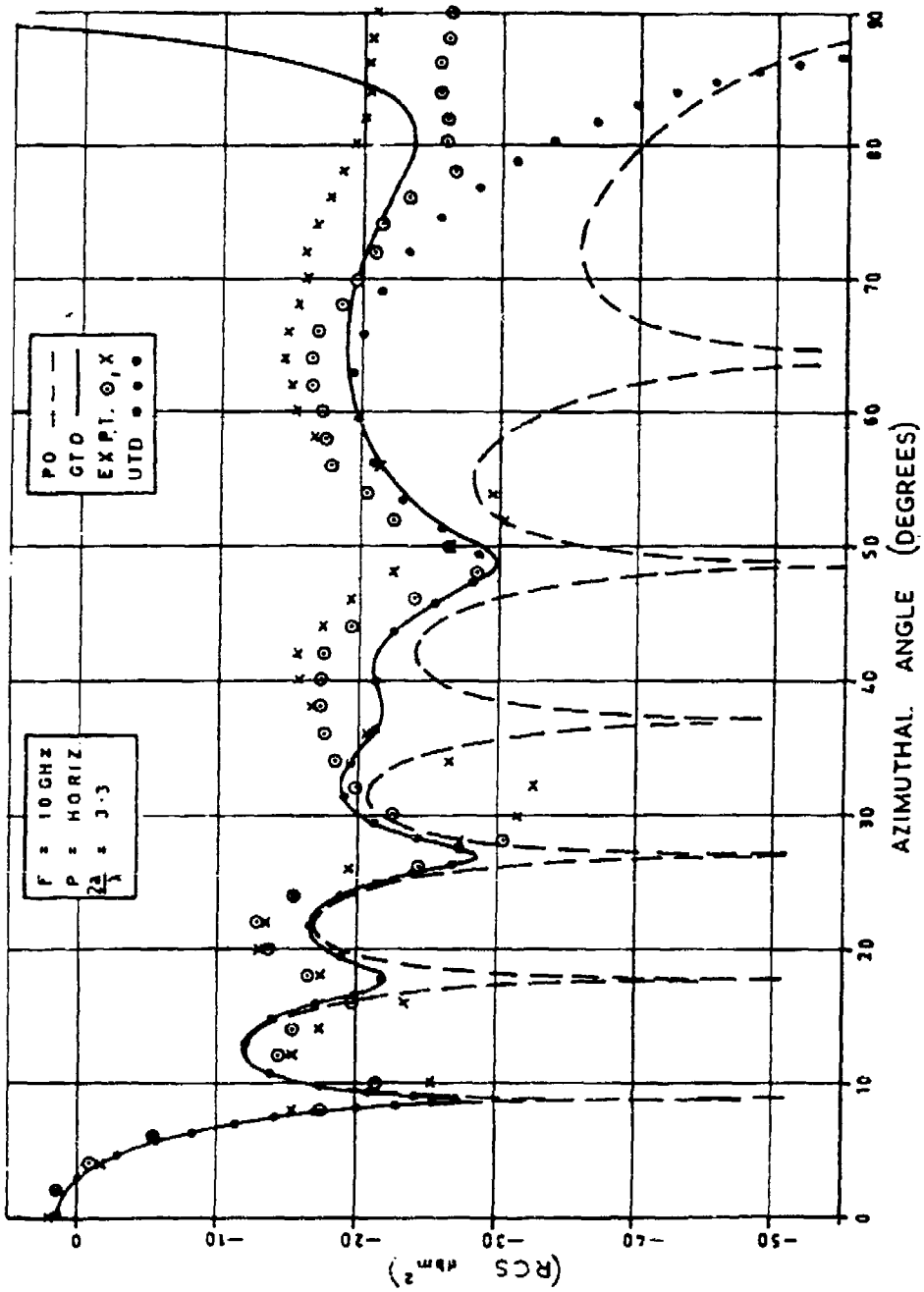

Figure 17. RCS for flat plate at 10 GHz (horizontal polarisation)

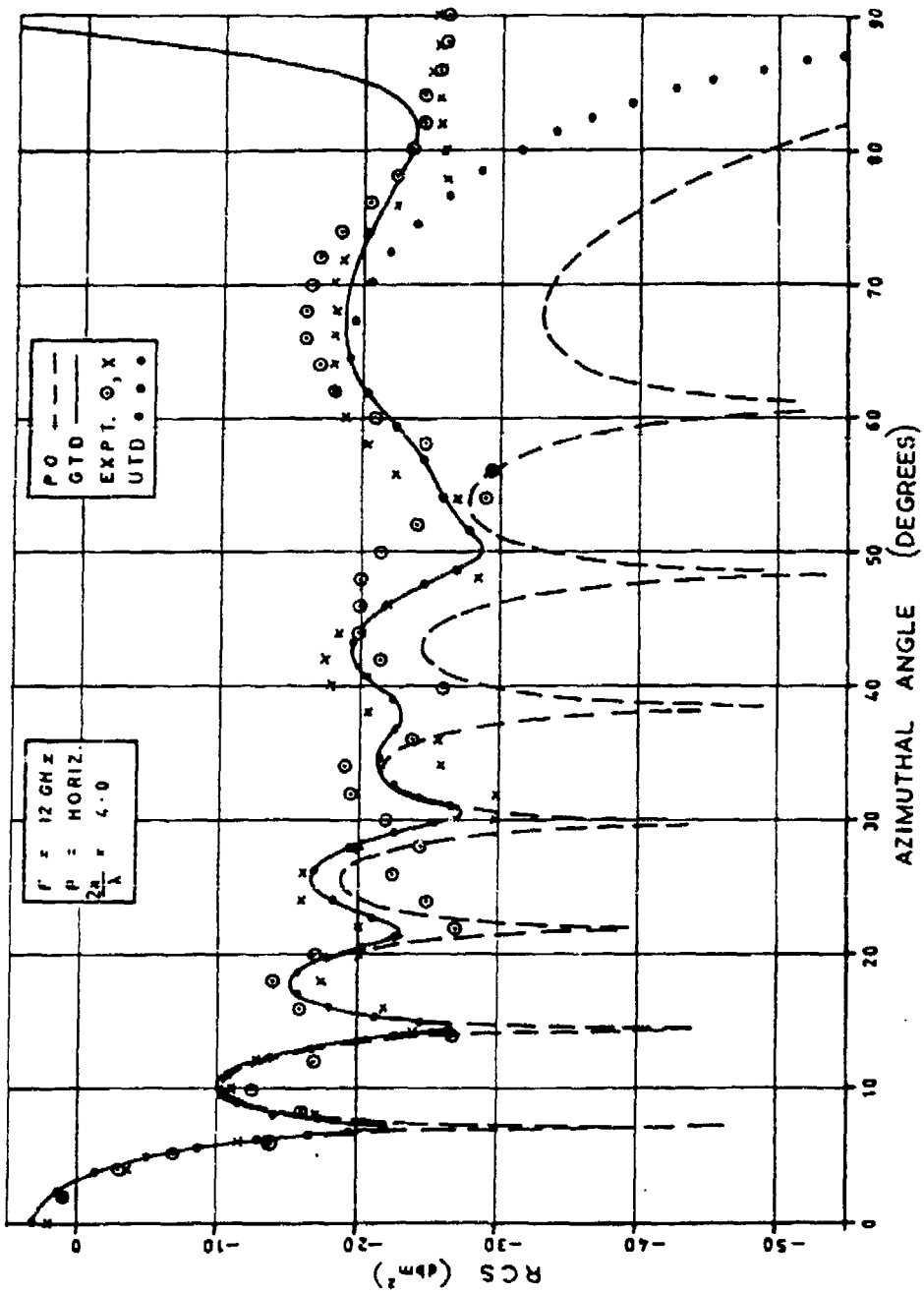

Figure 18. RCS for flat plate at 12 GHz (horizontal polarisation)

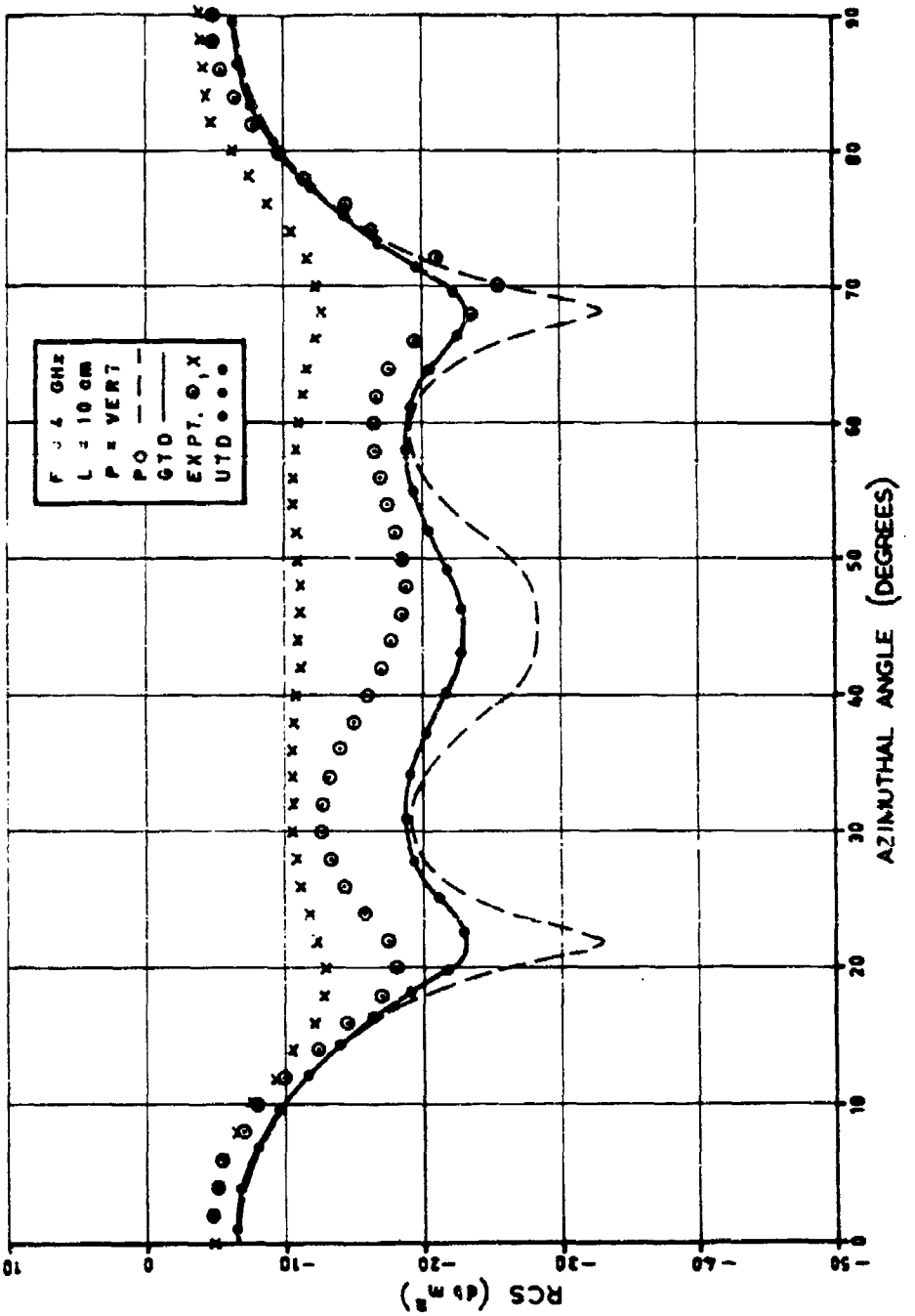

Figure 19. RCS for 10 cm cylinder at 4 GHz (vertical polarisation)

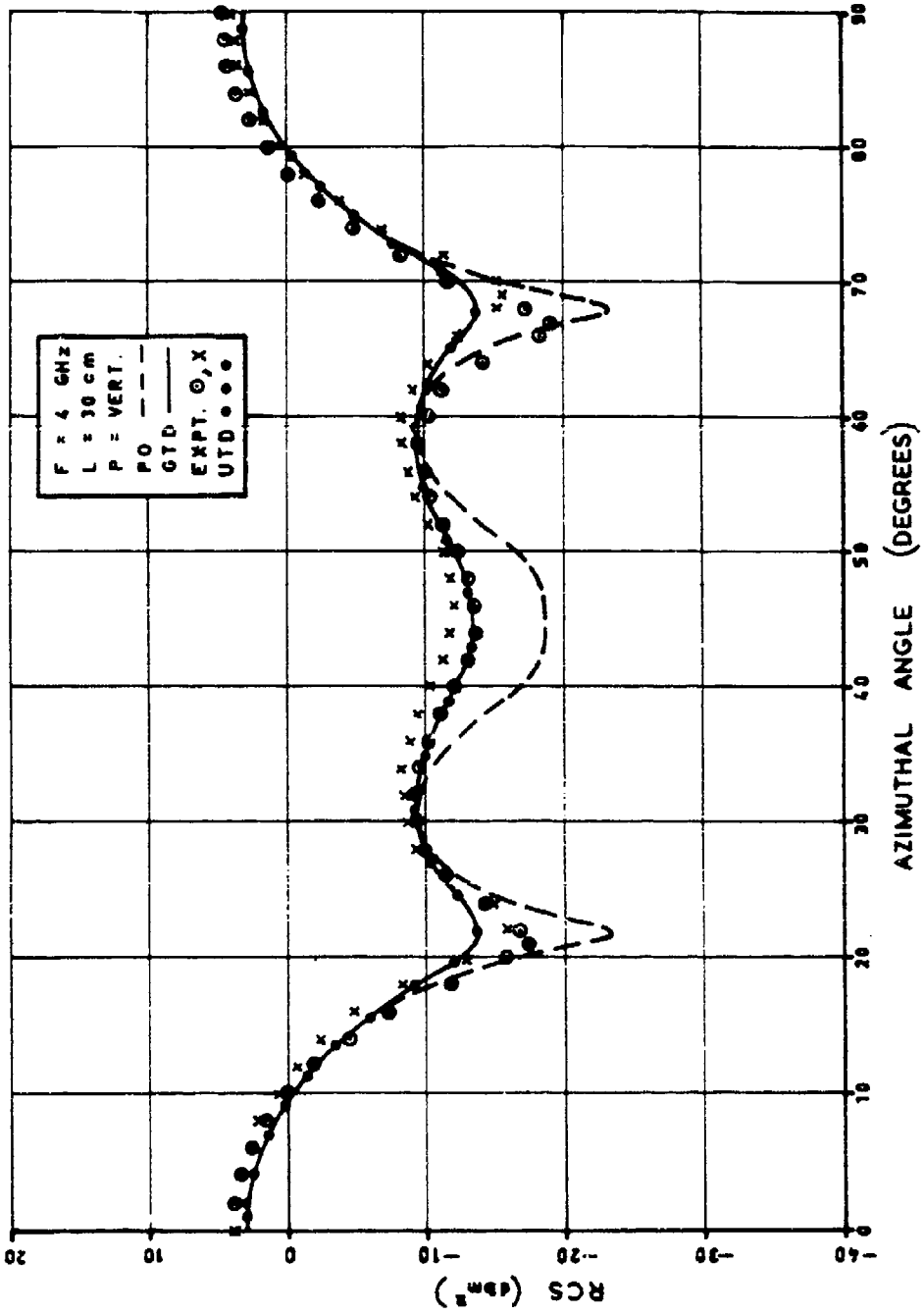

Figure 20. RCS for 30 cm cylinder at 4 GHz (vertical polarisation)

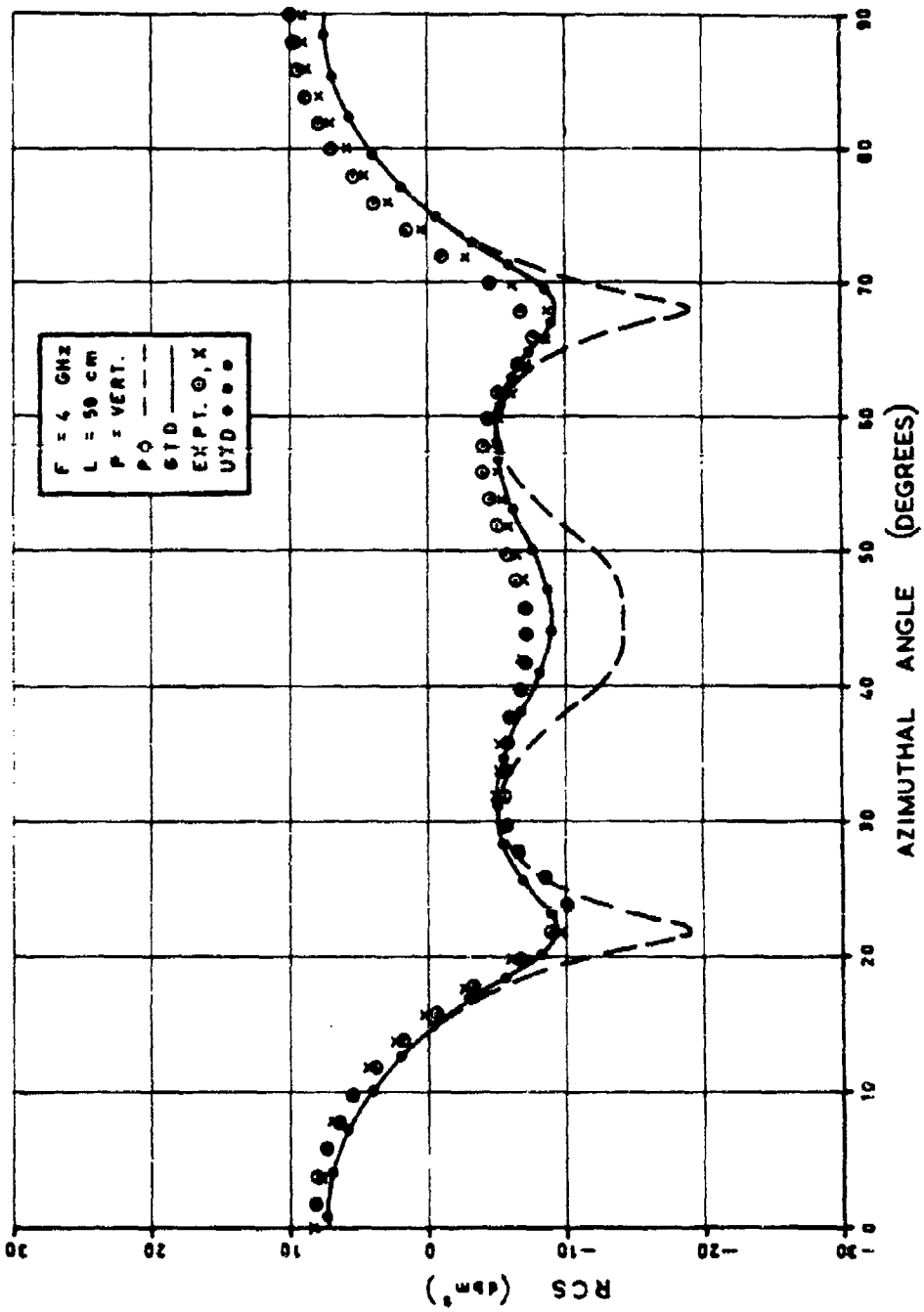

Figure 21. RCS for 50 cm cylinder at 4 GHz (vertical polarisation)

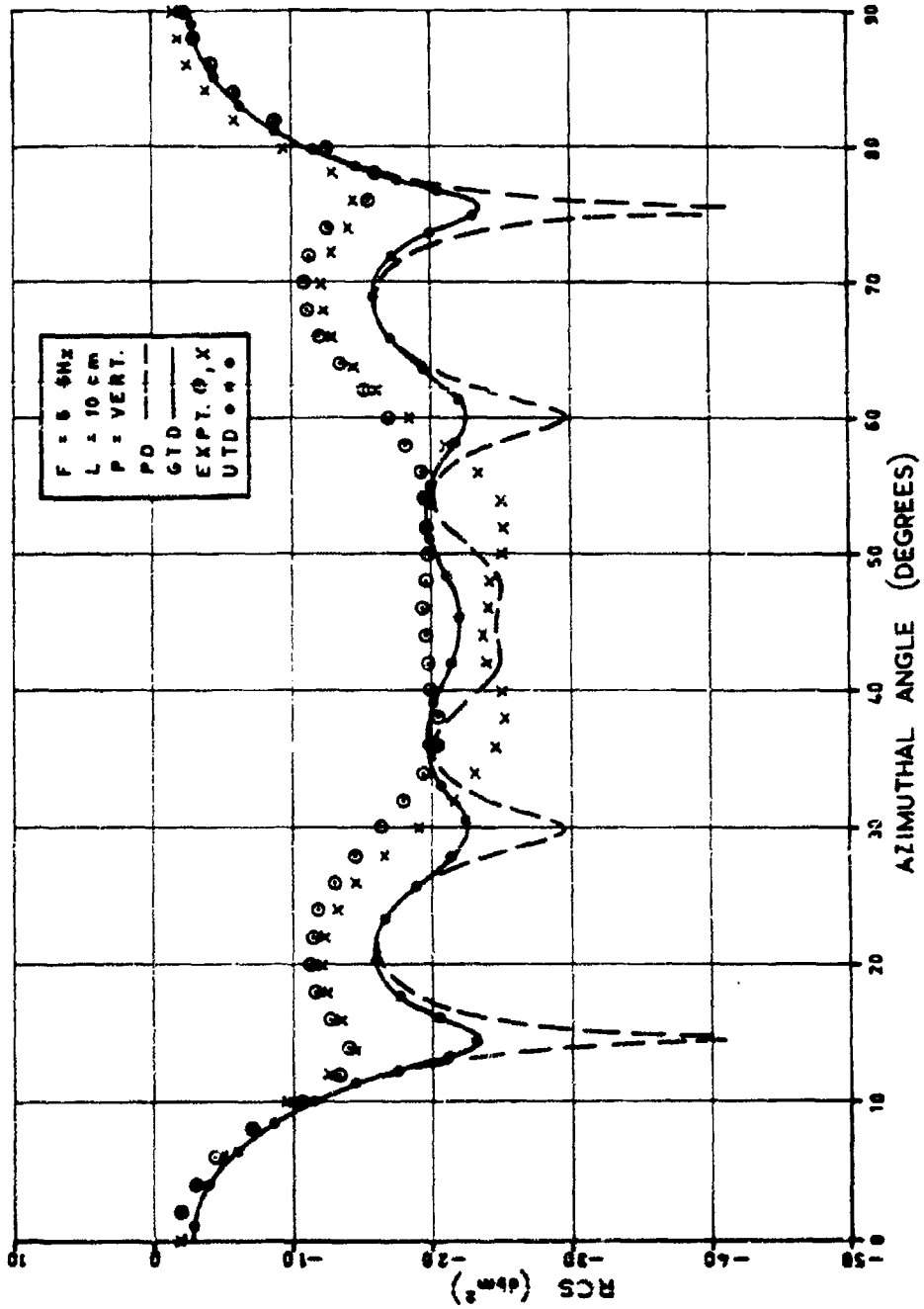

Figure 22. RCS for 10 cm cylinder at 6 GHz (vertical polarisation)

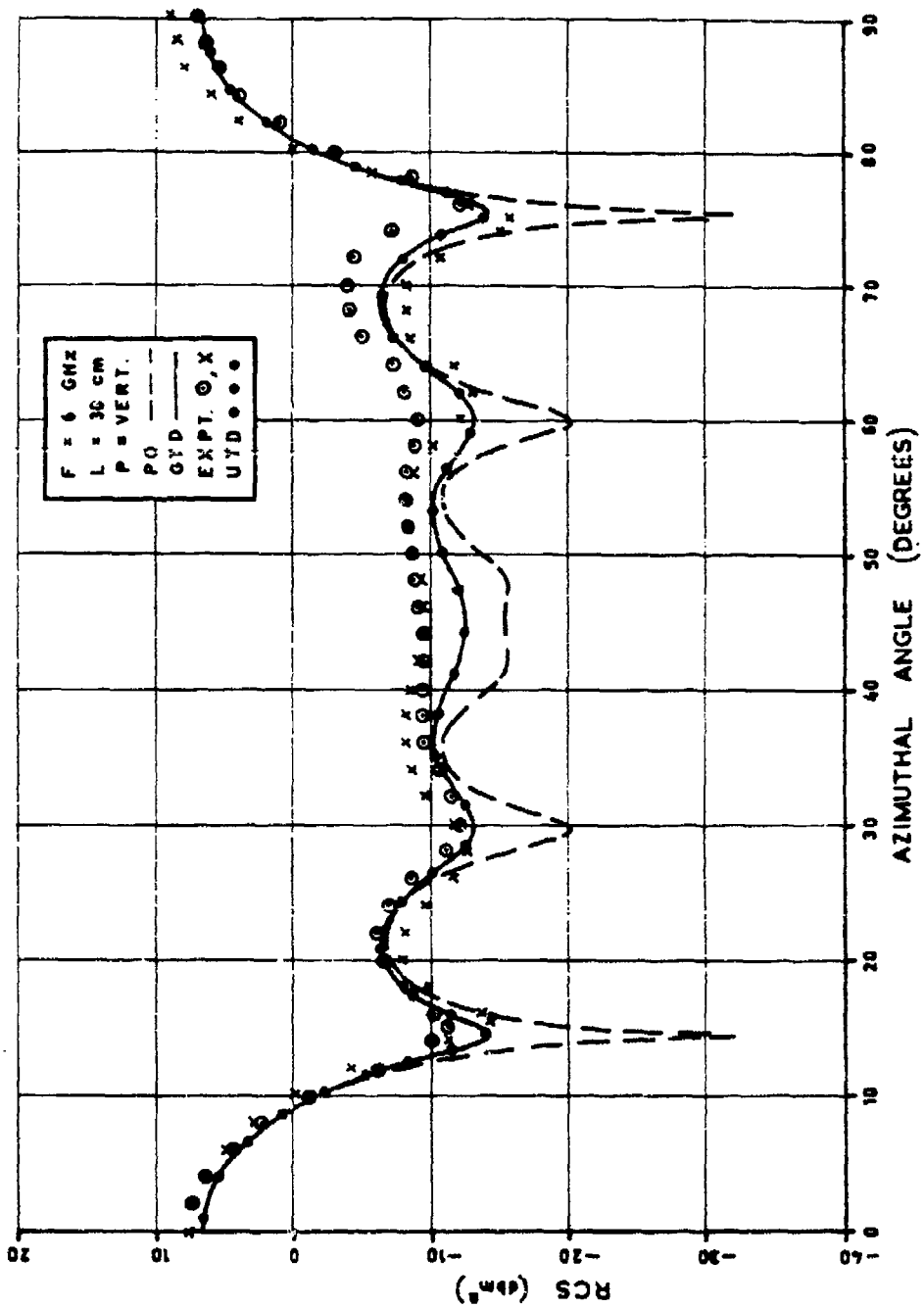

Figure 23. RCS for 30 cm cylinder at 6 GHz (vertical polarisation)

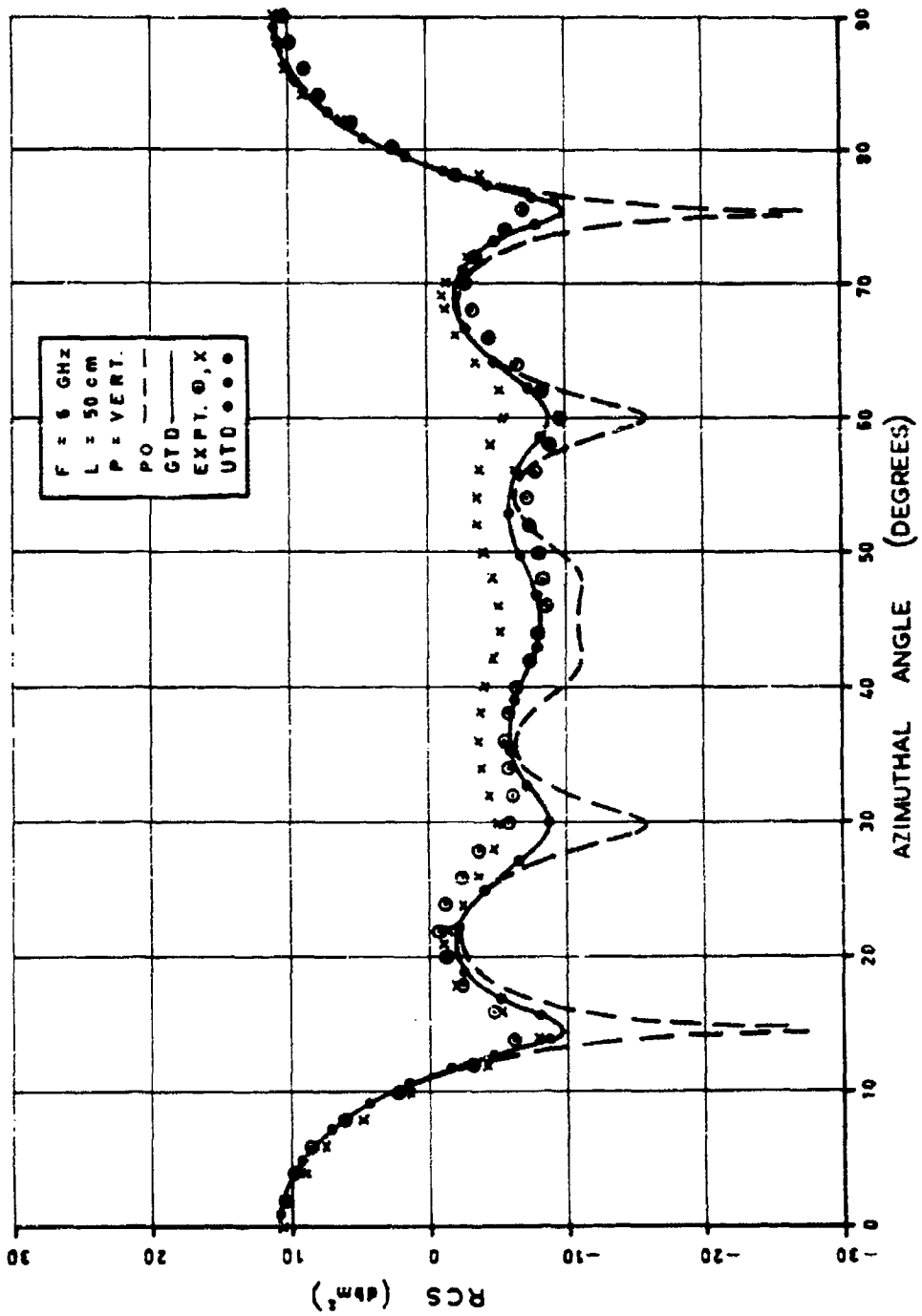

Figure 24. RCS for 50 cm cylinder at 6 GHz (vertical polarisation)

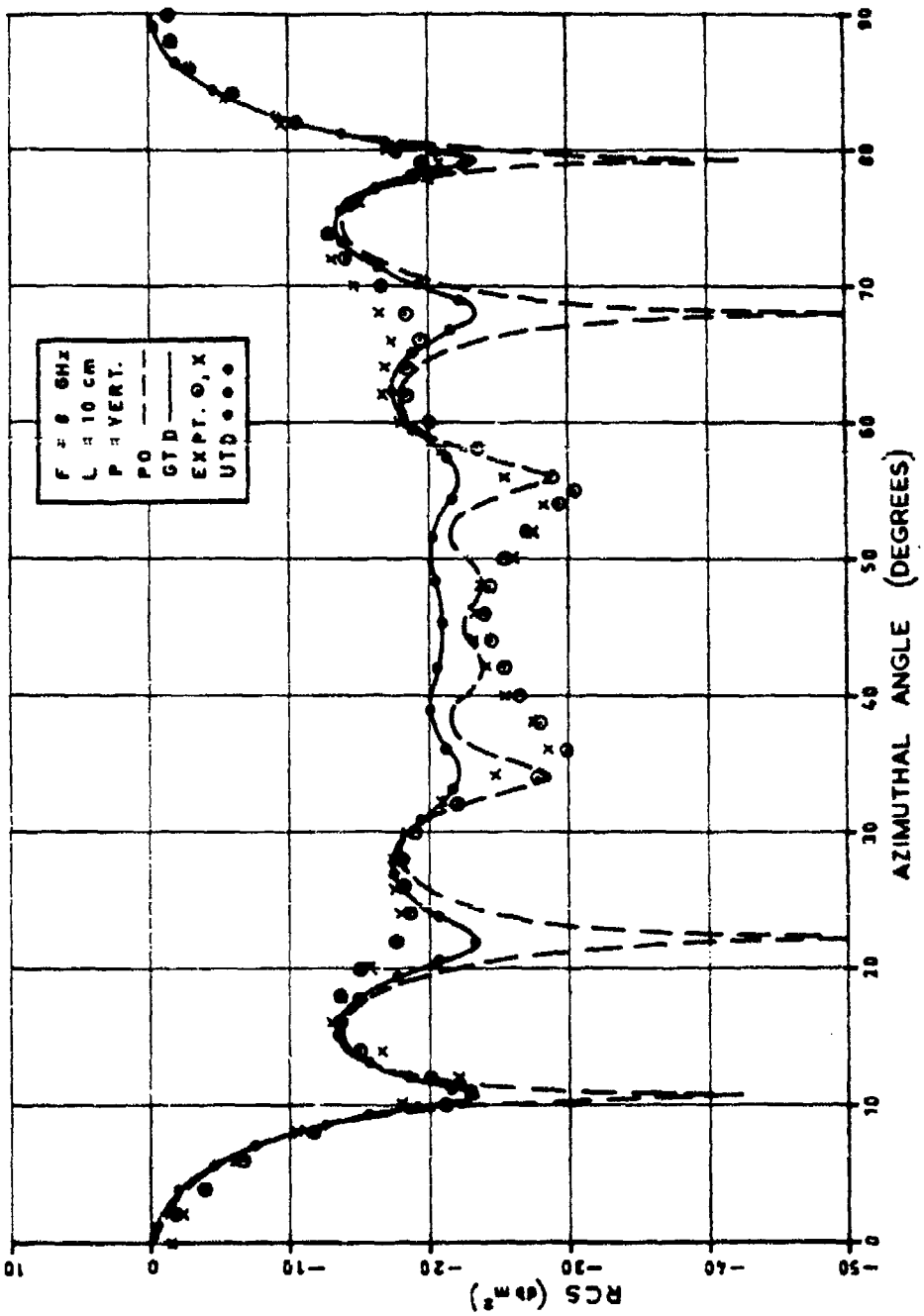

Figure 25. RCS for 10 cm cylinder at 8 GHz (vertical polarisation)

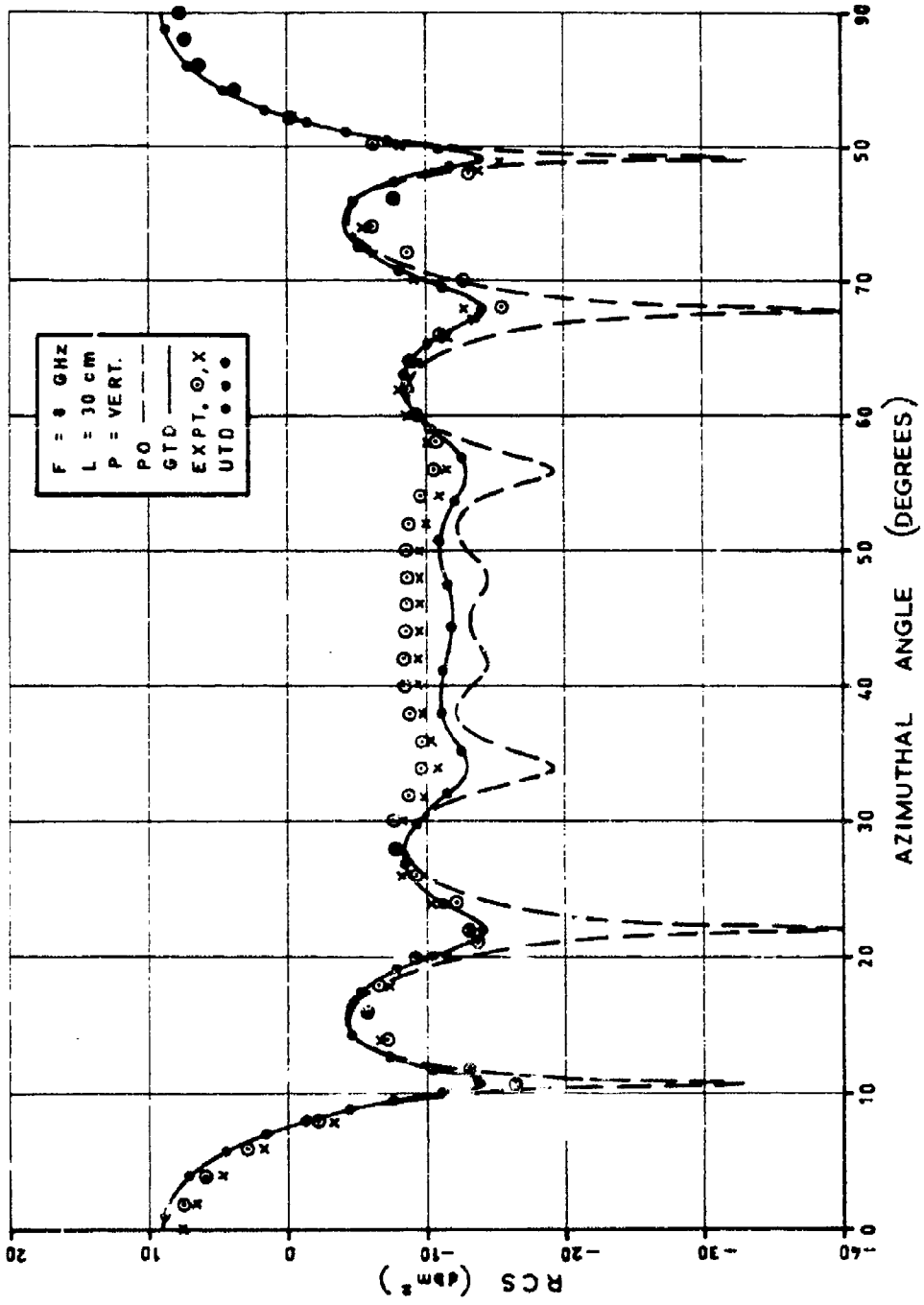

Figure 26. RCS for 30 cm cylinder at 8 GHz (vertical polarisation)

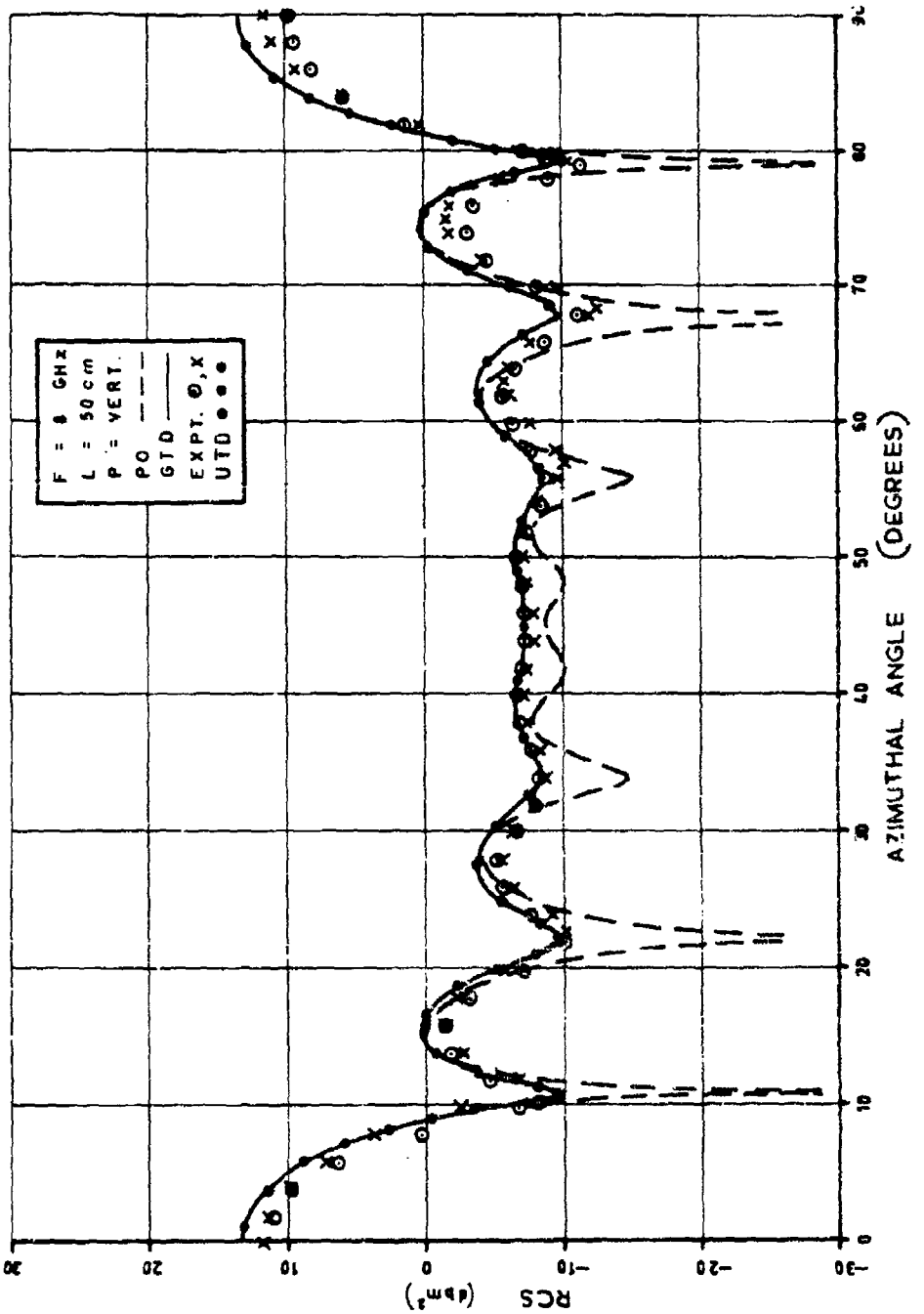

Figure 27. RCS for 50 cm cylinder at 8 GHz (vertical polarisation)

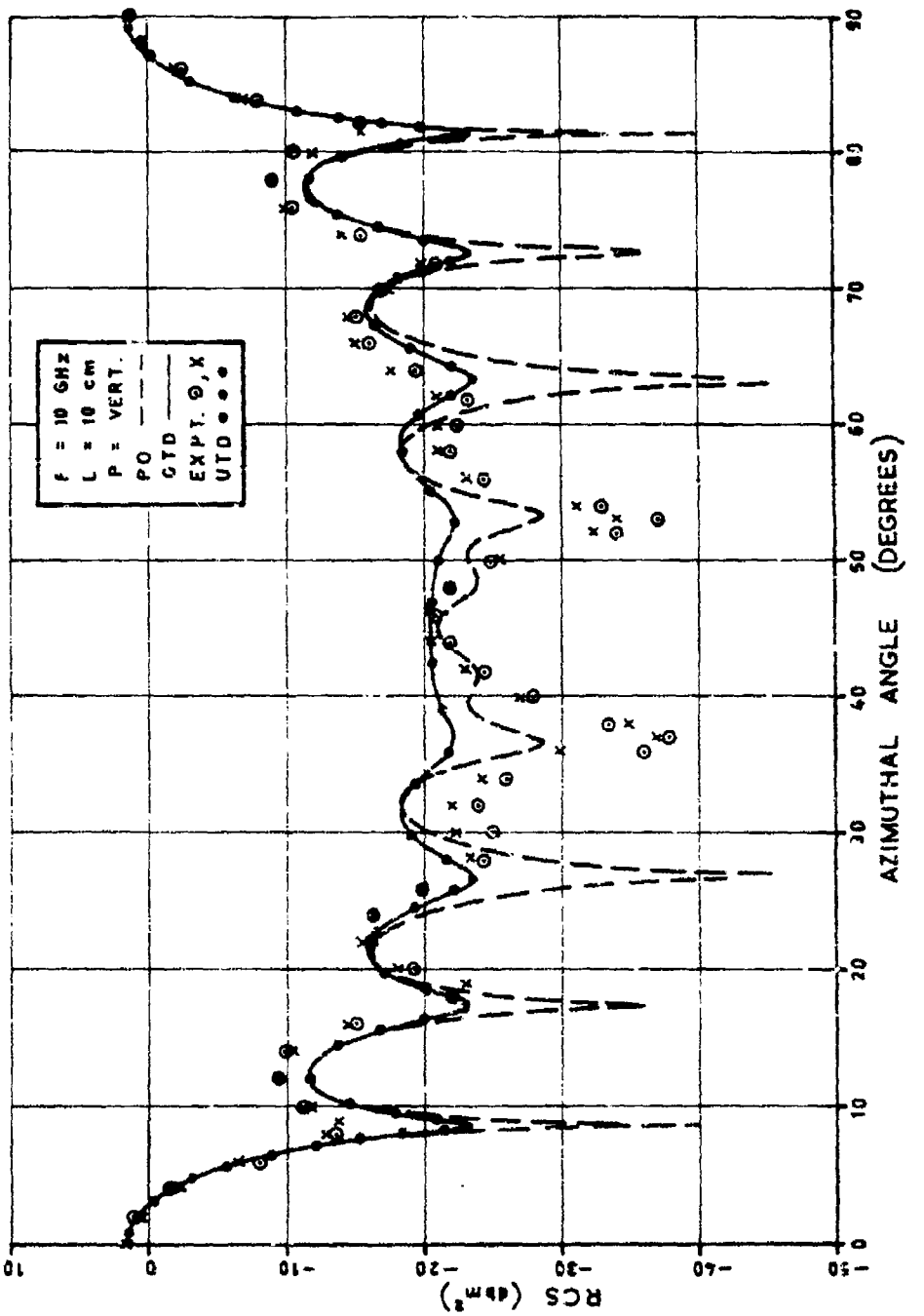

Figure 28. RCS for 10 cm cylinder at 10 GHz (vertical polarisation)

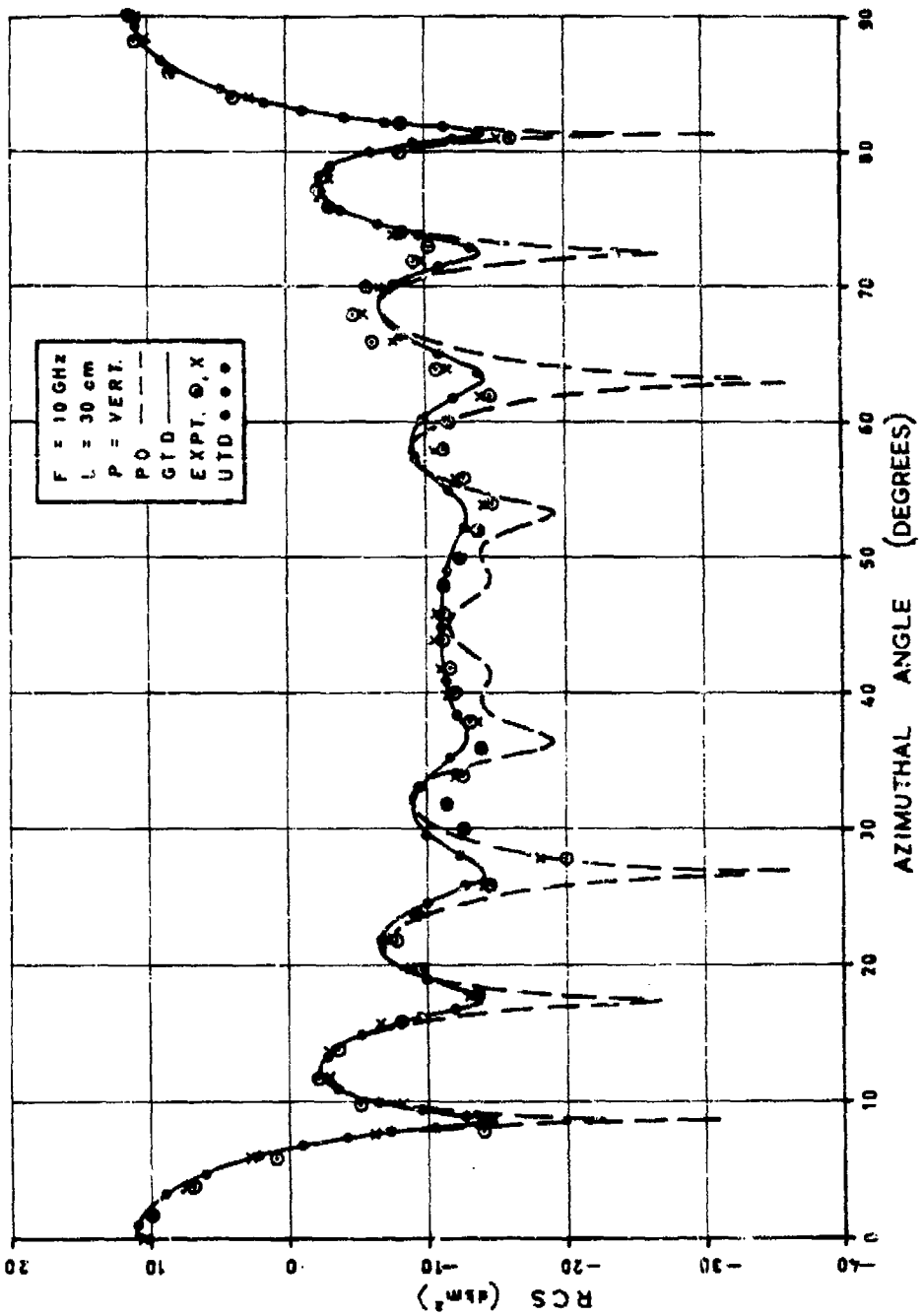

Figure 29. RCS for 30 cm cylinder at 10 GHz (vertical polarisation)

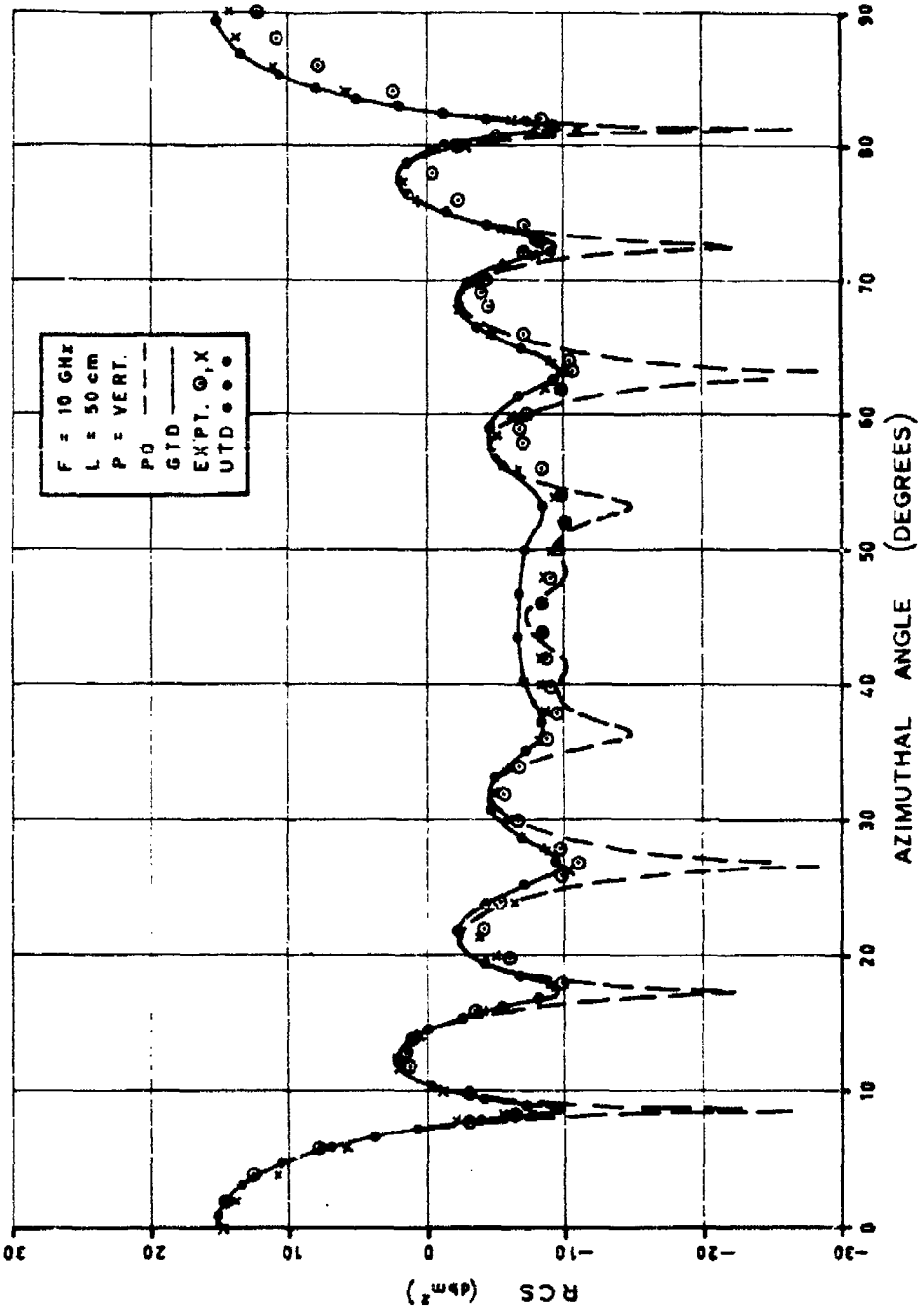

Figure 30. RCS for 50 cm cylinder at 10 GHz (vertical polarisation)

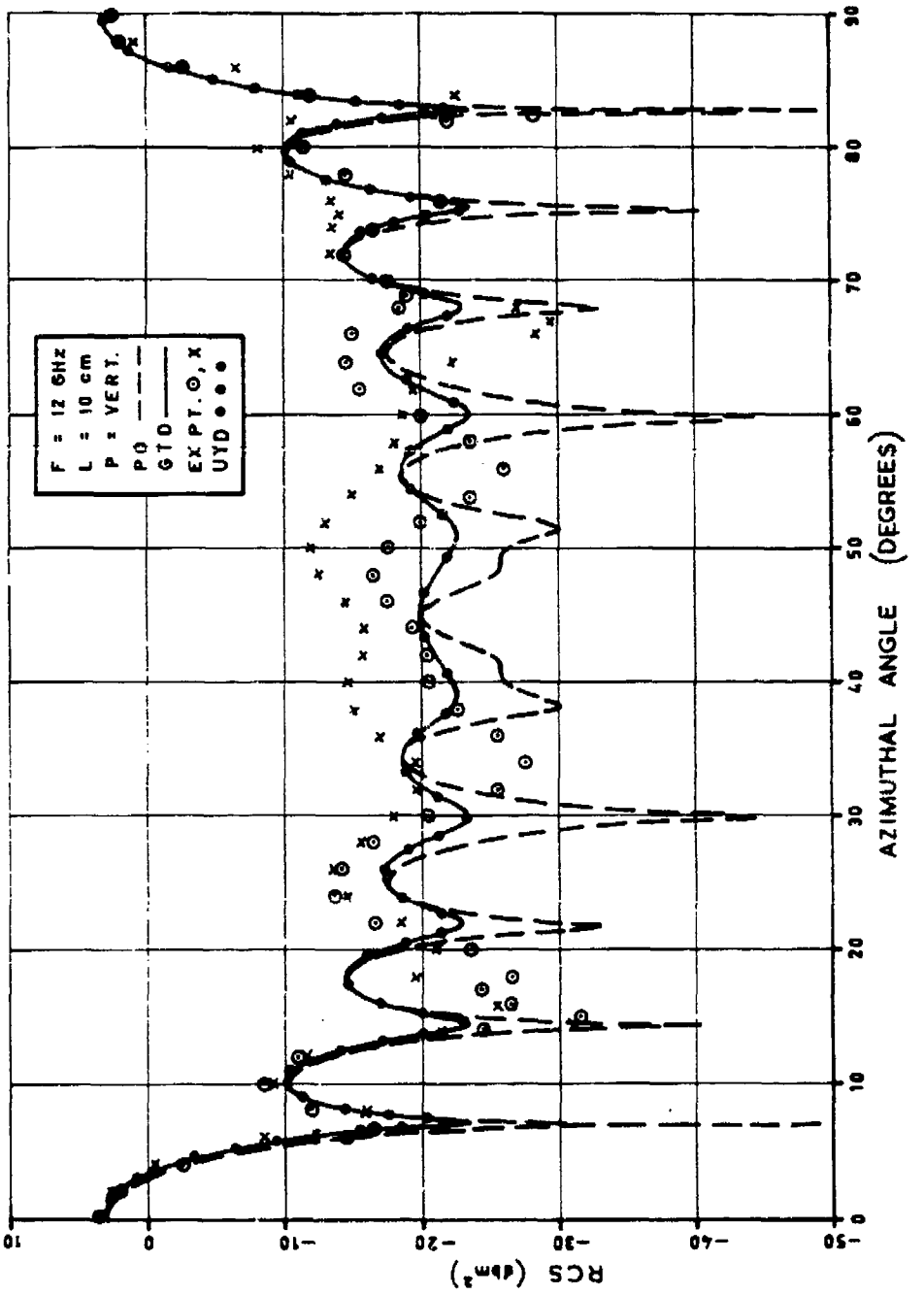

Figure 31. RCS for 10 cm cylinder at 12 GHz (vertical polarisation)

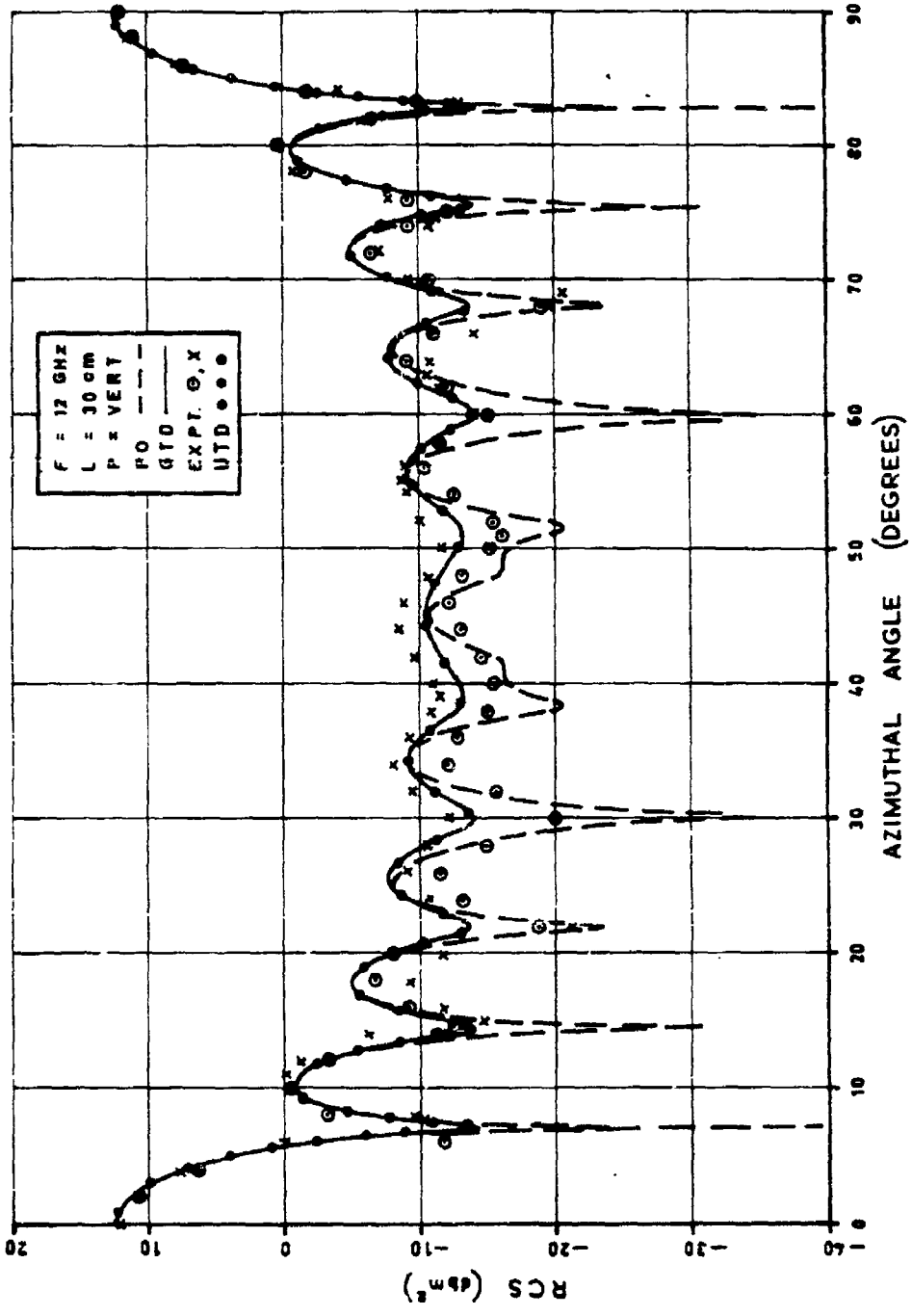

Figure 32. RCS for 30 cm cylinder at 12 GHz (vertical polarisation)

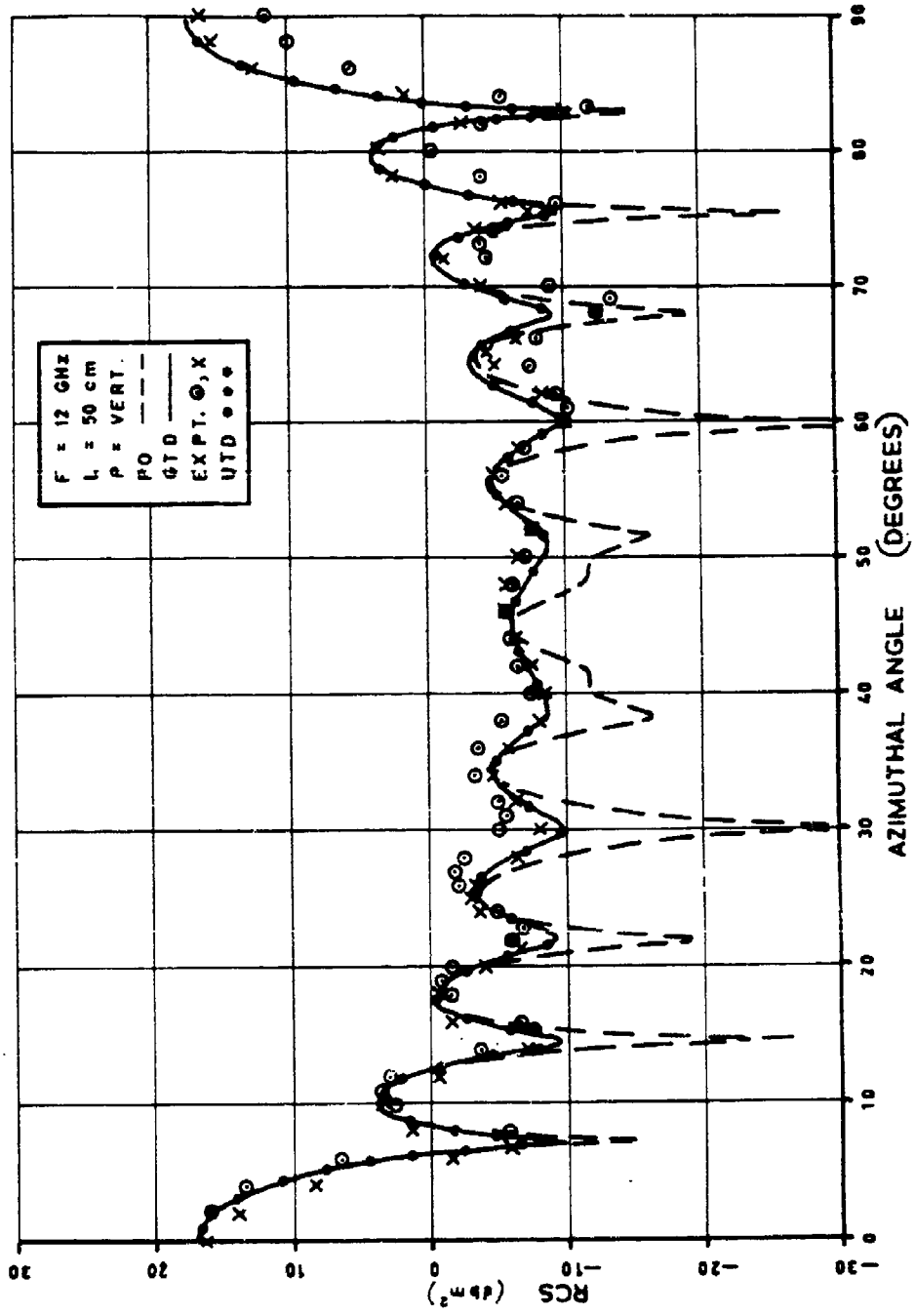

Figure 33. RCS for 50 cm cylinder at 12 GHz (vertical polarisation)

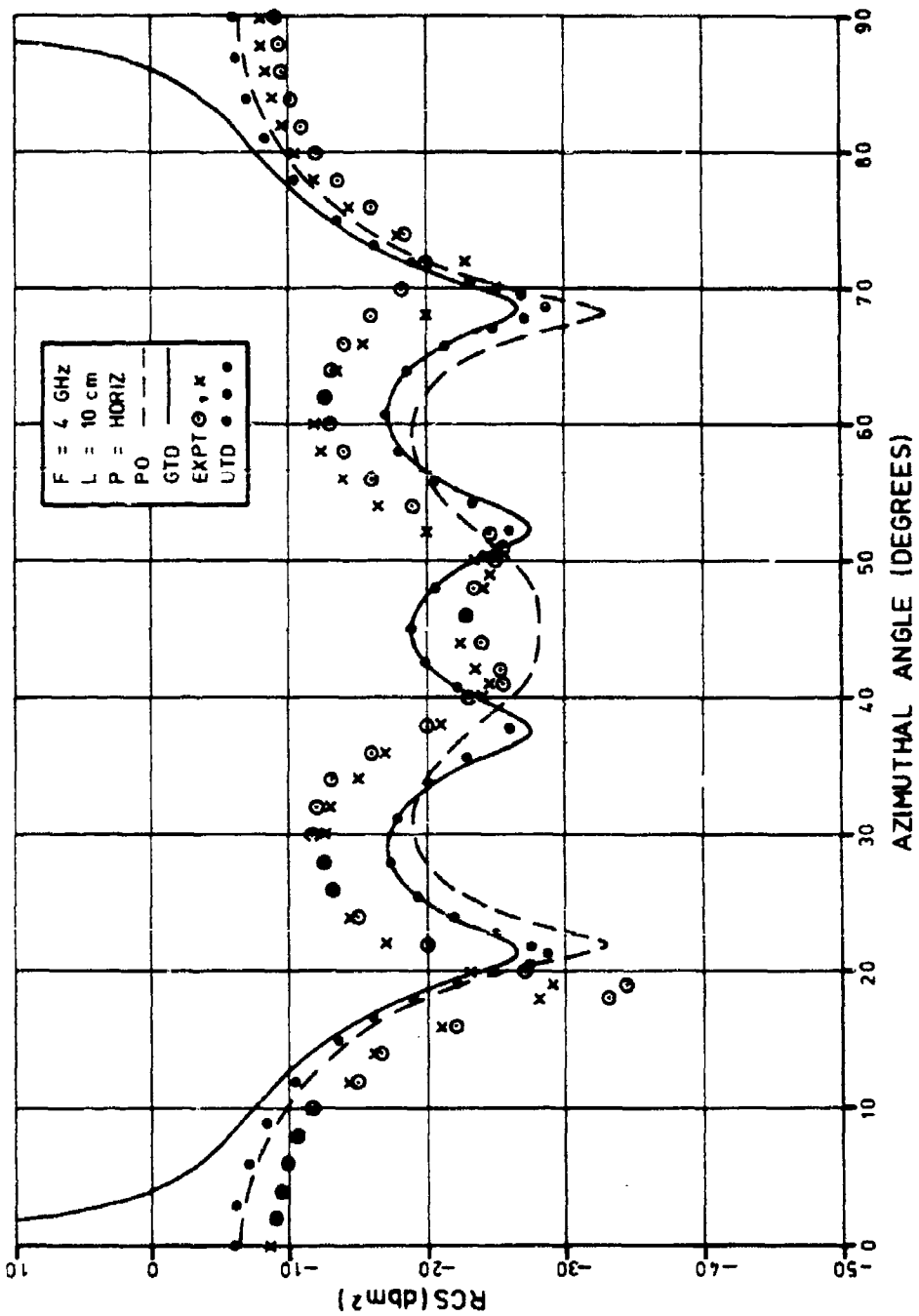

Figure 34. RCS for 10 cm cylinder at 4 GHz (horizontal polarisation)

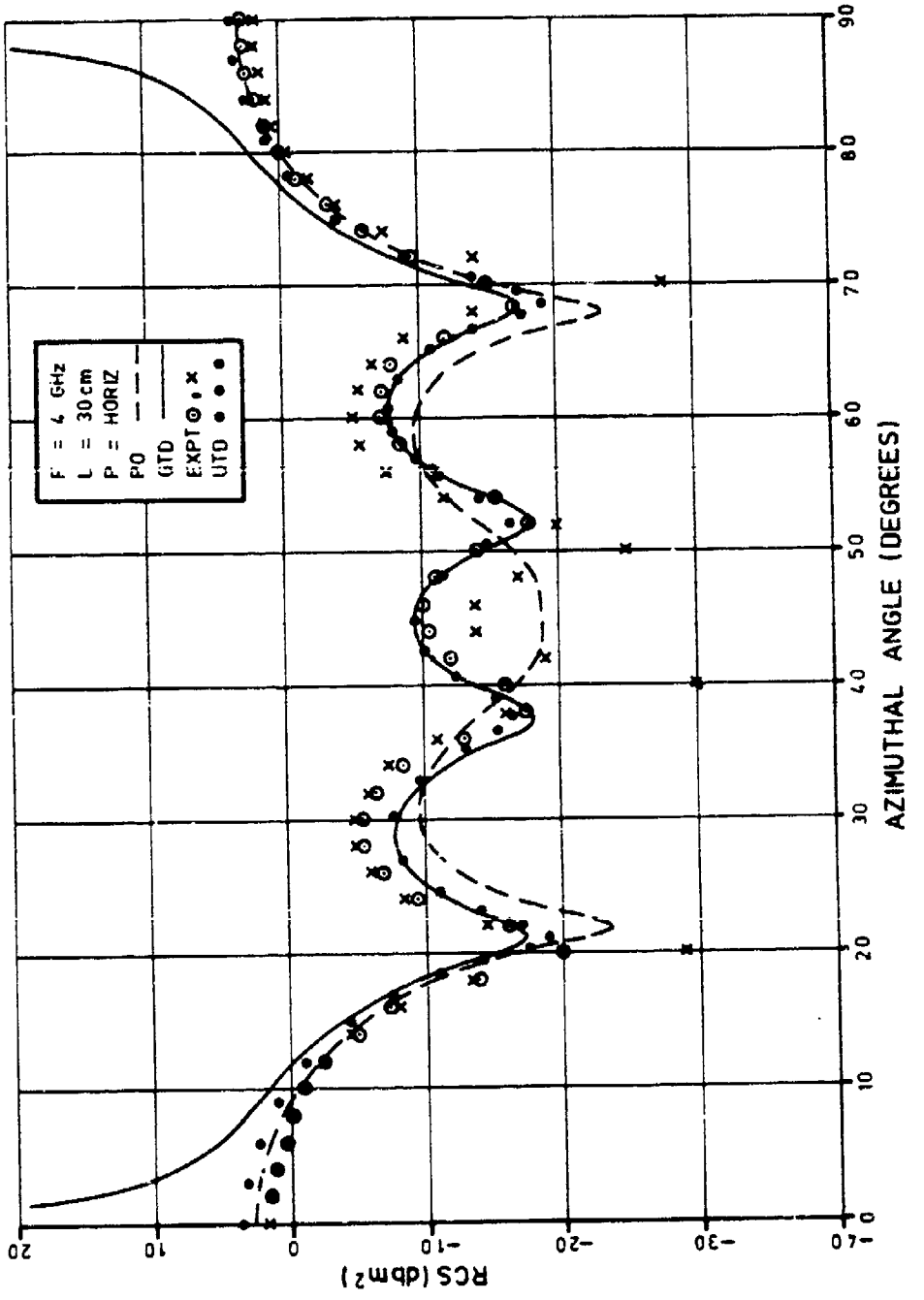

Figure 35. RCS for 30 cm cylinder at 4 GHz (horizontal polarisation)

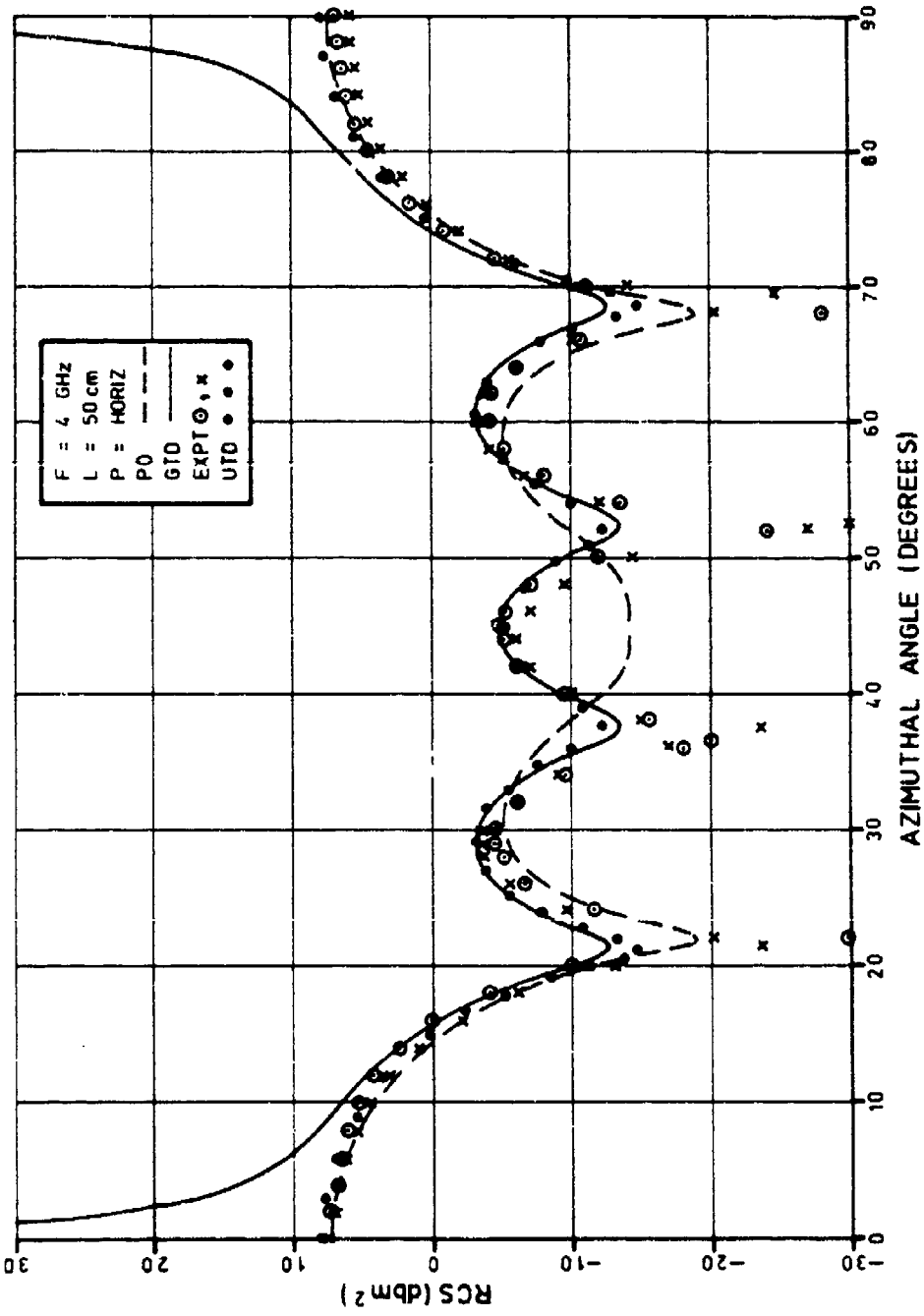

Figure 36. RCS for 50 cm cylinder at 4 GHz (horizontal polarisation)

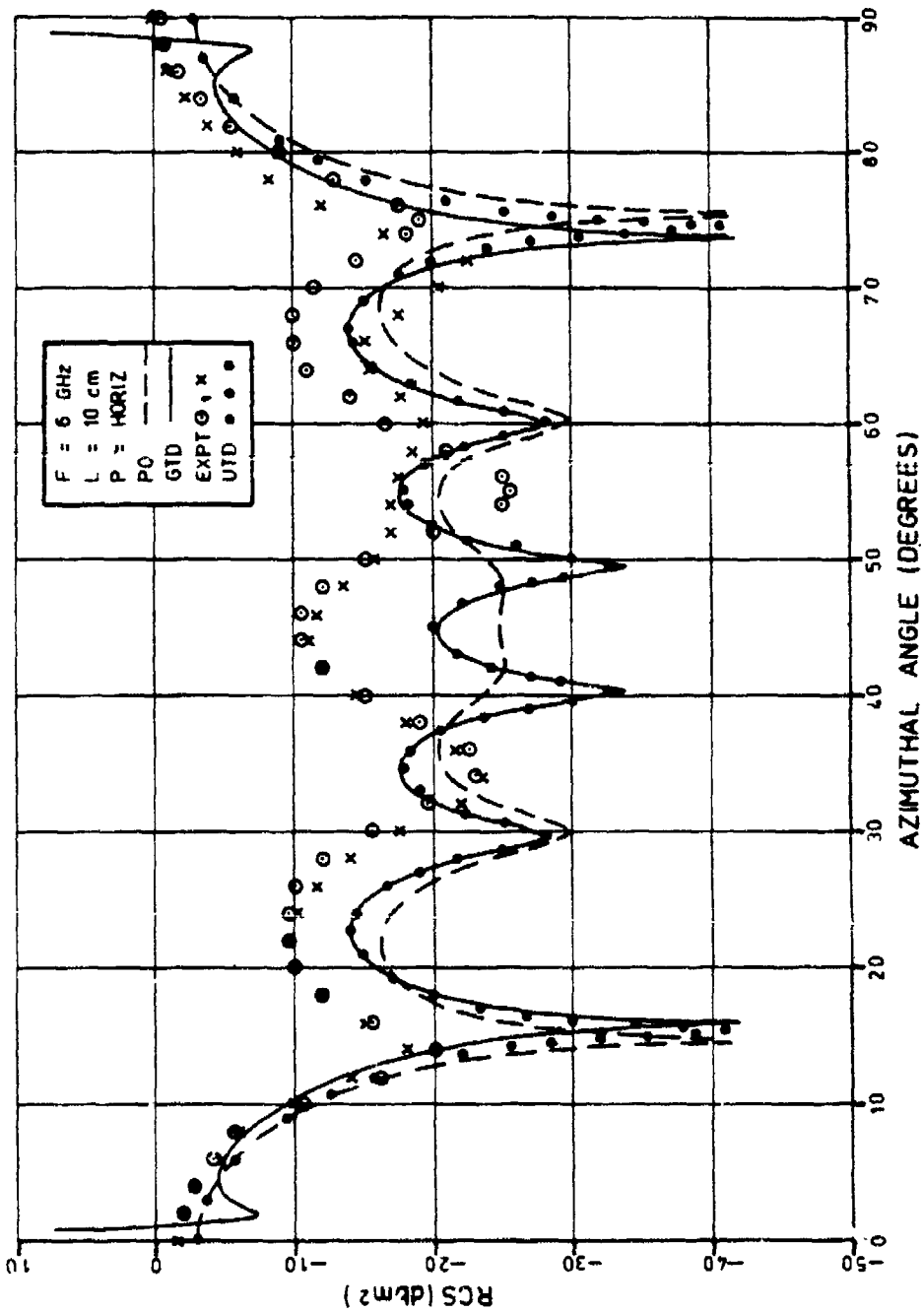

Figure 37. RCS for 10 cm cylinder at 6 GHz (horizontal polarisation)

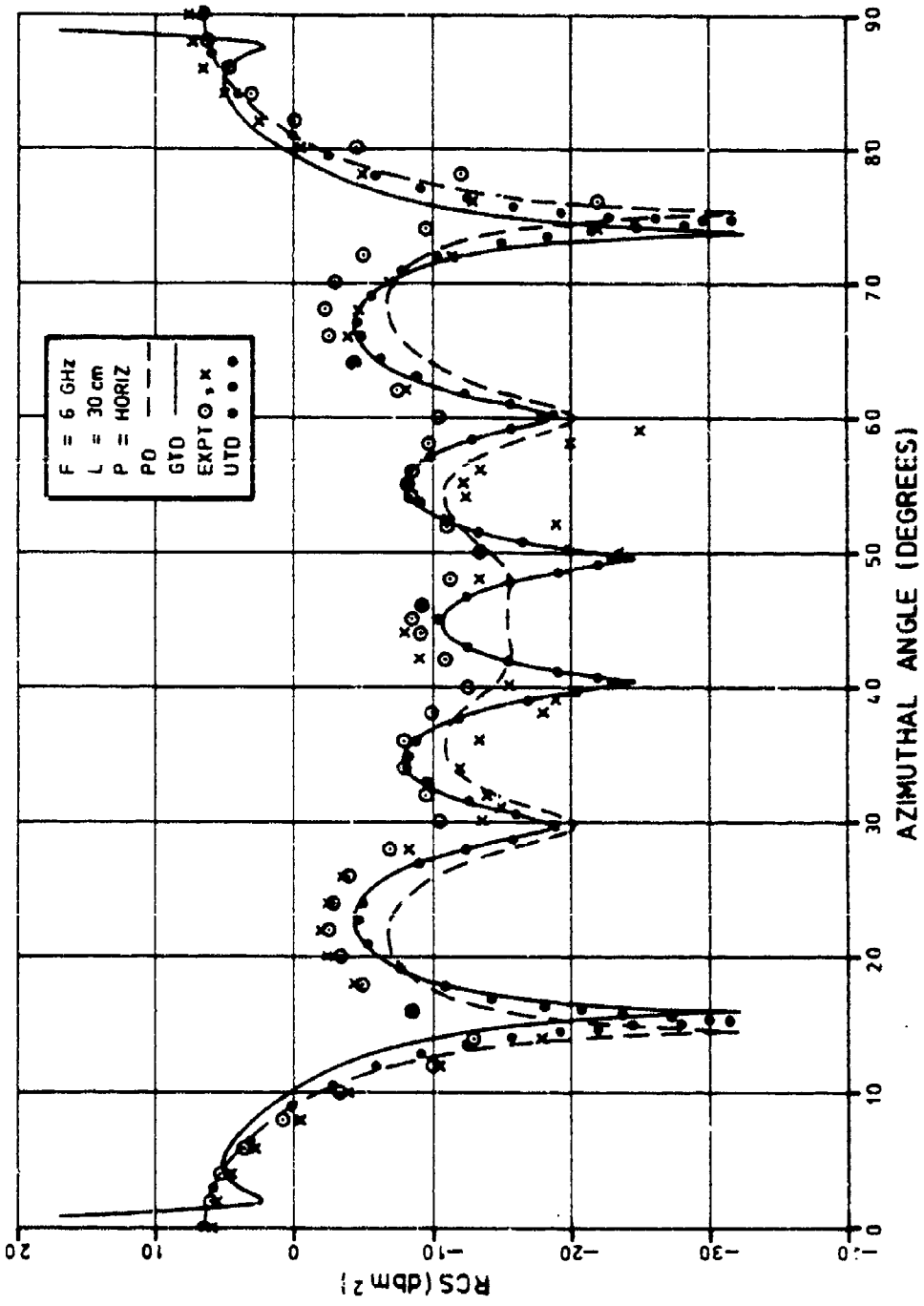

Figure 38. RCS for 30 cm cylinder at 6 GHz (horizontal polarisation)

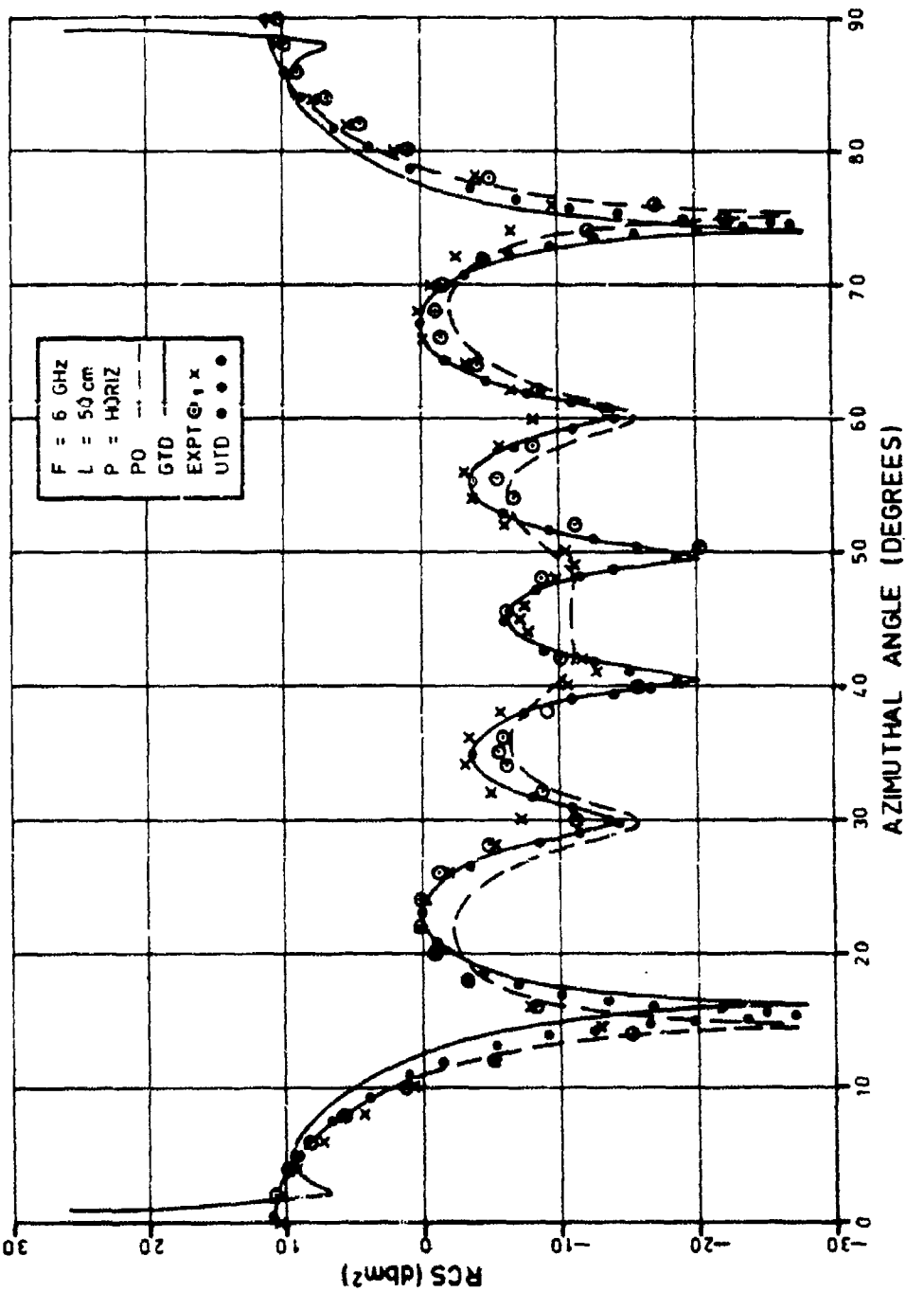

Figure 39. RCS for 50 cm cylinder at 6 GHz (horizontal polarisation)

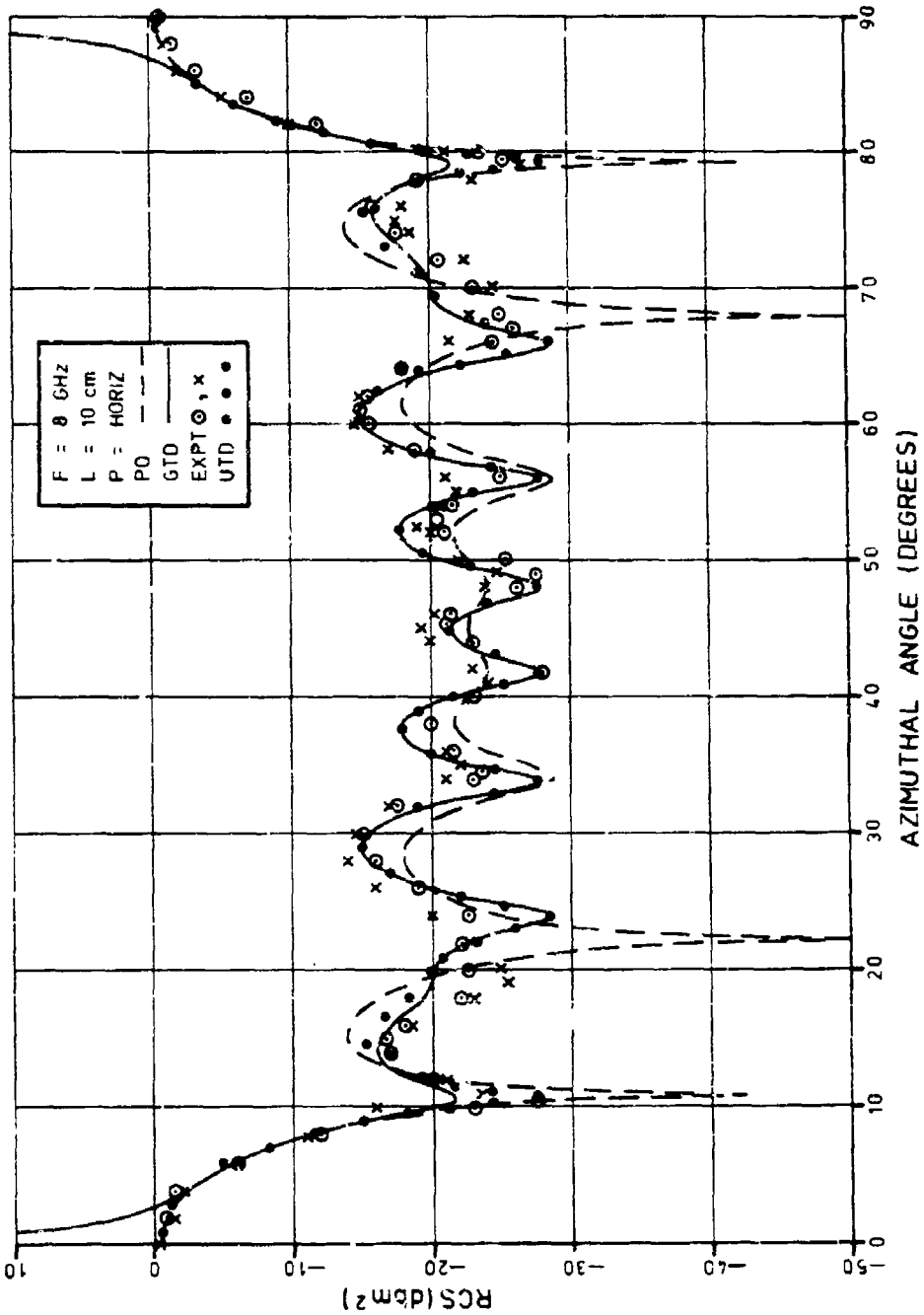

Figure 40. RCS for 10 cm cylinder at 8 GHz (horizontal polarisation)

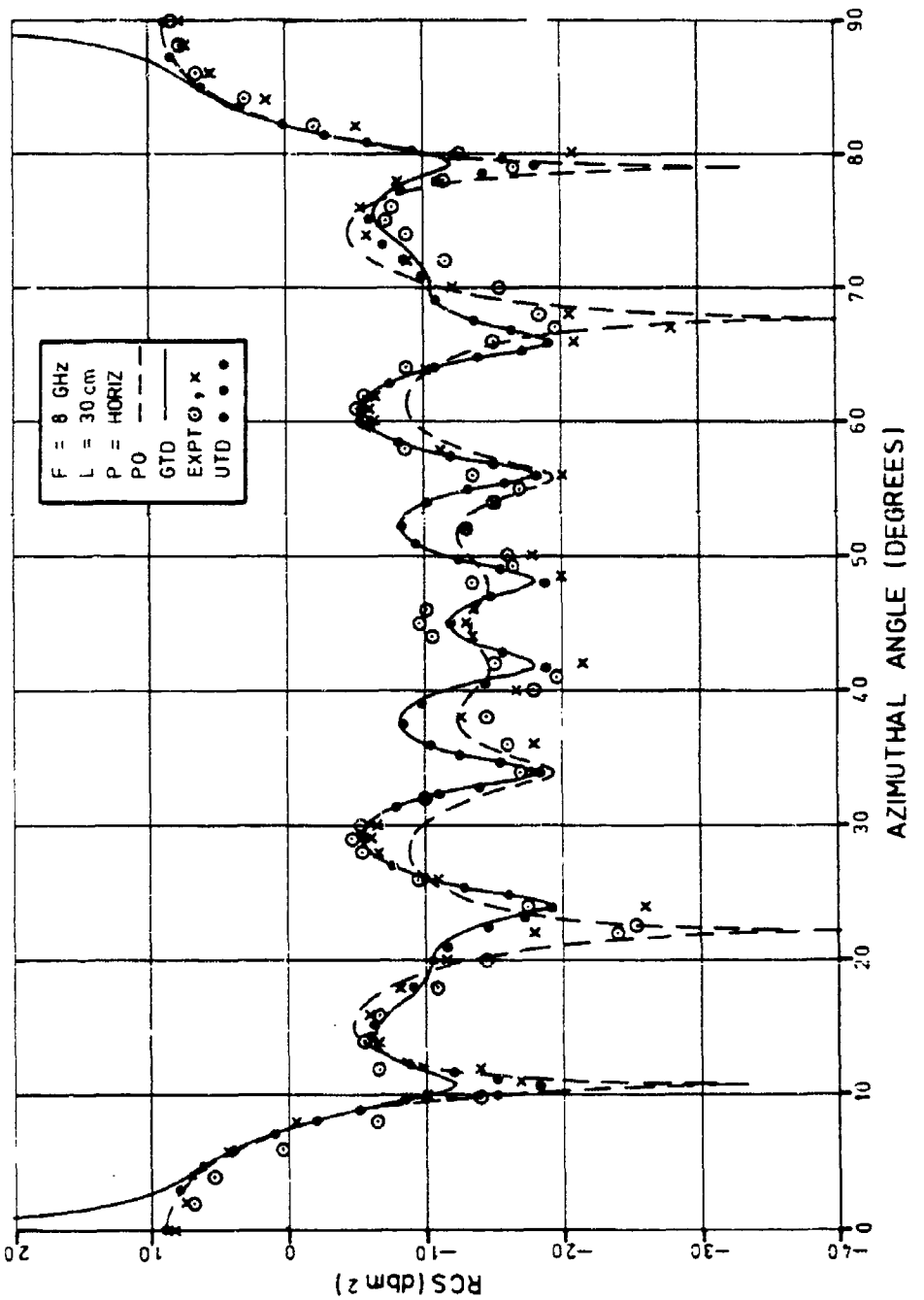

Figure 41. RCS for 30 cm cylinder at 8 GHz (horizontal polarisation)

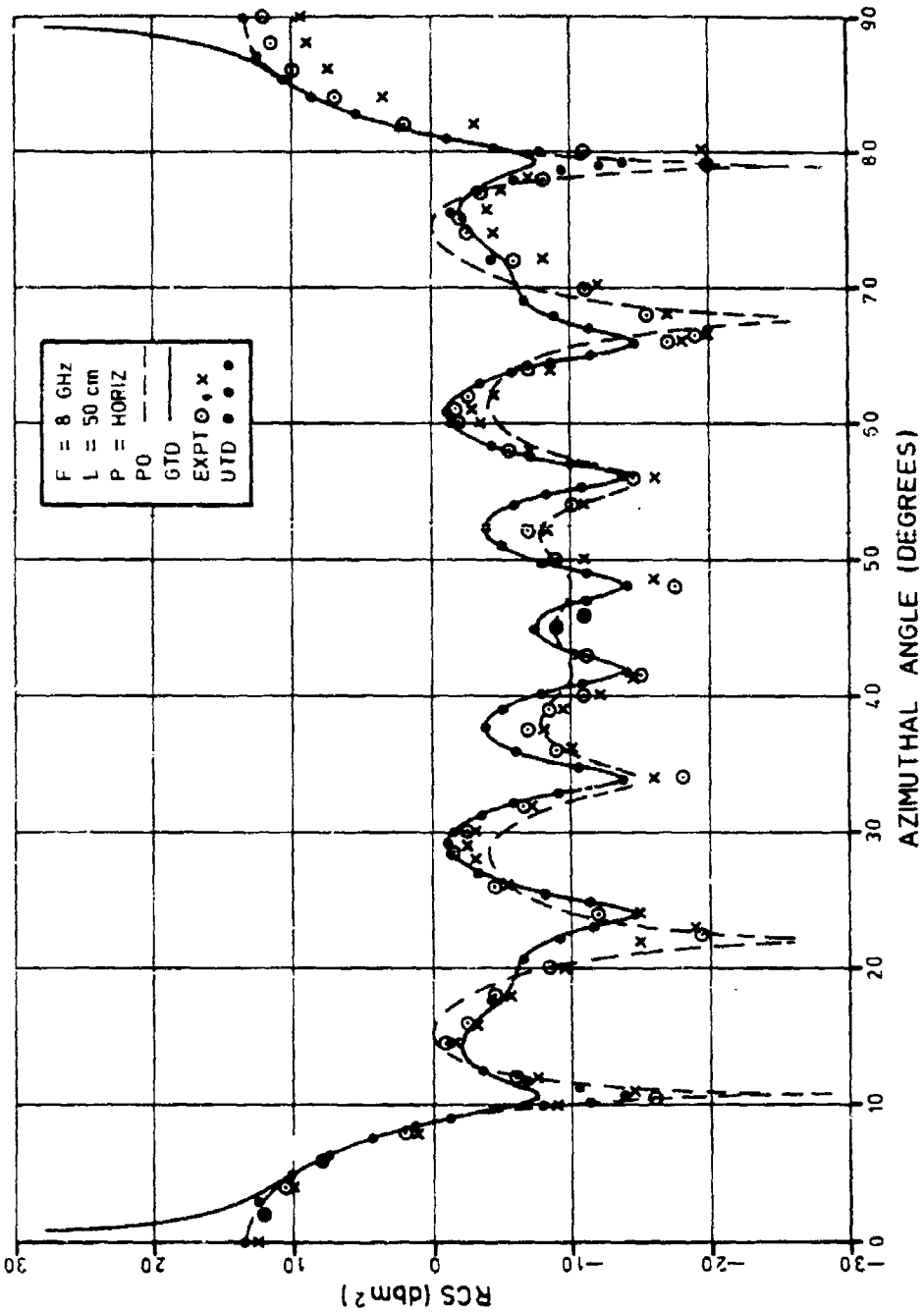

Figure 42. RCS for 50 cm cylinder at 8 GHz (horizontal polarisation)

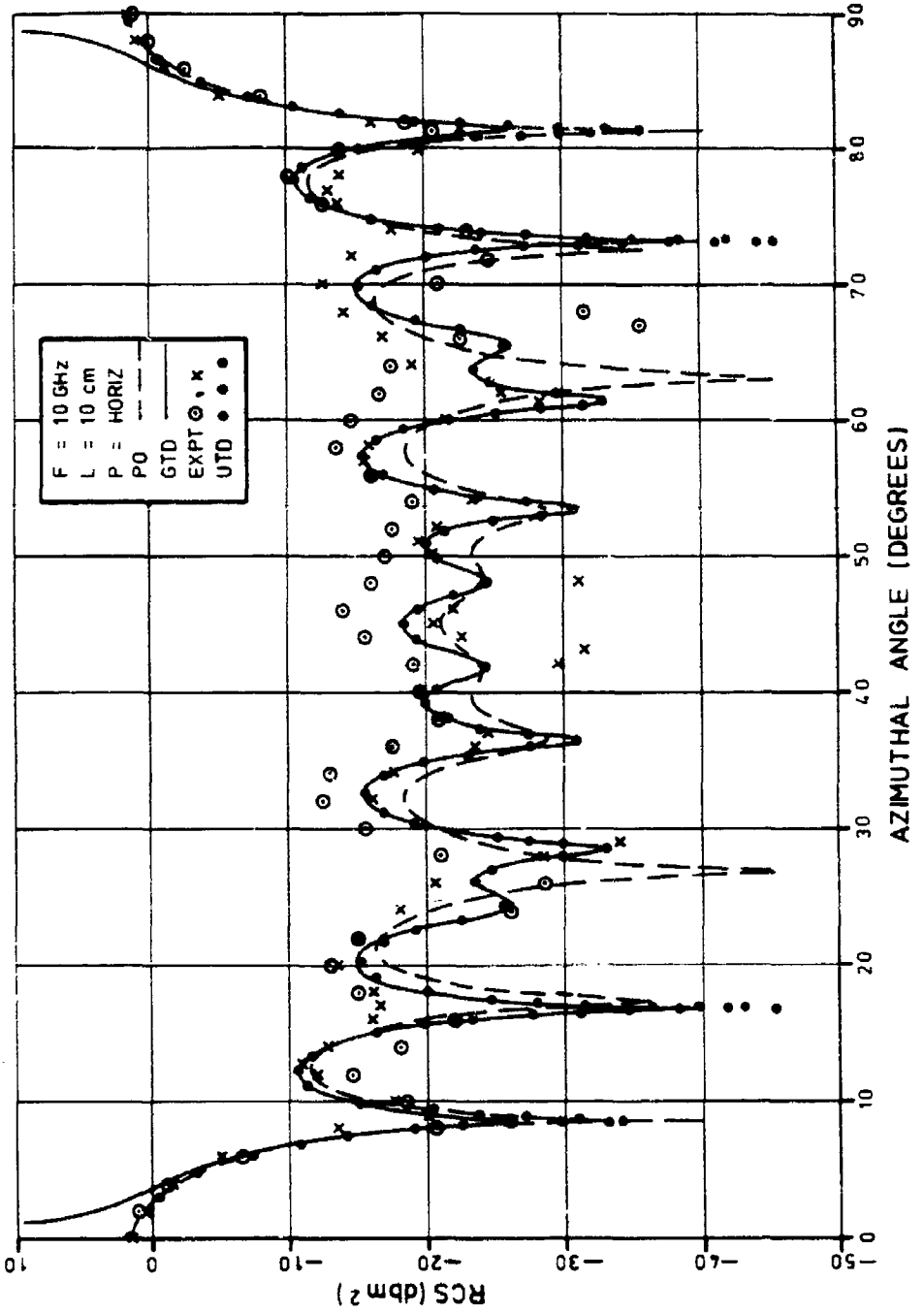

Figure 43. RCS for 10 cm cylinder at 10 GHz (horizontal polarisation)

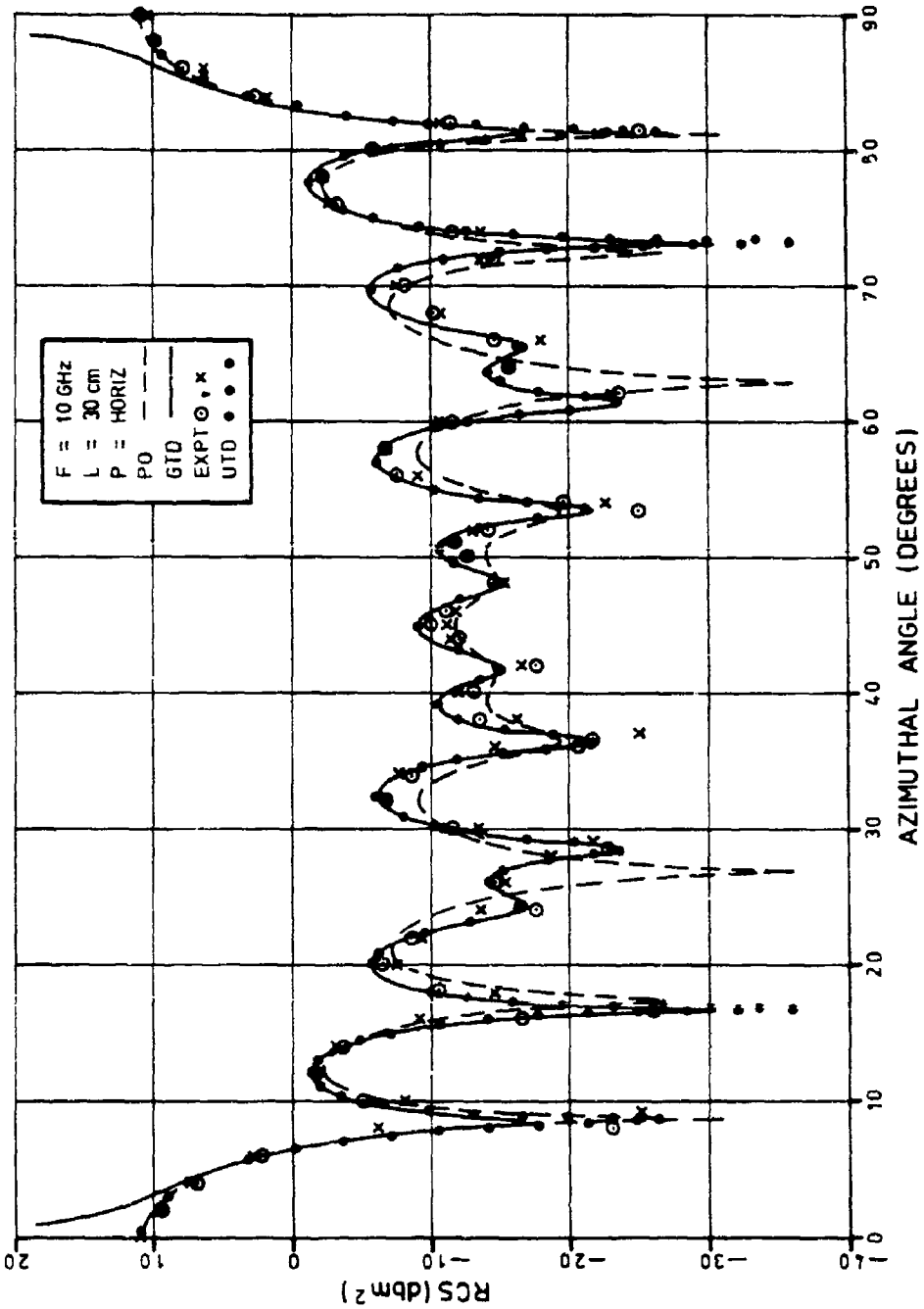

Figure 44. RCS for 30 cm cylinder at 10 GHz (horizontal polarisation)

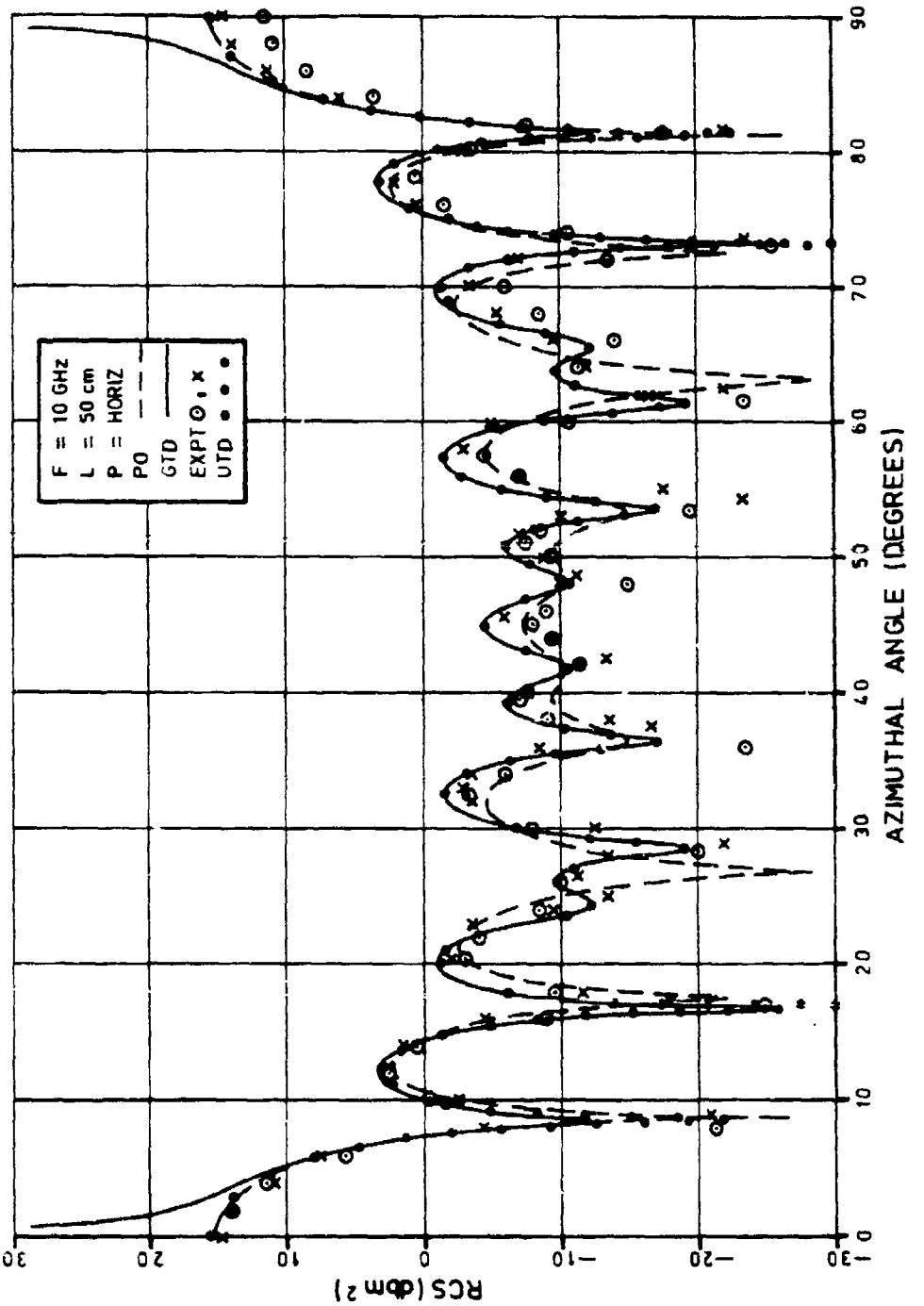

Figure 45. RCS for 50 cm cylinder at 10 GHz (horizontal polarisation)

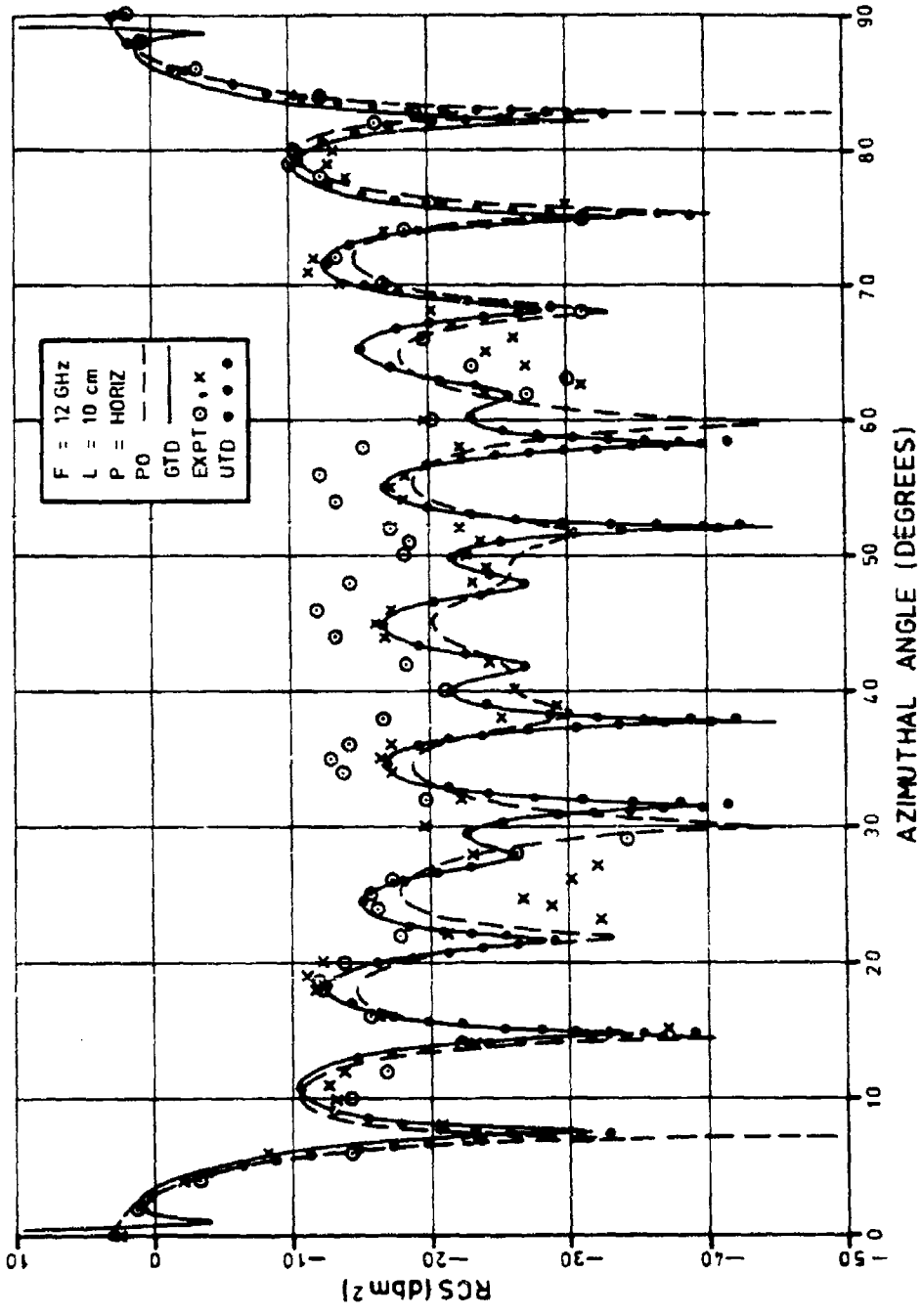

Figure 46. RCS for 10 cm cylinder at 12 GHz (horizontal polarisation)

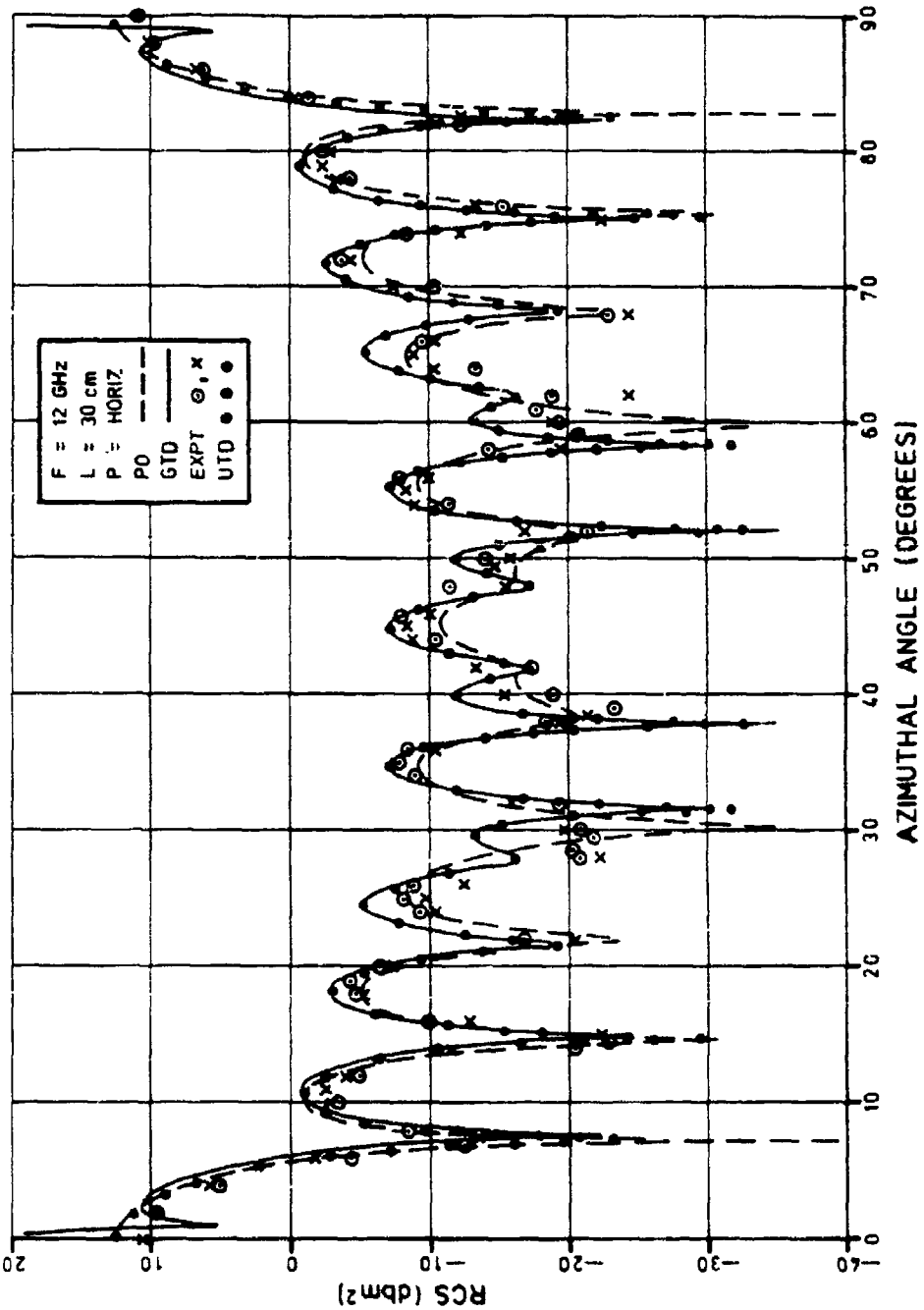

Figure 47. RCS for 30 cm cylinder at 12 GHz (horizontal polarisation)

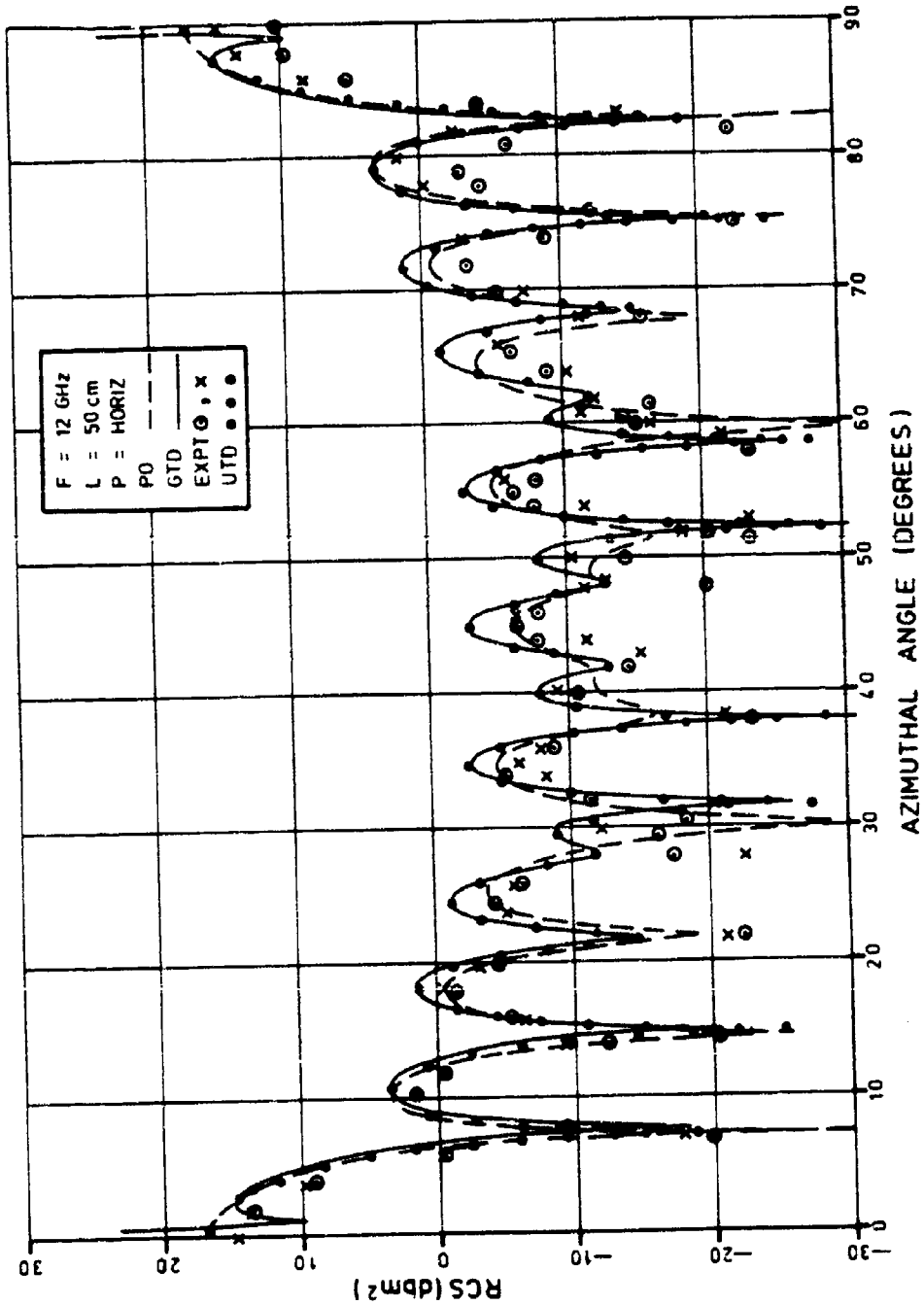

Figure 48. RCS for 50 cm cylinder at 12 GHz (horizontal polarisation)

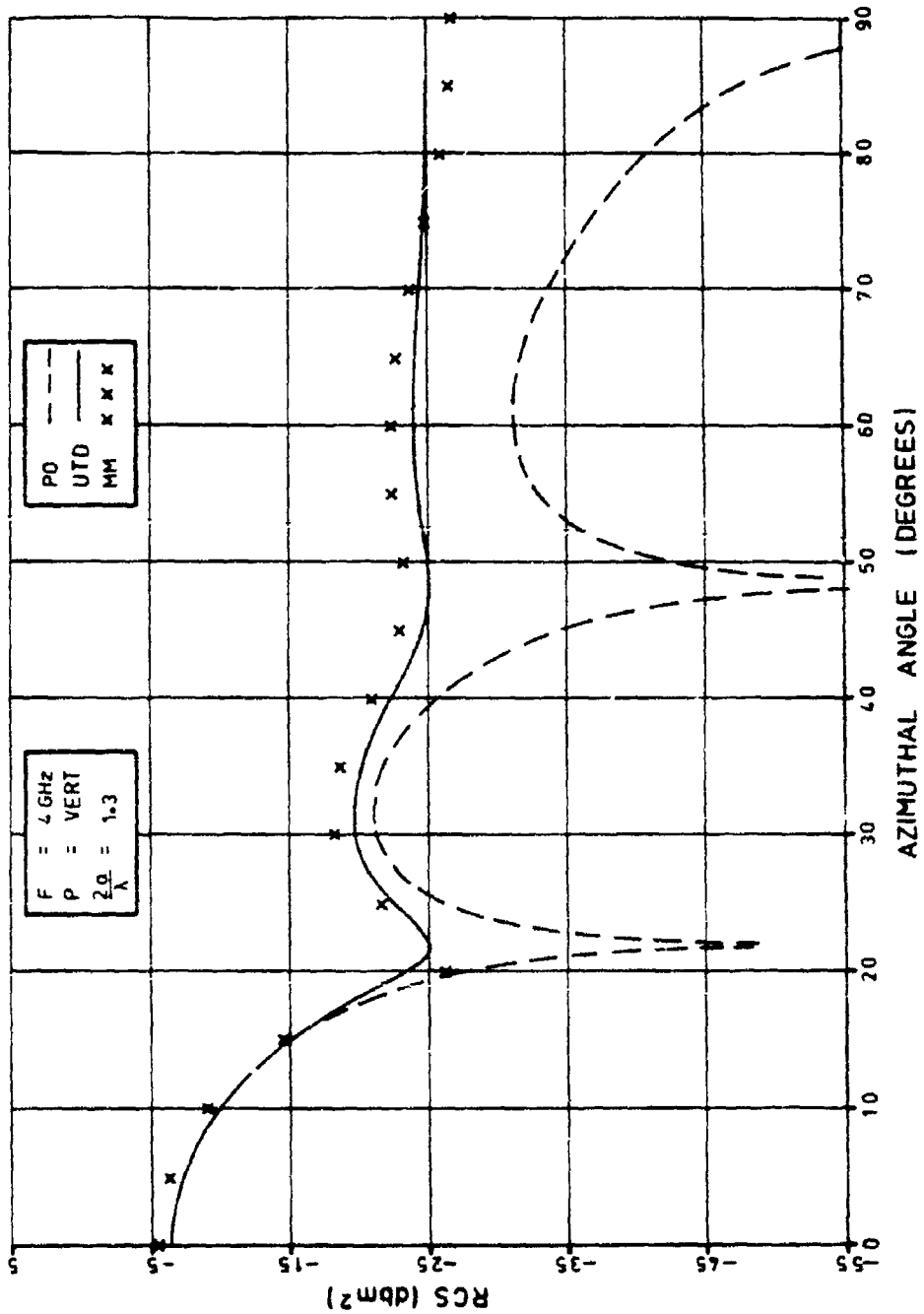

Figure 49. Comparison of UTD, PO and MM solutions for the flat plate at 4 GHz (vertical polarisation)

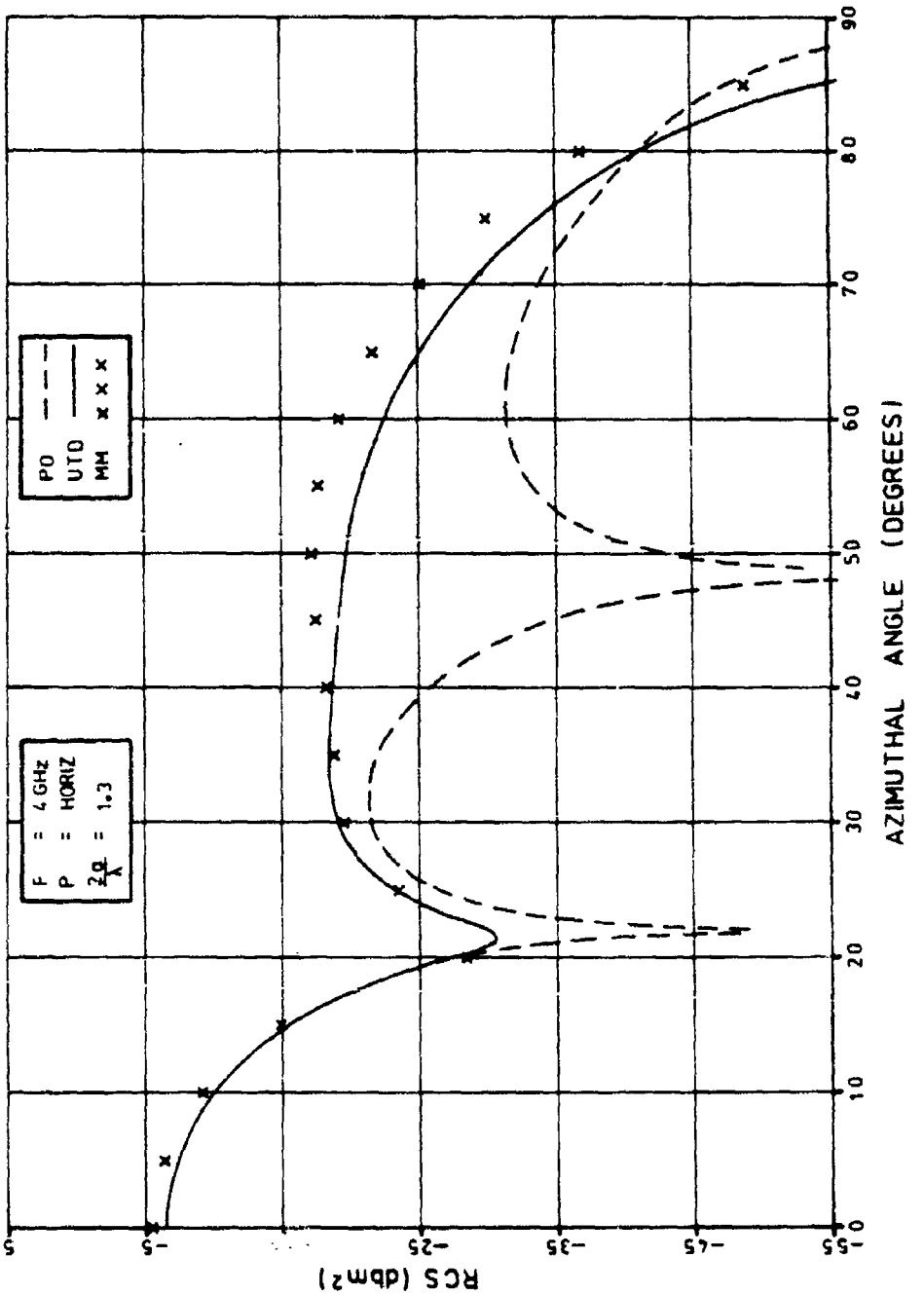

Figure 50. Comparison of UTD, PO and MM solutions for the flat plate at 4 GHz (horizontal polarisation)

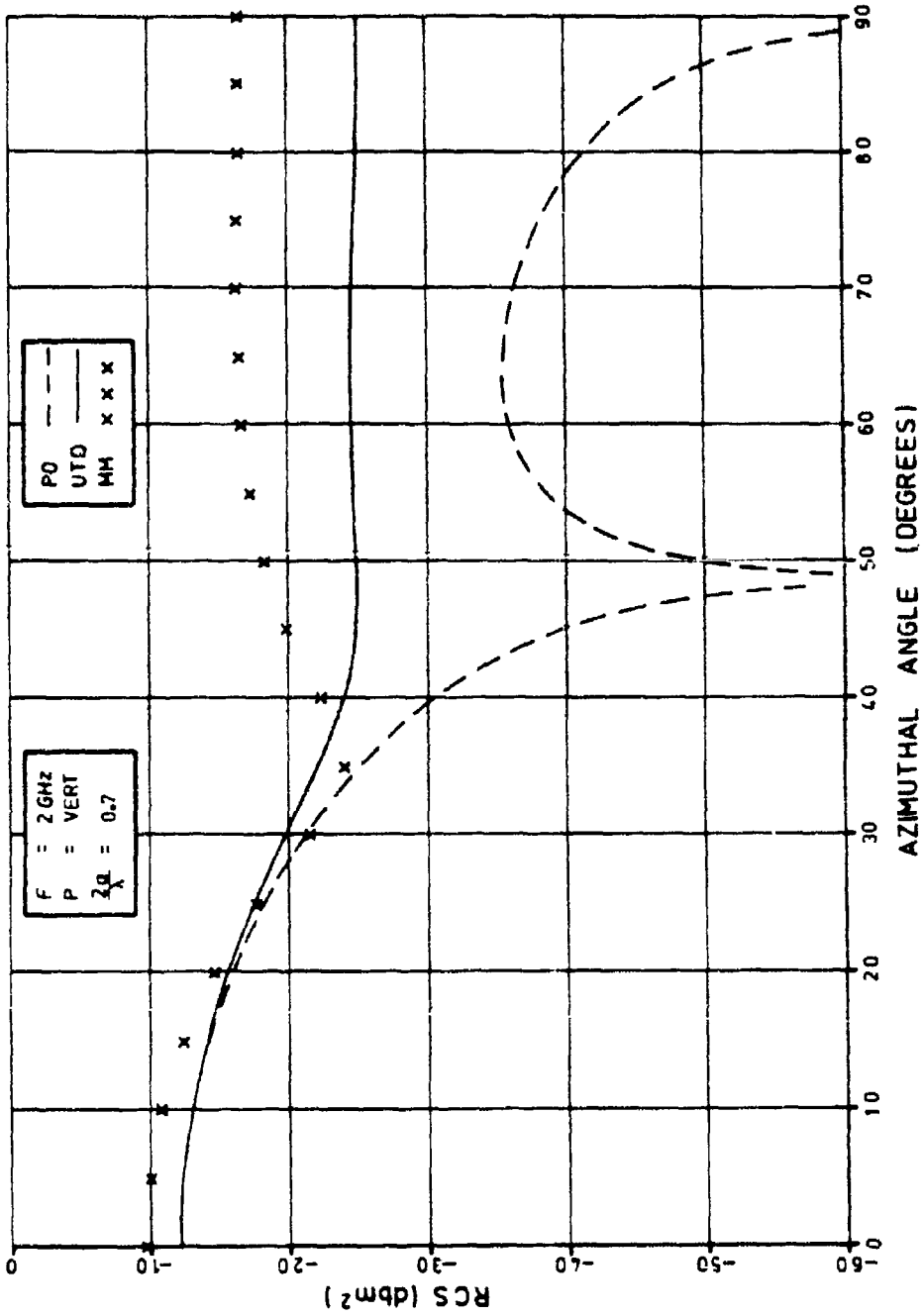

Figure 51. Comparison of UTD, PO and MM solutions for the flat plate at 2 GHz (vertical polarisation)

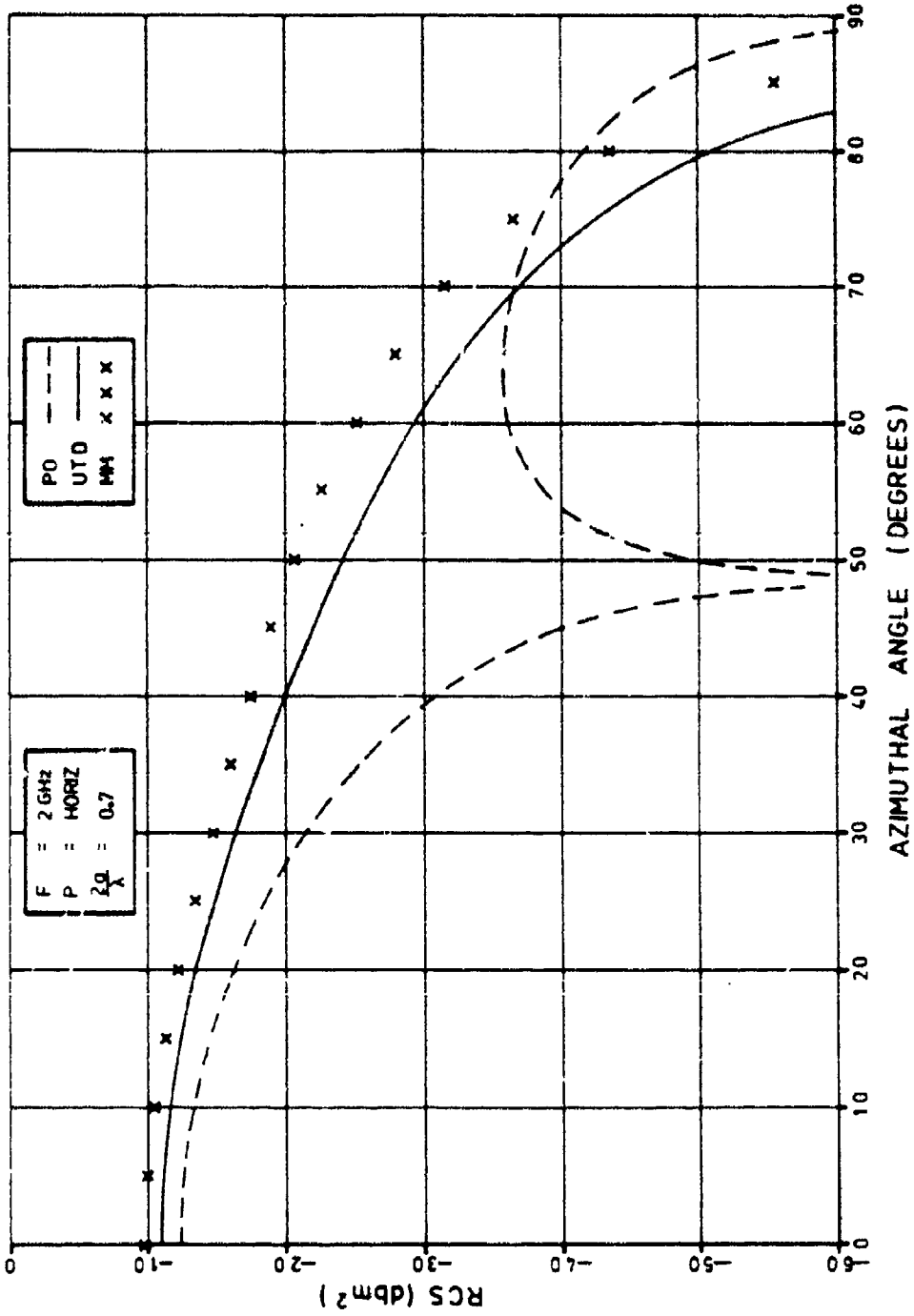

Figure 52. Comparison of UTD, PO and MM solutions for the flat plate at 2 GHz (horizontal polarisation)

DISTRIBUTION

	Copy No.
EXTERNAL	
In United Kingdom	
Defence Science Representative, London	Cnt Sht Only
Mr P. Varnish, Admiralty Research Establishment, Portsdown	1
British Library, Lending Division	2
Institution of Electrical Engineers	3
In United States of America	
Counsellor, Defence Science, Washington	Cnt Sht Only
Engineering Societies Library	4
In Australia	
Chief Defence Scientist	5
Deputy Chief Defence Scientist	
Controller, External Relations, Projects and Analytical Studies	
Superintendent, Science Programs and Administration	
Director, Joint Intelligence Organisation (DSTI)	6
Document Exchange Centre Defence Information Services Branch for:	
Microfilming	7
United Kingdom, Defence Research Information Centre (DRIC)	8 - 9
United States, Defense Technical Information Center (DTIC)	10 - 21
Canada, Director, Scientific Information Services	22
New Zealand, Ministry of Defence	23
National Library of Australia	24
Director General, Army Development (NSO), Russell Offices for ABCA Standardisation Officers	
UK ABCA representative, Canberra	25
US ABCA representative, Canberra	26
Canada ABCA representative, Canberra	27
NZ ABCA representative, Canberra	28

Librarian, Technical Reports Centre, Defence Library, Campbell Park	29
Library, H Block, Victoria Barracks, Melbourne	30
WITHIN DRCS	
Director, Electronics Research Laboratory	31
Superintendent, Radar Division	32
Senior Principal Research Scientist, Radar	33
Principal Officer, Microwave Radar Group	34
Principal Officer, Radio Group	35
Principal Officer, Jindalee Development Group	36
Principal Officer, Jindalee Project Group	37
Dr G.R. Haack, Radio Group	38
Mr A.T. Tickner, Radio Group	39
Dr J.L. Whitrow, Microwave Radar Group	40
Dr W.C. Anderson, Radio Group	41
Dr S.J. Anderson, Jindalee Development Group	42
DRCS Library	43
Spares	44 - 50

DOCUMENT CONTROL DATA SHEET

Security classification of this page: UNCLASSIFIED

1 DOCUMENT NUMBERS		2 SECURITY CLASSIFICATION	
AR Number:	AR-004-260	a. Complete Document:	Unclassified
Series Number:	ERL-0344-TR	b. Title in Isolation:	Unclassified
Other Numbers:		c. Summary in Isolation:	Unclassified

3 TITLE

THE RADAR CROSS SECTION OF PERFECTLY-CONDUCTING RECTANGULAR FLAT PLATES AND RECTANGULAR CYLINDERS - A COMPARISON OF PHYSICAL OPTICS, GTD AND UTD SOLUTIONS

4 PERSONAL AUTHOR(S):

W.C. Anderson

5 DOCUMENT DATE:

August 1985

6 6.1 TOTAL NUMBER OF PAGES 89

6.2 NUMBER OF REFERENCES: 17

7 7.1 CORPORATE AUTHOR(S):

Electronics Research Laboratory

7.2 DOCUMENT SERIES AND NUMBER

Electronics Research Laboratory 0344-TR

8 REFERENCE NUMBERS

a. Task: DST 92/001

b. Sponsoring Agency:

9 COST CODE:

644665

10 IMPRINT (Publishing organisation)

Defence Research Centre Salisbury

11 COMPUTER PROGRAM(S) (Title(s) and language(s))

12 RELEASE LIMITATIONS (of the document):

Approved for Public Release

Security classification of this page: UNCLASSIFIED

Security classification of this page: UNCLASSIFIED

13 **ANNOUNCEMENT LIMITATIONS** (of the information on these pages):

No limitation

14 **DESCRIPTORS:**

a. EJC Thesaurus Terms

Optics
Diffraction
Electromagnetic scattering
Backscattering

(AUSTRALIA)

b. Non-Thesaurus Terms

15 **COSATI CODES:**

20060

16 **SUMMARY OR ABSTRACT:**
(if this is security classified, the announcement of this report will be similarly classified)

The method of Physical Optics, the Geometrical Theory of Diffraction and the Uniform Geometrical Theory of Diffraction are applied here to electromagnetic scattering from flat plates and rectangular cylinders. The results are compared with experimental measurements to establish the domains of validity of the theoretical techniques.

requires include!

Security classification of this page: UNCLASSIFIED